

# Validacija sprege gibanja krutog tijela i računalne dinamike fluida u frekvencijskoj domeni

---

**Volarić, Filip**

**Master's thesis / Diplomski rad**

**2017**

*Degree Grantor / Ustanova koja je dodijelila akademski / stručni stupanj:* **University of Zagreb, Faculty of Mechanical Engineering and Naval Architecture / Sveučilište u Zagrebu, Fakultet strojarstva i brodogradnje**

*Permanent link / Trajna poveznica:* <https://urn.nsk.hr/urn:nbn:hr:235:234447>

*Rights / Prava:* [In copyright](#)/[Zaštićeno autorskim pravom.](#)

*Download date / Datum preuzimanja:* **2024-11-29**

*Repository / Repozitorij:*

[Repository of Faculty of Mechanical Engineering and Naval Architecture University of Zagreb](#)



UNIVERSITY OF ZAGREB  
Faculty of Mechanical Engineering and Naval Architecture

# **MASTER'S THESIS**

**Filip Volarić**

Zagreb, 2017

UNIVERSITY OF ZAGREB  
Faculty of Mechanical Engineering and Naval Architecture

**VALIDATION OF RIGID BODY MOTION AND  
COMPUTATIONAL FLUID DYNAMICS IN SPECTRAL  
SPACE**

Supervisor:  
Prof. Hrvoje Jasak, PhD

Student:  
Filip Volarić

Zagreb, 2017

I hereby declare that this thesis is entirely the result of my own work except where otherwise indicated. I have fully cited all used sources and I have only used the ones given in the list of references

I am eminently thankful to Professor Hrvoje Jasak for allowing me to pursue and accomplish this thesis.

I would like to express my sincere gratitude to Inno Gatin for his time, patience and valuable advice. Without his knowledge and experience this thesis would not be possible.

I express my sincere gratitude to my parents and to my sister for all the support they have provided me over the years. Thank you for your patience and for being of such great support.

Finally I would like to thank my friends and colleagues with whom I spent countless hours in a positive working environment on the 8th floor.

Thank you,  
Filip Volarić



SVEUČILIŠTE U ZAGREBU  
**FAKULTET STROJARSTVA I BRODOGRADNJE**



Središnje povjerenstvo za završne i diplomske ispite  
Povjerenstvo za diplomske ispite studija strojarstva za smjerove:  
procesno-energetski, konstrukcijski, brodstrojarski i inženjersko modeliranje i računalne simulacije

Sveučilište u Zagrebu	
Fakultet strojarstva i brodogradnje	
Datum: -11- 2017	Prilog
Klasa: 602-04/17-G/4	
Ur. broj: 15-1703-17-442	

## DIPLOMSKI ZADATAK

Student: **Filip Volarić**

Mat. br.: 0035190377

Naslov rada na hrvatskom jeziku:

**Validacija sprege gibanja krutog tijela i računalne dinamike fluida u frekvencijskoj domeni**

Naslov rada na engleskom jeziku:

**Validation of Rigid Body Motion and Computational Fluid Dynamics in Spectral Space**

Opis zadatka:

The Harmonic Balance (HB) method in Computational Fluid Dynamics (CFD) approaches the problem of transient quasi-periodic flows via spectral decomposition of a time signal within the Finite Volume (FV) framework. While HB is usually applied to turbulent compressible single phase flows in turbomachinery, it is also applicable to two-phase free surface flows encountered in the field of marine engineering. In predictions of added resistance it is necessary to account for the coupling between fluid flow and motion of the marine object. In order to predict the rigid body motion in conjunction with the HB method, a spectral rigid body motion algorithm is developed. In this study, the candidate shall investigate and validate the spectral rigid body motion algorithm, coupled with the HB fluid flow solution method.

The candidate shall perform the following tasks within this project:

- Perform a literature survey on spectral methods in CFD, including HB and other variants;
- Perform a detailed mathematical investigation of the spectral rigid body motion algorithm;
- Suggest possible improvements of the existing implementation of the spectral rigid body motion algorithm;
- Perform simple two-dimensional simulations of a moving body in two-phase flow with surface waves,
- Perform a validation of the spectral rigid body motion simulation by comparing the results with the transient method,
- Present the comparison of results and computational time for the spectral and transient solution.

The Thesis shall list the bibliography and any assistance received during this study.

Zadatak zadan:

28. rujna 2017.


Datum predaje rada:

30. studenog 2017.

Predviđeni datum obrane:

6., 7. i 8. prosinca 2017.

Zadatak zadao:

  
Prof. dr. sc. Hrvoje Jasak

Predsjednica Povjerenstva:

  
Prof. dr. sc. Tanja Jurčević Lulić

# Table of Contents

<b>List of Figures</b>	<b>III</b>
<b>List of Tables</b>	<b>IV</b>
<b>Nomenclature</b>	<b>V</b>
<b>Abbreviations</b>	<b>IX</b>
<b>Abstract</b>	<b>X</b>
<b>Sažetak</b>	<b>XI</b>
<b>Prošireni sažetak (Extended Abstract in Croatian)</b>	<b>XII</b>
<b>1 Introduction</b>	<b>1</b>
<b>2 Mathematical model</b>	<b>3</b>
2.1 Introduction . . . . .	3
2.2 Governing equations . . . . .	3
2.3 SWENSE decomposition . . . . .	5
2.4 Harmonic balance method . . . . .	6
2.4.1 Implicit coupling of the HB source term . . . . .	9
2.5 Governing equations in the HB form . . . . .	11
2.6 Closure . . . . .	12
<b>3 Rigid body dynamics</b>	<b>13</b>
3.1 Introduction . . . . .	13
3.2 Determination of the rigid body position . . . . .	13
3.2.1 Determination of the body position in the frequency domain . . . . .	14
3.3 Determination of a rigid body orientation . . . . .	16
3.3.1 Determination of the body orientation in the frequency domain . . . . .	19
3.4 Forces acting on a rigid body . . . . .	21
3.5 Closure . . . . .	22
<b>4 Validation of spectral rigid body motion</b>	<b>23</b>
4.1 Introduction . . . . .	23
4.2 Translation . . . . .	24
4.3 Rotation . . . . .	26
4.4 Setup of the numerical simulation . . . . .	28
4.5 Results of numerical simulations . . . . .	29

---

4.5.1	Translation . . . . .	29
4.5.2	Rotation . . . . .	33
4.6	Closure . . . . .	37
<b>5</b>	<b>Motion validation of a submerged body</b>	<b>38</b>
5.1	Introduction . . . . .	38
5.2	Design of the test case . . . . .	38
5.3	Numerical case set up . . . . .	41
5.3.1	Discretised computational domain . . . . .	41
5.3.2	Relaxation zones . . . . .	42
5.3.3	Wave parameters . . . . .	42
5.3.4	Boundary conditions . . . . .	43
5.3.5	Simulation properties . . . . .	43
5.4	Reference transient simulation . . . . .	44
5.5	Comparison of the HB and transient simulation results . . . . .	46
5.6	Conclusion . . . . .	53
<b>6</b>	<b>Conclusion and Future Work</b>	<b>54</b>
	<b>References</b>	<b>55</b>

## List of Figures

4.1	Computational domain for the validation of translational motion. . . . .	24
4.2	Validation of pitch rotation . . . . .	26
4.3	First validation test case mesh . . . . .	28
4.4	Convergence of Fourier coefficients in the 9th simulation. . . . .	30
4.5	Time domain variables during one period in the 9th simulation. . . . .	31
4.6	Convergence of Fourier coefficients in the 18th simulation. . . . .	34
4.7	Time domain variables during one period in the 18th simulation. . . . .	35
5.1	Divergence of trapezoidal body simulation. . . . .	39
5.2	Dimensions of the rigid body. . . . .	39
5.3	Computational domain dimensions for the transient simulation. . . . .	40
5.4	Existence of mean value of motion. . . . .	40
5.5	Computational domain dimensions for the Harmonic Balance (HB) simulation. . . . .	41
5.6	Full view of the mesh. . . . .	41
5.7	Zoomed view of the mesh in the middle of domain. . . . .	42
5.8	Relaxation zones represented with a weight field. . . . .	42
5.9	Time signal of the rigid body position. . . . .	45
5.10	Periodic convergence of the position Fourier coefficients. . . . .	45
5.11	Time signal of the force acting on the rigid body. . . . .	46
5.12	Periodic convergence of force Fourier coefficients. . . . .	46
5.13	Convergence of the first order position amplitude. . . . .	47
5.14	Convergence of the first order force amplitude. . . . .	48
5.15	Perturbation component of velocity at first time instant . . . . .	49
5.16	Perturbation component of velocity at third time instant . . . . .	50
5.17	Perturbation component of velocity at fifth time instant . . . . .	50
5.18	Perturbation component of velocity at eight time instant . . . . .	51
5.19	Dynamic pressure at sixth time instant . . . . .	51
5.20	Dynamic pressure velocity at ninth time instant . . . . .	52
5.21	Dynamic pressure at eleventh time instant . . . . .	52
5.22	The wake pattern . . . . .	52



## List of Tables

4.1	Forces in the simulations for the translational motion validation. . . . .	29
4.2	Results of the translational validation simulations. . . . .	32
4.3	Torque in simulations for rotational motion validation. . . . .	33
4.4	Results of rotational validation simulations. . . . .	36
5.1	Wave parameters. . . . .	43
5.2	Periodically converged results for first and second harmonic amplitudes of the position and force. . . . .	44
5.3	First and second order harmonic amplitude of the position and force obtained from HB simulation with 6 harmonics. . . . .	47
5.4	Results of the HB simulations with 4 and 6 harmonics and the relative difference towards transient simulation. . . . .	49

## Nomenclature

### Greek letters

$\dot{\omega}$	Angular acceleration	rad / s <sup>2</sup>
$\varepsilon$	Width parameter	-
$\Gamma$	Interface	-
$\kappa$	Mean interface curvature	1 / m
$\nu_e$	Effective kinematic viscosity	m <sup>2</sup> / s
$\nu_{e,a}$	Effective kinematic viscosity of air	m <sup>2</sup> / s
$\nu_{e,w}$	Effective kinematic viscosity of water	m <sup>2</sup> / s
$\omega$	Base angular frequency	rad / s
$\psi_I$	Incident Level Set field	-
$\psi_P$	Perturbation Level Set field	-
$\psi$	Level Set field	-
$\rho_a$	Air density	kg / m <sup>3</sup>
$\rho_w$	Water density	kg / m <sup>3</sup>
$\rho$	Density	kg / m <sup>3</sup>
$\tau$	Time	s
$\underline{\delta u}$	Perturbation of velocity	m / s
$\underline{\omega}$	Angular velocity	rad / s
$\underline{\Omega}_p$	Fourier coefficient of angular velocity	rad / s
$\underline{\xi}$	Variable in exponential mapping	-
$\underline{\Xi}_p$	Fourier coefficient of variable $\underline{\xi}$	-
$\xi_I$	Arbitrary incident field	-
$\xi_P$	Arbitrary perturbation field	-
$\xi$	Arbitrary field	-

**Latin letters**

$\ddot{x}$	Acceleration of a centre of mass	$m / s^2$
$\dot{x}$	Velocity of a centre of mass	$m / s$
$\mathbb{R}$	Real numbers	-
$\mathcal{Q}$	Scalar field in time domain	-
$\mathcal{R}$	Scalar transport equation residual in time domain	-
$\underline{\underline{A}}$	Coefficient matrix	-
$\underline{\underline{C}}$	Rigid body configuration	-
$\underline{\underline{c}}$	Stiffness coefficients matrix	$N / m$
$\underline{\underline{E}}$	Transformation matrix from time to frequency domain	-
$\underline{\underline{E}}^{-1}$	Transformation matrix from frequency to time domain	-
$\underline{\underline{I}}$	Identity matrix	-
$\underline{\underline{J}}$	Tensor of inertia	$kgm^2$
$\underline{\underline{k}}$	Damping coefficients matrix	$Ns / m$
$\underline{\underline{m}}$	Mass matrix	$kg$
$\underline{\underline{R}}$	Rotation matrix	-
$\underline{\underline{Q}}$	Vector of variable $\mathcal{Q}$ in discrete time instants	-
$\underline{c}$	Modified convective velocity	$m / s$
$\underline{f}_d$	Damping force	$N$
$\underline{F}_p$	Fourier coefficient of force	$N$
$\underline{f}_R$	Resultant force acting on a rigid body	$N$
$\underline{f}_s$	Spring force	$N$
$\underline{g}$	Gravitational acceleration	$m / s^2$
$\underline{I}$	Identity vector	-
$\underline{l}$	Resultant torque	$Nm$

$\underline{L}_p$	Fourier coefficient of torque	Nm
$\underline{Q}, \underline{R}$	Fourier coefficient vectors	-
$\underline{S}$	Harmonic Balance temporal coupling vector	-
$\underline{u}_I$	Incident velocity field	m / s
$\underline{u}_P$	Perturbation velocity field	m / s
$\underline{u}$	Velocity field	m / s
$\underline{U}_p$	Fourier coefficient of velocity	m / s
$\underline{x}$	Position vector of a centre of mass	m
$\underline{x}$	Radii vector	m
$\underline{X}_p$	Fourier coefficient of position	m
$b$	Diffusion coefficient	-
$C$	Rigid body configuration	-
$c_x, c_y, c_z$	Stiffness coefficient in the direction of the $x, y$ and $z$ axis	N / m
$Co$	Courant-Friedrich-Lewy number	-
$i$	Imaginary unit	-
$J_{xx}, J_{yy}, J_{zz}$	Principal moments of inertia	kgm <sup>2</sup>
$k_x, k_y, k_z$	Damping coefficient in the direction of the $x, y$ and $z$ axis	Ns / m
$m$	Mass of a rigid body	kg
$N$	Number of harmonics	-
$p_d$	Dynamic pressure	Pa
$P_r$	Coefficient substituting the summation term	-
$Q_{C_l}$	$l$ -th cosine Fourier coefficient of $\mathcal{Q}$	-
$Q_{S_l}$	$l$ -th sine Fourier coefficient of $\mathcal{Q}$	-
$R_{C_l}$	$l$ -th cosine Fourier coefficient of $\mathcal{R}$	-
$R_{S_l}$	$l$ -th sine Fourier coefficient of $\mathcal{R}$	-

---

$SE(3)$	Special Euclidean group	-
$SO(3)$	Special orthogonal group	-
$T$	Base period	s
$t_k$	$k$ -th discrete time instant	s
$U$	Mean convective velocity	m / s

## **Abbreviations**

**SWENSE** Spectral Wave Explicit Navier Stokes Equation

**CFD** Computational Fluid Dynamics

**LS** Level Set

**HB** Harmonic Balance

**FV** Finite Volume

**GFM** Ghost Fluid Method

**FFT** Fast Fourier Transform

**DFT** Discrete Fourier Transform

## Abstract

Over the last decade the Harmonic Balance (HB) method was developed in the field of Computer Fluid Dynamics (CFD). HB method transforms a transient periodic problem into a set of coupled steady-state problems. Although the HB method was first applied to single-phase flows in the field of turbomachinery, it is also applicable to two-phase free surface flows such as the ones that can be found in the field of naval hydrodynamics. In the field of naval hydrodynamic it is very important to accurately assess the drag force of the ship in waves during the design process, so it is necessary to couple fluid flow and motion of the ship. Hence, the HB method can only be used in the assessment of drag force if the corresponding spectral rigid body motion algorithm is developed.

In this thesis HB method is described first, which is used to simulate flow, and then a detailed description of spectral rigid body motion algorithm is given. The new algorithm is validated on two test cases. The results of the first case are compared to an analytical solution, and the results of the second case are compared with a transient simulation.

Keywords: *CFD*, Free Surface Flows, Frequency domain, Harmonic Balance, Rigid Body Dynamics.

## Sažetak

U području računalne dinamike fluida se u posljednjih desetak godina razvija metoda harmoničke ravnoteže koja transformira problem tranzijentnog periodičnog strujanja u sustav međusobno ovisnih stacionarnih problema. Iako se metoda harmoničke ravnoteže najviše razvila za jednofazna strujanja u području turbostrojeva, isti princip može se primjeniti na simulaciju dvofaznih strujanja sa slobodnom površinom koja se javljaju u području brodske hidrodinamike. Tijekom projektiranja forme broda vrlo je bitno dobro procijeniti silu otpora pri plovidbi u valovitom moru, pa je stoga bitno povezati strujanje fluida i gibanje objekta koje je uzrokovano strujanjem. Budući da je razvijena metoda harmoničke ravnoteže za dvofazna strujanja sa slobodnom površinom, potrebno je razviti komplementarnu metodu za proračun gibanja krutog tijela. U ovom radu prvo je dan opis metode harmoničke ravnoteže koja se koristi za simulaciju dvofaznog strujanja, te je nakon toga dan detaljan izvod algoritma za gibanje tijela u frekvencijskoj domeni. Novi algoritam je testiran na dva različita slučaja. Rezultati prvog slučaja su uspoređeni sa analitičkim rješenjem, dok su rezultati drugog slučaja uspoređeni s rješenjem tranzijentne simulacije.

Ključne riječi: Računalna dinamika fluida, Strujanje sa slobodnom površinom, Frekvencijska domena, Metoda harmoničke ravnoteže, Dinamika krutog tijela.



## Prošireni Sažetak

### Uvod

Cilj ovog rada je razviti i validirati metodu za gibanje krutog tijela u frekvencijskoj domeni. Budući da je u računalnoj dinamici fluida već razvijena metoda harmoničke ravnoteže koja preko Fourierove transformacije transformira jedan tranzijentni problem u niz spregnutih stacionarnih problema, sljedeći korak je razvoj kompatibilne metode za gibanje krutog tijela. Budući da je rješavanje strujanja fluida i gibanja krutog tijela povezano, u ovom radu su prvo dane jednačbe za strujanje fluida, a nakon toga jednačbe za gibanje tijela. Nadalje će biti prikazani rezultati validacije razvijenog algoritma na dva testna slučaja. Algoritam je razvijen unutar foam-extend softwera za računalnu dinamiku fluida [1].

### Matematički model

#### Osnovne jednačbe

Matematički model korišten za modeliranje nestlačivog, turbulentnog, dvofaznog strujanja dva fluida sa "oštrom" granicom sastoji se od jednačbe očuvanja mase, jednačbe očuvanja količine gibanje i Level Set [2] jednačbe kojom se prati pozicija slobodne površine. Te jednačbe su prvo dane u osnovnom obliku, a zatim će na njih biti primijenjena metoda SWENSE (eng. "Spectral Wave Explicit Navier-Stokes", skraćeno SWENSE) [3] razlaganja rješenja, da bi na kraju osnovne jednačbe bile dane vremensko-spektralnoj formi.

Granica  $\Gamma$  razdvaja dvije faze (u ovom radu vodu i zrak), od kojih svaka ima konstantnu gustoću,  $\rho = \rho_w$  u vodi i  $\rho = \rho_a$  u zraku. Uzimajući u obzir konstantnost gustoće po fazama i kontinuiranost polja brzine zbog kinematskog rubnog uvjeta na slobodnoj površini, jednačba očuvanja mase glasi:

$$\nabla \cdot \underline{u} = 0. \quad (1)$$

Prema Vukčević et al [3] zakon očuvanja količine gibanja za nestlačivo turbulentno dvofazno strujanje glasi:

$$\frac{\partial \underline{u}}{\partial t} + \nabla \cdot (\underline{u}\underline{u}) - \nabla \cdot (\nu_e \nabla \underline{u}) = -\frac{1}{\rho} \nabla p_d + \nabla \underline{u} \cdot \nabla \nu_e, \quad (2)$$

gdje je  $\nu_e$  efektivna kinematska viskoznost koja uključuje i turbulentnu viskoznost,  $\rho$  je gustoća koja ima diskontinuitet na slobodnoj površini,  $p_d$  polje dinamičkog tlaka:  $p_d = p - \rho \underline{g} \cdot \underline{x}$ , gdje  $p$  označava totalni tlak,  $\underline{g}$  gravitacijsko ubrzanje, a  $\underline{x}$  radij vektor.

Pozicija slobodne površine dobiva se korištenjem Level Set metode [2] koja je pogodna za primjenu uz SWENSE dekompoziciju:

$$\frac{\partial \psi}{\partial t} + \nabla \cdot (\underline{c}\psi) - \psi \nabla \cdot \underline{c} - b \nabla \cdot (\nabla \psi) = b \frac{\sqrt{2}}{\varepsilon} \tanh\left(\frac{\psi}{\varepsilon \sqrt{2}}\right). \quad (3)$$

U jednadžbi (3)  $b$  i  $\varepsilon$  su numerički parametri:  $b$  je koeficijent difuzije, dok je  $\varepsilon$  je parameter širine razmazivanja.  $\underline{c}$  je modificirana konvektivna brzina:

$$\underline{c} = \underline{u} + b \frac{\sqrt{2}}{\varepsilon} \tanh\left(\frac{\psi}{\varepsilon \sqrt{2}}\right) \nabla \psi + b \kappa \frac{\nabla \psi}{|\nabla \psi|}, \quad (4)$$

Da bi matematički model bio potpun potrebno je uzeti u obzir rubne uvjete na slobodnoj površini. Ghost Fluid metoda (GFM) [4] koja se koristi u ovom radu implicitno uzima u obzir diskontinuitete gradijenta tlaka i gustoće na slobodnoj površini zadovoljavajući kinematski i dinamički rubni uvjet slobodne površine. Kinematskim rubnim uvjetom slobodne površine propisano je kontinuirano polje brzine na slobodnoj površini, odnosno jednakost polja brzine koje se nalazi infinitezimalno blizu slobodnoj površini u težem fluidu s poljem brzine u infinitezimalnoj blizini slobodne površini u lakšem fluidu<sup>1</sup>:

$$[\underline{u}] = \underline{u}^- - \underline{u}^+ = 0. \quad (5)$$

Dinamičkim rubnim uvjetom propisana je ravnoteža naprezanja na slobodnoj površini koja se mogu podijeliti na normalnu komponentu koja nastaje zbog tlaka i na tangencijalnu komponentu koja nastaje zbog viskoznih naprezanja. GFM korištena u ovom radu uzima u obzir skok gradijenta tlaka zbog skoka gustoće na slobodnoj površini koji se može izraziti kao:

$$[\rho] = \rho^- - \rho^+, \quad (6)$$

dok zanemaruje utjecaje površinske napetosti. Zanemarenjem površinske napetosti dobivamo uvjet diskontinuiranog polja tlaka koji se uvođenjem dinamičkog tlaka može zapisati u sljedećem obliku:

$$[pd] = -[\rho] \underline{g} \cdot \underline{x}. \quad (7)$$

Tangencijalna naprezanja su aproksimirana linearnom interpolacijom kinematske viskoznosti na slobodnoj površini:

$$\underline{v}_e = \alpha \underline{v}_{e,w} + (1 - \alpha) \underline{v}_{e,a}. \quad (8)$$

Linearna interpolacija kinematske viskoznosti opravdana je za dvofazna strujanja sa slobodnom površinom na velikim prostornim skalama korištena u ovom radu [5].

Iz jednadžbe 2 zbog kontinuiranog polja brzine  $\underline{u}$  i pretpostavljene kontinuiranosti kinematičke viskoznosti  $\underline{v}_e$  proizlazi dodatni uvjet skoka:

<sup>1</sup>U svim jednadžbama vezanima uz GFM oznaka  $^+$  označuje teži fluid, a  $^-$  lakši.

$$\left[ \frac{1}{\rho} \nabla p_d \right] = 0, \quad (9)$$

kojeg je prema nekim autorima nužno uzeti u obzir [3].

### Osnovne jednadžbe u SWENSE obliku

SWENSE razlaganje temelji se na rastavljanju proizvoljnog polja  $\xi$  na nailaznu  $\xi_I$  i na perturbiranu  $\xi_P$  komponentu:

$$\xi = \xi_I + \xi_P. \quad (10)$$

Svrha SWENSE razlaganja je opisivanje glavnih značajki valova na slobodnoj površini sa modelom potencijalnog strujanja iz kojeg proizlazi polje  $\xi_I$  te naknadno dodavanje nelinearnih, viskoznih i turbulentnih efekata poljem  $\xi_P$ . Iako je izbor nailaznog polja  $\xi_I$  proizvoljan, pretpostavlja se da ono predstavlja dobru procjenu potpunog rješenja. U nastavku će biti dane osnovne jednadžbe koje su dobivene razlaganjem jednadžbi (1), (2) i (3) danih u prethodnom poglavlju. Napomena, sva nailazna polja nastala razlaganjem dobivaju indeks  $I$  dok sva perturbirana polja dobivaju indeks  $P$ .

Razlaganjem jednadžbe (1) dobiva se jednadžba kontinuiteta u SWENSE obliku:

$$\nabla \cdot \underline{u}_P = -\nabla \cdot \underline{u}_I. \quad (11)$$

iako je polje brzine u potencijalnom strujanju solenoidalno,  $\nabla \cdot \underline{u}_I = 0$ , divergencija nailaznog polja brzine se zadržava jer se s tim članom se u jednadžbi (11) rješavaju greške kontinuiteta nastale mapiranjem tog polja na diskretiziranu proračunsku domenu.

Razlaganjem jednadžbe (2) dobiva se zakon očuvanja količine gibanja u SWENSE obliku:

$$\begin{aligned} \frac{\partial \underline{u}_P}{\partial t} + \nabla \cdot (\underline{u} \underline{u}_P) - \nabla \cdot (\underline{v}_e \nabla \underline{u}_P) = \\ - \frac{\partial \underline{u}_I}{\partial t} - \nabla \cdot (\underline{u} \underline{u}_I) + \nabla \cdot (\underline{v}_e \nabla \underline{u}_I) - \frac{1}{\rho} \nabla p_d + \nabla \underline{u} \cdot \nabla \underline{v}_e. \end{aligned} \quad (12)$$

U jednadžbi (12) se može uočiti da nisu sva polja razložena: polje brzine  $\underline{u}$  u konvektivnom članu, dinamički tlak  $p_d$  tj. gradijent dinamičkog tlaka te član  $\nabla \underline{u} \cdot \nabla \underline{v}_e$ . Razlog tome leži u različitom tretiranju tih članova u numeričkom postupku. Konvektivna brzina nije razložena zbog linearizacije konvektivnog člana s eksplicitnim volumskim protokom iz prethodnog vremenskog koraka. Član  $\nabla \underline{u} \cdot \nabla \underline{v}_e$  nije razložen jer se tretira eksplicitno u numeričkom algoritmu, dok se gradijent dinamičkog tlaka tretira u skladu s GFM metodom pa nije potrebno njegovo razlaganje.

Level Set jednadžbu u SWENSE obliku dobivamo razlaganjem jednadžbe (3):

$$\begin{aligned} \frac{\partial \psi_P}{\partial t} + \nabla \cdot (\underline{c} \psi_P) - \psi_P \nabla \cdot \underline{c} - b \nabla \cdot (\nabla \psi_P) = \\ - \frac{\partial \psi_I}{\partial t} - \nabla \cdot (\underline{c} \psi_I) + \psi_I \nabla \cdot \underline{c} + b \nabla \cdot (\nabla \psi_I) + b \frac{\sqrt{2}}{\varepsilon} \tanh \left( \frac{\psi}{\varepsilon \sqrt{2}} \right). \end{aligned} \quad (13)$$

Modificirana konvektivna brzina  $\underline{c}$  nije podložna razlaganju iz istog razloga kao i brzina  $\underline{u}$  u jednadžbi (12). Također član  $b \frac{\sqrt{2}}{\varepsilon} \tanh \left( \frac{\psi}{\varepsilon \sqrt{2}} \right)$  nije razložen jer se tretira eksplicitno u numeričkom algoritmu.

### Osnovne jednadžbe u HB obliku

Metoda harmoničke ravnoteže [6, 5] koristi se kod vremenski periodičkih strujanja s izraženom baznom frekvencijom za transformaciju tranzijentnog problema u niz spregnutih stacionarnih problema. Tranzijentne jednadžbe su transformirane u niz stacionarnih jednadžbi koje su povezane izvorskim članom koji predstavlja vremensku derivaciju u frekvencijskoj domeni. Osnovni uvjet za primjenu metode harmoničke ravnoteže je vremenski osrednjeno strujanje u kojem je moguće svaku varijablu razviti u Fourierov niz sa konačnim brojem harmonika  $N$ :

$$\mathcal{Q}(t) = Q_0 + \sum_{l=1}^N (Q_{C_l} \cos(l\omega t) + Q_{S_l} \sin(l\omega t)), \quad (14)$$

gdje  $\mathcal{Q}$  predstavlja polje u vremenskoj domeni,  $Q$  Fourierov koeficijent tog polja u frekvencijskoj domeni, indeksi  $S_l$  i  $C_l$  predstavljaju sinusni odnosno kosinusni Fourierov koeficijent, a  $\omega$  je poznata bazna frekvencija polja  $q$ .

Standardna transportna jednadžba u vremenskoj domeni ima sljedeći oblik:

$$\frac{\partial \mathcal{Q}}{\partial t} + \mathcal{R} = 0, \quad (15)$$

gdje je  $\mathcal{R}$  predstavlja konvektivni, difuzijski i izvorski član:

$$\mathcal{R} = \nabla \cdot (\underline{u} \mathcal{Q}) - \nabla \cdot (\gamma \nabla \mathcal{Q}) - S_{\mathcal{Q}}. \quad (16)$$

Uz razvijanje polja  $\mathcal{Q}$  i  $\mathcal{R}$  u Fourierov niz te primjenom matričnog prikaza diskretne Fourierove transformacije (DFT),  $\underline{Q} = \underline{E} \underline{\mathcal{Q}}$ , standardna transportna jednadžba poprima sljedeći oblik:

$$\omega \underline{E}^{-1} \underline{A} \underline{E} + \underline{\mathcal{R}} = 0. \quad (17)$$

Jednadžba (17) predstavlja skup kvazi-stacionarnih jednadžbi spregnutih elementima izvan glavne dijagonale matrice  $\underline{E}^{-1} \underline{A} \underline{E}$ . Usporedbom jednadžbi (15) i (17) primjećuje se da je

vremenska derivacija zamijenjena izvorskim članom koji veze jednadžbe u spregnuti sistem:

$$\begin{aligned} S(\underline{\mathcal{Q}}) &= \omega \underline{E}^{-1} \underline{A} \underline{E} \underline{\mathcal{Q}}, \\ S_l(\underline{\mathcal{Q}}) &= -\frac{2\omega}{2N+1} \left( \sum_{k=1}^{2N} P_{k-l} \mathcal{Q}_{t_k} \right), \text{ za } l = 1 \dots 2N+1, \end{aligned} \quad (18)$$

gdje je  $S(\underline{\mathcal{Q}})$  vektor izvorskih članova u kojem je  $S_l$   $l$ -ti element u vektoru.  $P$  je konstantna matrica definirana kao:

$$P_r = \sum_{m=1}^N r \sin(rm\omega\Delta t), \text{ za } r = -N \dots N, \quad (19)$$

za  $\Delta t = T/(2N+1)$ .

Može se vidjeti da se metodom harmoničke ravnoteže tranzijentni problem transformira u skup  $2N+1$  spregnutih kvazi-stacionarnih problema koji se rješavaju u jednako razmaknutim vremenskim trenucima perioda  $T$ . Stacionarne jednadžbe su spojene preko izvorskog člana opisanog jednadžbom (18) koji zamjenjuje vremensku derivaciju iz tranzijentne jednadžbe, dok su konvektivni, difuzijski i izvorski članovi iz tranzijentne jednadžbe ostali nepromijenjeni. U nastavku će biti dane osnovne jednadžbe u HB obliku.

U jednadžbi kontinuiteta (11) nema člana s vremenskom derivacijom pa je oblik jednadžbe nepromijenjen, jedina razlika je da se polje brzine sada računa u jednako razmaknutim vremenskim trenucima unutar jednog vremenskog perioda što rezultira sa  $2N+1$  međusobno nezavisnih jednadžbi kontinuiteta za svaki izabrani vremenski trenutak:

$$\nabla \cdot \underline{u}_{P,l} = -\nabla \cdot \underline{u}_{I,l}, \quad l = 1 \dots 2N+1. \quad (20)$$

U zakonu očuvanja količine gibanja (12) postoje dva člana s vremenskom derivacijom koje je potrebno zamijeniti sa HB izvorskim članovima danim jednadžbom (18):

$$\begin{aligned} S_l(\underline{u}_P) + \nabla \cdot (\underline{u}_I \underline{u}_{P,l}) - \nabla \cdot (\underline{v}_{e_l} \nabla \underline{u}_{P,l}) = \\ -S_l(\underline{u}_I) - \nabla \cdot (\underline{u}_I \underline{u}_{I,l}) + \nabla \cdot (\underline{v}_{e_l} \nabla \underline{u}_{I,l}) - \frac{1}{\rho_l} \nabla p_{d,l} + \nabla \underline{u}_I \cdot \nabla \underline{v}_{e_l}, \quad l = 1 \dots 2N+1. \end{aligned} \quad (21)$$

Potrebno je primijetiti da svaka jednadžba ima odgovarajuća polja gustoće  $\rho_l$  i efektivne kinematske viskoznosti  $\underline{v}_{e_l}$ . Budući da su dva HB izvorska člana u jednadžbi (21) linearni operatori moguće ih je staviti u jedan član, međutim to nije napravljeno jer se izvorski član perturbiranog polja brzine  $\underline{u}_P$  tretira implicitno dok se izvorski član incidentnog polja brzine  $\underline{u}_I$  tretira eksplicitno.

Level Set jednadžba (13) kao i zakon očuvanja količine gibanja ima dva člana sa vremenskim derivacijama koja je potrebno zamijeniti sa HB izvorskim članom danim

jednadžbom (18):

$$\begin{aligned} S_I(\psi_P) + \nabla \cdot (\underline{c}_I \psi_{P_I}) - \psi_{P_I} \nabla \cdot \underline{c}_I - b \nabla \cdot (\nabla \psi_{P_I}) = \\ - S_I(\psi_I) - \nabla \cdot (\underline{c}_I \psi_{I_I}) + \psi_{I_I} \nabla \cdot \underline{c}_I + b \nabla \cdot (\nabla \psi_{I_I}) + b \frac{\sqrt{2}}{\varepsilon} \tanh \left( \frac{\psi_I}{\varepsilon \sqrt{2}} \right). \end{aligned} \quad (22)$$

Dva HB izvorska člana je moguće spojiti u jedan, međutim to nije napravljeno radi implicitnog tretiranja perturbacijskog polja.

## Dinamika krutog tijela

Jedan od problema dinamike krutog tijela je određivanje njegove konfiguracije. Konfiguracija tijela je poznata ako je poznata njegova pozicija i orijentacija.

Pozicija centra masa krutog tijela  $\underline{x}$  određuje se rješavanjem Newtonove jednadžbe:

$$\underline{m} \underline{a} = \underline{f}_R, \quad (23)$$

gdje je  $m$  masa tijela,  $\underline{a}$  ubrzanje centra masa krutog tijela, a  $f_R$  rezultantna sila koja djeluje u centru masa.

Radi uključenja efekta opruge i viskoznog prigušivača, jednadžbu (23) je potrebno modificirati. Izuzimanjem sile u opruzi i sile u prigušivaču iz rezultantne sile te uzimanjem u obzir smjer djelovanja tih sila jednadžba (23) poprima sljedeći oblik:

$$\underline{m} \underline{\ddot{x}} + \underline{k} \underline{\dot{x}} + \underline{c} \underline{x} = \underline{f}, \quad (24)$$

gdje je  $\underline{m}$  dijagonalna matrica s iznosima mase na dijagonali,  $\underline{c}$  je dijagonalna matrica koeficijenata krutosti, a  $\underline{k}$  je dijagonalna matrica koeficijenata viskoznog prigušenja. Nadalje,  $\underline{x}$  je vektor položaja centra masa krutog tijela,  $\underline{\dot{x}}$  je vektor relativne brzine, dok je  $\underline{\ddot{x}}$  vektor akceleracije.

Da bi mogli gibanje tijela rješavati u frekvencijskoj domeni potrebno je sve vremenski ovisne varijable u jednadžbi (24) razviti u Fourierov niz. Ovdje se koristi razvoj u konačni kompleksni Fourierov niz. Općenitu varijablu  $q(t)$  razvijamo u kompleksni Fourierov niz prema:

$$q(t) = Q_0 + \sum_{p=1}^N Q_p e^{ip\omega t}, \quad (25)$$

gdje je  $i$  imaginarna jedinica  $i = \sqrt{-1}$ ,  $Q_p$  kompleksna amplituda  $p$ -tog harmonika, a  $\omega$  bazna frekvencija. Kao što se može vidjeti u jednadžbi (24) postoje i derivacije vremenske varijable pa je potrebno derivirati Fourierov niz (jednadžba 25). Prva derivacija je definirana kao:

$$\dot{q}(t) = \sum_{p=1}^N ip\omega Q_p e^{ip\omega t}, \quad (26)$$

dok je druga derivacija definirana kao:

$$\ddot{q}(t) = \sum_{p=1}^N -p^2 \omega^2 Q_p e^{ip\omega t}. \quad (27)$$

Razvojem u kompleksni Fourierov red pomaka  $\underline{x}$  i njegovih derivacija te njihovim uvrštavanjem u jednadžbu (24) dobivamo jednadžbu translacijskog gibanja krutog tijela u frekvencijskoj domeni. Sređivanjem te grupiranjem članova uz isti harmonik dobiva se izraz za izračun Fourierovih koeficijenata pomaka krutog tijela u frekvencijskoj domeni:

$$X_{pj} = \frac{F_{pj}}{-mp^2 \omega^2 + ip\omega k_j + c_j}, \quad p = 1 \dots N \text{ i } j = x, y, z, \quad (28)$$

gdje je  $\underline{X}_p$  vektor Fourierovih koeficijenata pomaka u smjeru koordinatnih osi  $p$ -tog harmonika.

Nakon izračuna Fourierovih koeficijenata pomaka moguće je na temelju definicije brzine  $\underline{u}$  kao trenutne promjene vektora položaja:

$$\underline{u} = \frac{d\underline{x}}{dt}, \quad (29)$$

te primjene kompleksnog Fourierovog niza dobiti izraz za određivanje Fourierovih koeficijenata brzine:

$$\underline{U}_p = ip\omega \underline{X}_p, \quad \text{za } p = 1 \dots N, \quad (30)$$

gdje je  $\underline{U}_p$  vektor Fourierovih koeficijenata brzine u smjeru koordinatnih osi  $p$ -tog harmonika.

Nakon određivanja pozicije tijela potrebno je odrediti i njegovu orijentaciju da bi u potpunosti znali konfiguraciju tijela. Orijehtacija tijela je jednoznačno određena matricom rotacije  $\underline{R} \in SO(3)$ .  $SO(3)$  grupa kojoj pripada matrica rotacije je također i Liejeva grupa pa se u skladu s radom Müllera i Terzea [7] matrica rotacija može računati kao:

$$\underline{R} = \underline{I} + \frac{\sin \|\underline{\xi}\|}{\|\underline{\xi}\|} \underline{\xi} + \frac{1 - \cos \|\underline{\xi}\|}{\|\underline{\xi}\|^2} \underline{\xi}^2, \quad (31)$$

gdje je  $\underline{I}$  jedinična matrica, a  $\underline{\xi}$  je moguće odrediti iz kutne brzine  $\underline{\omega}$ :

$$\dot{\underline{\xi}} = \underline{\omega}. \quad (32)$$

Jednadžba (32) nam osigurava drugi red točnosti.

Iz jednadžbe (32) je vidljivo da je za određivanje vektora  $\underline{\xi}$  a time i matrice rotacije  $\underline{R}$  potrebno odrediti kutnu brzinu  $\underline{\omega}$ . Kutnu brzinu određujemo iz Eulerove jednadžbe koja opisuje

rotacijsko gibanje krutog tijela:

$$\underline{J}\dot{\underline{\omega}} + \underline{\omega} \times \underline{J}\underline{\omega} = \underline{l}, \quad (33)$$

gdje je  $\underline{J}$  tenzor inercije krutog tijela,  $\underline{\omega}$  je kutna brzina, a  $\underline{l}$  rezultatni moment koji djeluje na tijelo.

U ovom radu gibanje se rješava u koordinatnom sustavu vezanom za tijelo. Koordinatni sustav vezan za tijelo ima ishodište u centru masa tijela jer su u tom slučaju jednadžbe za translaciju i rotaciju nisu spregnute. Također budući da je u ovom rješavaču tenzor inercije  $\underline{J}$  definiran kao dijagonalan tenzor, lokalni koordinatni sustav mora biti orijentiran prema glavnim osima inercije. Jednadžba (33) zapisana u matričnoj formulaciji glasi:

$$\underline{I}\dot{\underline{\omega}} + \underline{\tilde{\omega}}\underline{I}\underline{\omega} = \underline{l}, \quad (34)$$

gdje je  $\underline{\tilde{\omega}}$  antisimetrična matrica oblika:

$$\underline{\tilde{\omega}} = \begin{bmatrix} 0 & -\omega_z & \omega_y \\ \omega_z & 0 & -\omega_x \\ -\omega_y & \omega_x & 0 \end{bmatrix}, \quad (35)$$

koja se koristi za izračun vektorskog produkta.

Analogno Newtonovoj jednadžbi i Eulerovu jednadžbu (34) je potrebno zapisati u frekvencijskoj domeni. Primjenom raspisa kutne brzine  $\underline{\omega}$  i njene derivacije  $\dot{\underline{\omega}}$  u kompleksni Fourierov niz prema jednadžbama (26) i (27), Eulerova jednadžba po komponentama poprima sljedeću formu (u frekvencijskoj domeni):

$$\begin{aligned} \Omega_{p_x} &= \frac{1}{ip\omega J_{xx}} \left[ L_{p_x} + (J_{yy} - J_{zz}) \sum_{k=0}^p \Omega_{p_y} \Omega_{(p-k)_z} \right], \\ \Omega_{p_y} &= \frac{1}{ip\omega J_{yy}} \left[ L_{p_y} + (J_{zz} - J_{xx}) \sum_{k=0}^p \Omega_{p_z} \Omega_{(p-k)_x} \right], \quad \text{za } p = 1 \dots N \\ \Omega_{p_z} &= \frac{1}{ip\omega J_{zz}} \left[ L_{p_z} + (J_{xx} - J_{yy}) \sum_{k=0}^p \Omega_{p_x} \Omega_{(p-k)_y} \right], \end{aligned} \quad (36)$$

gdje su  $\Omega_{p_x}, \Omega_{p_y}$  i  $\Omega_{p_z}$  kompleksni Fourierovi koeficijenti  $p$ -tog harmonika u smjeru osi  $x, y$  i  $z$  od kutne brzine  $\underline{\omega}$ , a  $L_{p_x}, L_{p_y}$  i  $L_{p_z}$  kompleksni Fourierovi koeficijenti  $p$ -tog harmonika u smjeru osi  $x, y$  i  $z$  momenta  $\underline{l}$ .

Iako se matrica rotacije  $\underline{R}$  izračunava u vremenskoj domeni vektor  $\underline{\xi}$  koji je nužan za izračun matrice rotacije dobiva se inverznom Fourierovom transformacijom njegovih Fourierovih koeficijenata iz spektralne domene. Primjenom razvoja varijabli iz jednadžbe (32) u Fourierov niz dobiva se:



$$\Xi_{p_j} = \frac{\Omega p_j}{ip\omega}, \quad \text{za } p = 1 \dots N \text{ i } j = x, y, z, \quad (37)$$

gdje je  $\Xi_{p_j}$  Fourierov koeficijent  $p$ -tog harmonika vektora  $\underline{\xi}$  u smjeru osi  $j$ .

Kruto tijelo mijenja svoju konfiguraciju zbog sila i momenata koji djeluju na njega. Sila koja djeluje na tijelo koje se nalazi u fluidu nastaje zbog dva uzroka: dio sile nastaje zbog tlaka  $f_p$  i dio sile nastaje zbog viskoznih efekata  $f_v$ :

$$\underline{f} = \underline{f}_p + \underline{f}_v. \quad (38)$$

Analogno sili, moment se isto dijeli na dio koji nastaje zbog tlaka i dio koji nastaje zbog viskoznih efekata:

$$\underline{l} = \underline{l}_p + \underline{l}_v. \quad (39)$$

Sile i momenti u vremenskoj domeni se izračunavaju u globalnom Kartezijskom koordinatnom sustavu kao:

$$\underline{f}_p = \sum_{bf} \underline{s}_f p_f + m \underline{g}, \quad (40)$$

$$\underline{f}_v = \sum_{bf} \rho_f \mathbf{v}_{e,f} \underline{s}_f \cdot \underline{T}^*, \quad (41)$$

$$\underline{l}_p = \sum_{bf} \underline{r}_f \times \underline{s}_f p_f, \quad (42)$$

$$\underline{f}_v = \sum_{bf} \underline{r}_f \times \left( \rho_f \mathbf{v}_{e,f} \underline{s}_f \cdot \underline{T}^* \right), \quad (43)$$

gdje  $\sum_{bf}$  označava sumaciju po svim plohama tijela,  $\rho_f$  je odgovarajuća gustoća na rubnoj plohi, a  $\mathbf{v}_{e,f}$  je efektivna kinematska viskoznost.  $\underline{T}^*$  je devijatorski dio tenzora naprezanja  $\underline{T}$ , koji je definiran kao dvostruko simetrični dio  $\nabla \underline{u}$  tenzora. Vektor  $\underline{r}_f$  je vektor položaja koji povezuje trenutnu rubnu plohu i centar masa krutog tijela.

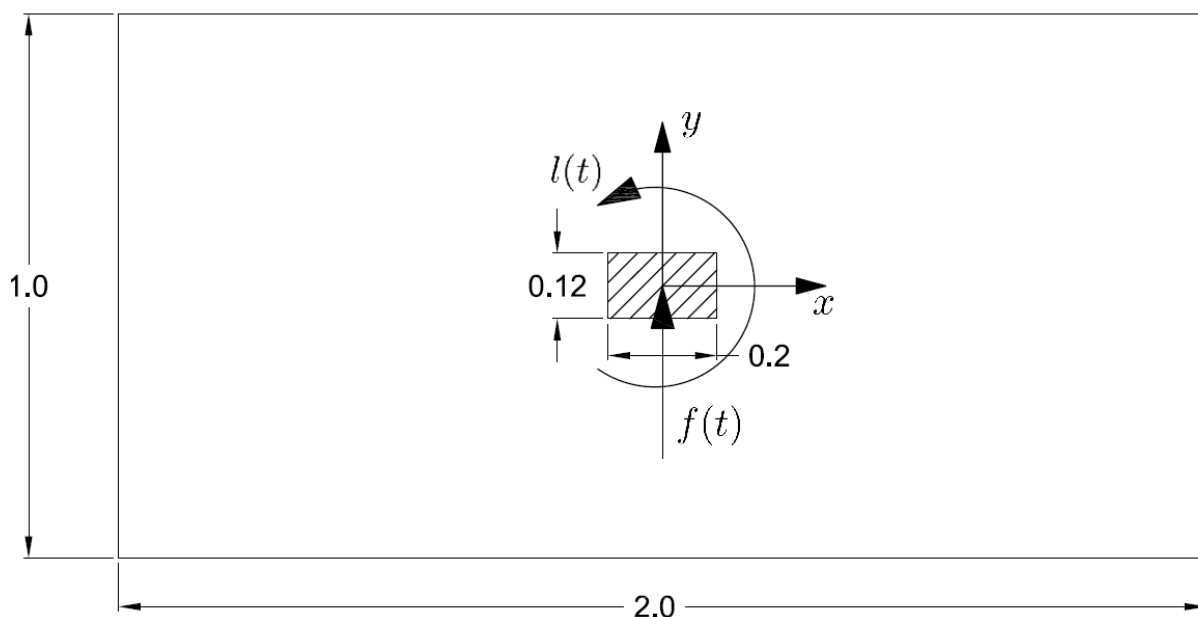
Budući da se polje strujanja rješava sa HB metodom, sve varijable polja strujanja strujanja su izračunata u  $2N + 1$  jednako razmaknutih vremenskih trenutaka perioda  $T$ . Stoga su sile i momenti, za čije su izračunavanje potrebna polja tlaka  $p$  i brzine  $\underline{u}$ , također poznati u diskretnim vremenskim trenucima. Diskretne vrijednosti sile i momenta se transformiraju u frekvencijsku domenu preko diskretne Fourierove transformacije.

## Validacija spektralnog pristupa gibanju krutog tijela

### Validacija gibanja uzrokovano konstantnim silama i momentima

Novi algoritam za izračun gibanja krutog tijela u frekvencijskoj domeni je validiran s dva testna slučaja. U prvom slučaju se rezultati uspoređuju s analitičkim rješenjem. Da bi se moglo odrediti analitičko rješenje koriste se konstantne vrijednosti amplitude sile prilikom simulacije umjesto da se izračunavaju iz polja strujanja. Nadalje, pravokutno tijelo je postavljeno u jednofazno, laminarno i neviskozno strujanje tako da se efekti prigušenja mogu zanemariti. Provedeno je 9 simulacija za validaciju translatorskog gibanja, te također 9 simulacija za validaciju rotacijskog gibanja. Simulacije se razlikuju po iznosima amplituda sila/momenata, te po korištenom redu amplitude sile odnosno momenta.

Dimenzije računalne domene korištene kod simulacija za validaciju prikazane su na slici 1. Oznaka  $f(t)$  označuje silu koja se koristi kod validacije translacijskog gibanja, dok oznaka  $l(t)$  označuje moment koji se koristi kod validacije rotacijskog gibanja.



Slika 1: Računalna domena kod validacije gibanja u frekvencijskoj domeni.

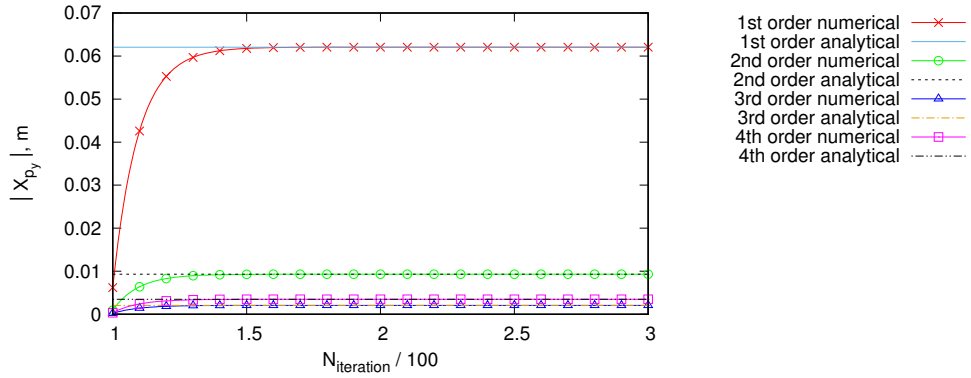
Validacija translacijskog gibanja je provedena s 9 simulacija. Vrijednosti korištenih sila se mogu vidjeti u Tablici 1.

Kao što se može vidjeti iz Tablice 1 složenost korištene sile  $F_{p_y}$  se povećava sa povećanjem indeksa simulacije. Cilj je bio pokrivanje širokog raspona mogućih sila. Sile su dane kao kombinacija prva četiri reda sile, gdje pojam  $p$ -ti red sile označava amplitudu sile  $p$ -tog harmonika. Zadnja simulacija je provedena sa silom koja se sastoji od sva četiri reda sile te ako je njezino poklapanje sa analitičkim rješenjem zadovoljavajuće pretpostavlja se da algoritam radi i za sile viših redova.

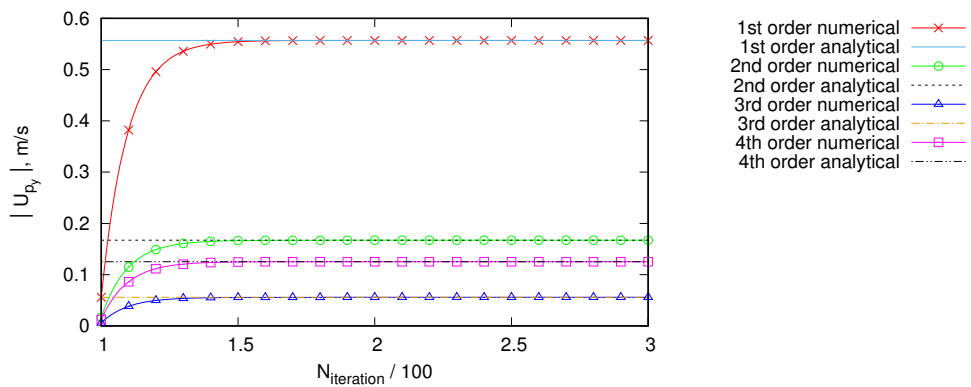
Tablica 1: Sile korištene za validaciju rješenja translatornog gibanje.

Red sile, $p$		1. Red	2. Red	3. Red	4. Red
Simulacija 1	$Re(F_{p_y})$	0	0	0	0
	$Im(F_{p_y})$	1	0	0	0
Simulacija 2	$Re(F_{p_y})$	1	0	0	0
	$Im(F_{p_y})$	0	0	0	0
Simulacija 3	$Re(F_{p_y})$	0	0	0	0
	$Im(F_{p_y})$	40	0	0	0
Simulacija 4	$Re(F_{p_y})$	-40	0	0	0
	$Im(F_{p_y})$	0	0	0	0
Simulacija 5	$Re(F_{p_y})$	30	0	0	0
	$Im(F_{p_y})$	20	0	0	0
Simulacija 6	$Re(F_{p_y})$	0	0	0	0
	$Im(F_{p_y})$	20	15	0	0
Simulacija 7	$Re(F_{p_y})$	-10	20	0	0
	$Im(F_{p_y})$	0	0	0	0
Simulacija 8	$Re(F_{p_y})$	150	0	0	0
	$Im(F_{p_y})$	0	-120	0	0
Simulacija 9	$Re(F_{p_y})$	0	0	15	0
	$Im(F_{p_y})$	50	30	0	45

Iz rezultata u tablici 2 može se vidjeti da numerički rezultati za translacijsko gibanje konvergiraju u analitičko rješenje. Budući da rezultati numeričkih simulacija konvergiraju u pripadajuća analitička rješenja, greška za sve simulacije iznosi 0%. Konvergencija Fourierovih koeficijenata za poziciju  $X_{p_y}$  i brzinu  $U_{p_y}$  je prikazana na grafovima 2a i 2b, dok je usporedba numeričkog i analitičkog rješenja za poziciju  $y$  i brzinu  $u_y$  u vremenskoj domeni dana na grafovima 3a i 3b. Svi grafovi su dani za devetu simulaciju.

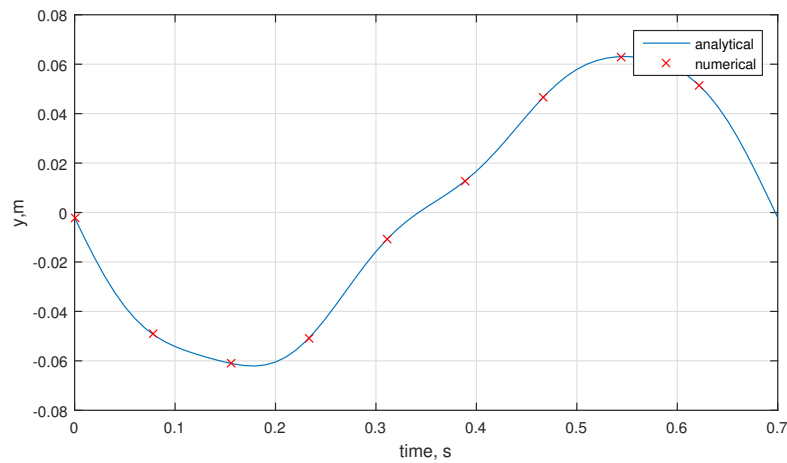


a) Pozicija,

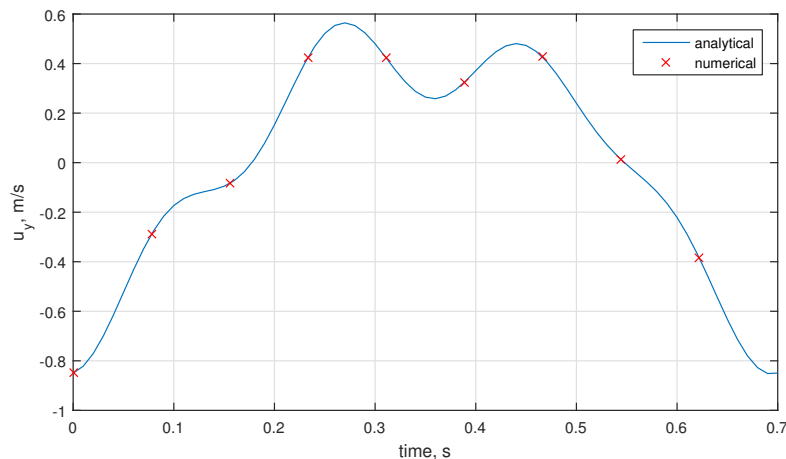


b) Brzina,

Slika 2: Konvergencija Fourierovih koeficijenata u 9. simulaciji.



a) Pozicija,

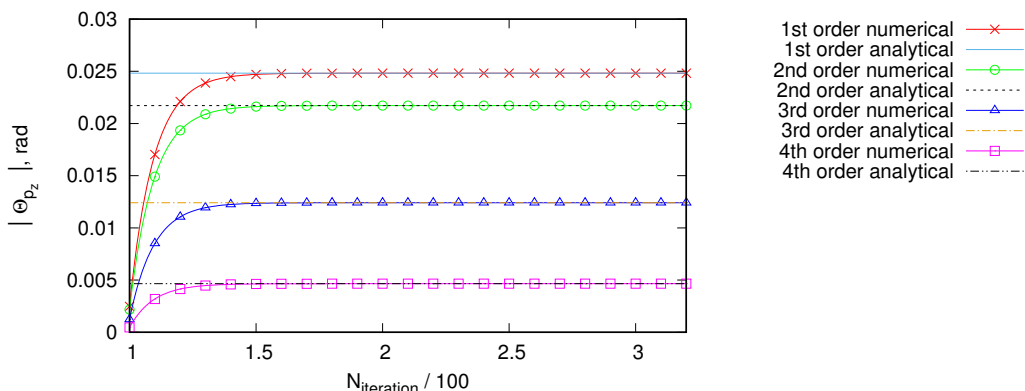


b) Brzina,

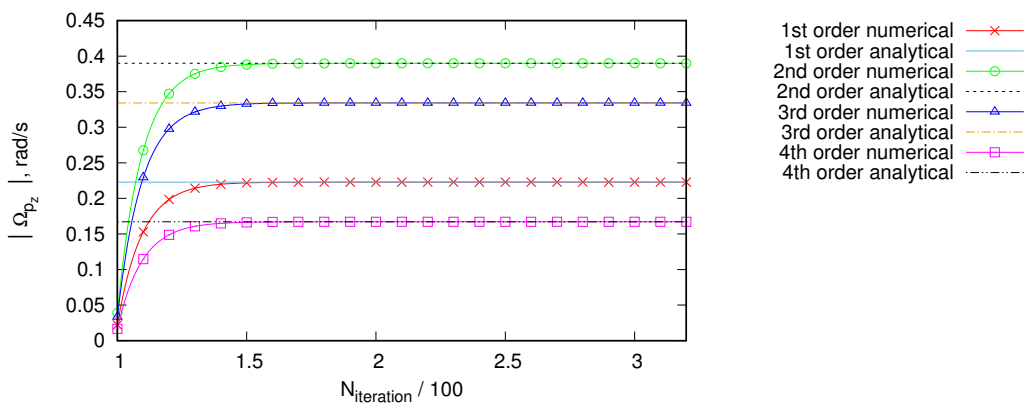
Slika 3: Varijable u vremenskoj domeni tijekom jednog perioda u 9. simulaciji

Momenti koji se koriste za validaciju numeričkog rješenja za rotacijsko gibanje krutog tijela su prikazani u tablici 3. Da bi se izbjegla zabuna između translatorskih i rotacijskih simulacija, rotacijske simulacije se označene rasponom brojeva od 10 do 18. Oznaka  $L_{p_z}$  označava  $p$ -ti red momenta u smjeru osi  $z$ , gdje analogno sili  $p$ -ti red momenta predstavlja amplitudu momenta  $p$ -tog harmonika.

Rezultati simulacija za validaciju rotacijskog gibanja su dani u tablici 4. Iz tih rezultata je vidljivo da numerička rješenja za Fourierove koeficijente Eulerovog kutova  $\Theta_{p_z}$  i kutne brzine  $\Omega_{p_z}$  konvergiraju u analitička rješenja. Zbog konvergencije numeričkih rješenja u analitičke rezultate greška za sve simulacije iznosi 0%. Konvergencija Fourierovih koeficijenata je prikazana na grafovima 4a i 4b. Poklapanje numeričkog i analitičkog rješenja za Eulerov kut  $\theta_z$  i kutnu brzinu  $\omega_z$  u vremenskoj domeni je dano na grafovima 5a i 5b. Svi grafovi su dani za osamnaestu simulaciju.

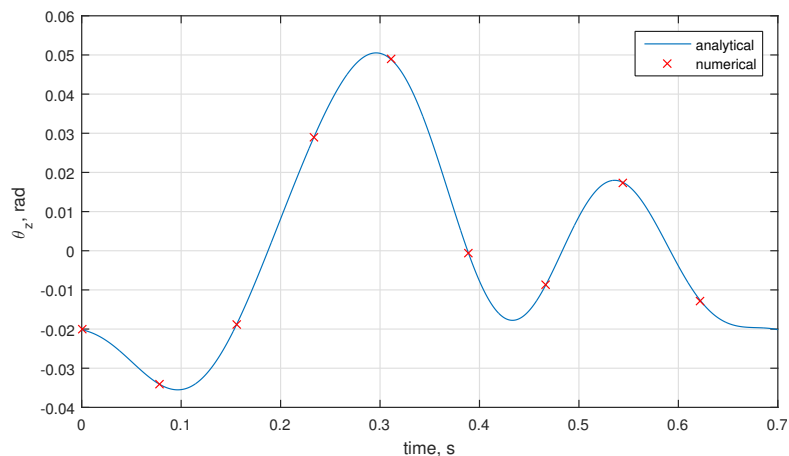


a) Eulerov kut,

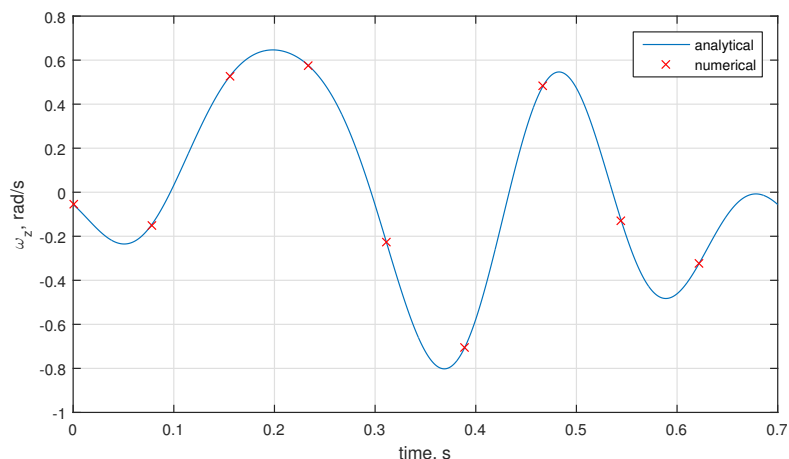


b) Kutna brina,

Slika 4: Konvergencija Fourierovih koeficijenta u 18. simulaciji.



a) Eulerov kut,



b) Kutna brzina,

Slika 5: Varijable u vremenskoj domeni tijekom jednog perioda u 18. simulaciji

Iz prikazanih rezultata se može zaključiti da algoritam za izračun gibanja u frekvencijskoj domeni daje rezultate identične analitičkom rješenju u slučaju da se sile/momenti ne

izračunavaju iz polja strujanja. Naravno potrebno je validirati gibanje u slučaju kada se sile/momenti koji uzrokuju gibanje izračunavaju iz polja strujanja. Stoga su u nastavku dani rezultati drugog testnog slučaja u kojem se validira translatorno gibanje uzrokovano utjecajem površinskih valova.

Tablica 2: Rezultati simulacija za validaciju translacijskog rješenja.

Red, $p$			1. Red	2. Red	3. Red	4. Red
Simulacija 1	$ X_{py} $ , m	numeričko	0.0012411	0	0	0
		analitičko	0.0012411	0	0	0
	$ U_{py} $ , m/s	numeričko	0.0111408	0	0	0
		analitičko	0.0111408	0	0	0
Simulacija 2	$ X_{py} $ , m	numeričko	0.0012411	0	0	0
		analitičko	0.0012411	0	0	0
	$ U_{py} $ , m/s	numeričko	0.0111408	0	0	0
		analitičko	0.0111408	0	0	0
Simulacija 3	$ X_{py} $ , m	numeričko	0.049647	0	0	0
		analitičko	0.049647	0	0	0
	$ U_{py} $ , m/s	numeričko	0.44563	0	0	0
		analitičko	0.44563	0	0	0
Simulacija 4	$ X_{py} $ , m	numeričko	0.049647	0	0	0
		analitičko	0.049647	0	0	0
	$ U_{py} $ , m/s	numeričko	0.44563	0	0	0
		analitičko	0.44563	0	0	0
Simulacija 5	$ X_{py} $ , m	numeričko	0.044751	0	0	0
		analitičko	0.044751	0	0	0
	$ U_{py} $ , m/s	numeričko	0.40168	0	0	0
		analitičko	0.40168	0	0	0
Simulacija 6	$ X_{py} $ , m	numeričko	0.024823	0.22281	0	0
		analitičko	0.024823	0.22281	0	0
	$ U_{py} $ , m/s	numeričko	0.0046544	0.083556	0	0
		analitičko	0.0046544	0.083556	0	0
Simulacija 8	$ X_{py} $ , m	numeričko	0.18617	1.67112	0	0
		analitičko	0.18617	1.67112	0	0
	$ U_{py} $ , m/s	numeričko	0.037235	0.66845	0	0
		analitičko	0.037235	0.66845	0	0
Simulacija 9	$ X_{py} $ , m	numeričko	0.062059	0.00930888	0.0020686	0.0034908
		analitičko	0.062059	0.00930888	0.0020686	0.0034908
	$ U_{py} $ , m/s	numeričko	0.55704	0.16711	0.055704	0.12533
		analitičko	0.55704	0.16711	0.055704	0.12533



Tablica 3: Momenti korišteni za validaciju rješenja rotacijskog gibanje.

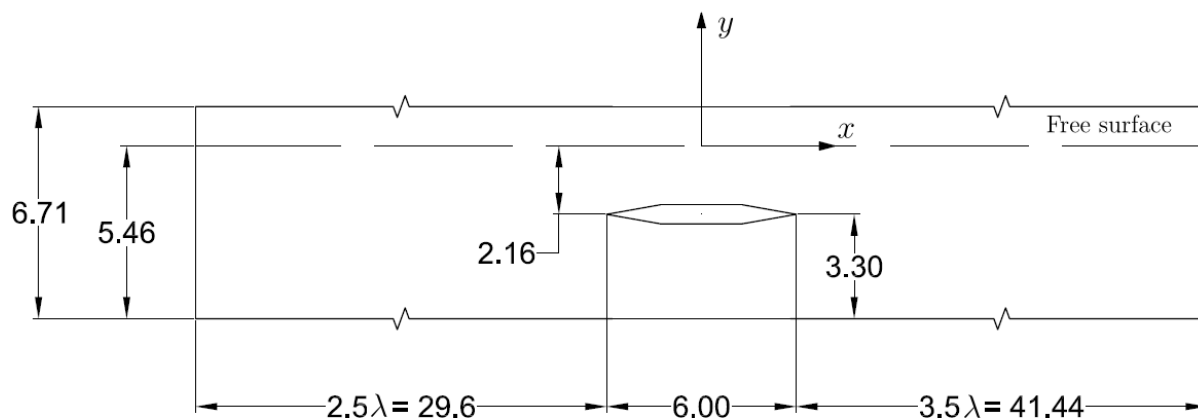
Red momenta		1. Red	2. Red	3. Red	4. Red
Simulacija 10	$Re(L_{p_z})$	0	0	0	0
	$Im(L_{p_z})$	1	0	0	0
Simulacija 11	$Re(L_{p_z})$	1	0	0	0
	$Im(L_{p_z})$	0	0	0	0
Simulacija 12	$Re(L_{p_z})$	0	0	0	0
	$Im(L_{p_z})$	-800	0	0	0
Simulacija 13	$Re(L_{p_z})$	800	0	0	0
	$Im(L_{p_z})$	0	0	0	0
Simulacija 14	$Re(L_{p_z})$	-400	0	0	0
	$Im(L_{p_z})$	700	0	0	0
Simulacija 15	$Re(L_{p_z})$	0	0	0	0
	$Im(L_{p_z})$	600	600	0	0
Simulacija 16	$Re(L_{p_z})$	1200	1800	0	0
	$Im(L_{p_z})$	0	0	0	0
Simulacija 17	$Re(L_{p_z})$	0	800	0	0
	$Im(L_{p_z})$	-300	0	0	0
Simulacija 18	$Re(L_{p_z})$	200	0	0	-600
	$Im(L_{p_z})$	0	700	-900	0

Tablica 4: Rezultati simulacija za validaciju rotacijskog rješenja.

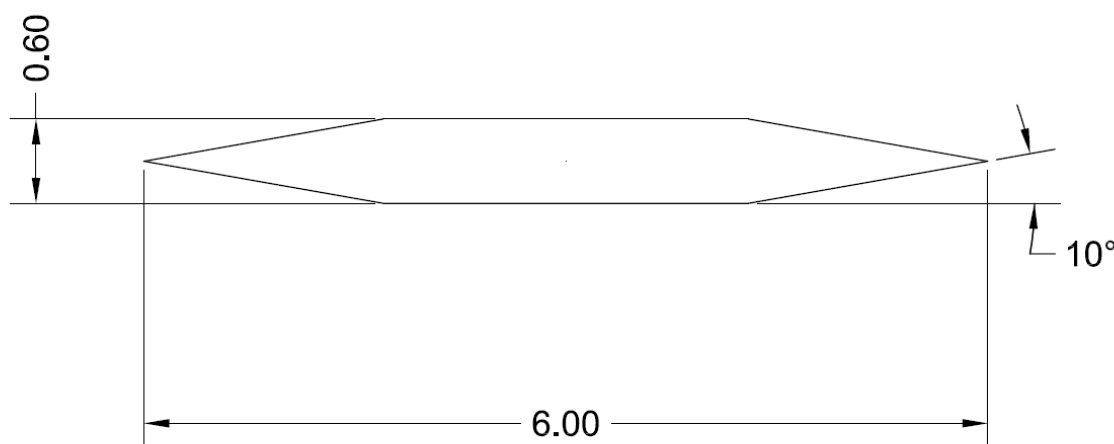
Red, $p$			1. Red	2. Red	3. Red	4. Red
Simulacija 10	$ \Theta_{p_z} $ , rad	numeričko	0.00012411	0	0	0
		analitičko	0.00012411	0	0	0
	$ \Omega_{p_z} $ , rad/s	numeričko	0.00111408	0	0	0
		analitičko	0.00111408	0	0	0
Simulacija 11	$ \Theta_{p_z} $ , rad	numeričko	0.00012411	0	0	0
		analitičko	0.00012411	0	0	0
	$ \Omega_{p_z} $ , rad/s	numeričko	0.00111408	0	0	0
		analitičko	0.00111408	0	0	0
Simulacija 12	$ \Theta_{p_z} $ , rad	numeričko	0.099294	0	0	0
		analitičko	0.099294	0	0	0
	$ \Omega_{p_z} $ , rad/s	numeričko	0.89126	0	0	0
		analitičko	0.89126	0	0	0
Simulacija 13	$ \Theta_{p_z} $ , rad	numeričko	0.099294	0	0	0
		analitičko	0.099294	0	0	0
	$ \Omega_{p_z} $ , rad/s	numeričko	0.89126	0	0	0
		analitičko	0.89126	0	0	0
Simulacija 14	$ \Theta_{p_z} $ , rad	numeričko	0.10006	0	0	0
		analitičko	0.10006	0	0	0
	$ \Omega_{p_z} $ , rad/s	numeričko	0.89820	0	0	0
		analitičko	0.89820	0	0	0
Simulacija 15	$ \Theta_{p_z} $ , rad	numeričko	0.074471	0.018617	0	0
		analitičko	0.074471	0.018617	0	0
	$ \Omega_{p_z} $ , rad/s	numeričko	0.66845	0.33422	0	0
		analitičko	0.66845	0.33422	0	0
Simulacija 16	$ \Theta_{p_z} $ , rad	numeričko	0.14894	0.055853	0	0
		analitičko	0.14894	0.055853	0	0
	$ \Omega_{p_z} $ , rad/s	numeričko	0.1.33692	1.00267	0	0
		analitičko	1.33690	1.00267	0	0
Simulacija 17	$ \Theta_{p_z} $ , rad	numeričko	0.037235	0.024823	0	0
		analitičko	0.037235	0.024823	0	0
	$ \Omega_{p_z} $ , rad/s	numeričko	0.33422	0.44563	0	0
		analitičko	0.33422	0.44563	0	0
Simulacija 18	$ \Theta_{p_z} $ , rad	numeričko	0.024823	0.021720	0.012411	0.0046544
		analitičko	0.024823	0.021720	0.012411	0.0046544
	$ \Omega_{p_z} $ , rad/s	numeričko	0.22281	0.38992	0.33422	0.16711
		analitičko	0.22281	0.38992	0.33422	0.16711

### Validacija translatornog gibanja uzrokovanog utjecajem valova

U drugom testnom slučaju se rezultati HB simulacije uspoređuju s rezultatima odgovarajuće tranzijentne simulacije. Dimenzije računalne domene korištene u HB simulaciji su prikazane na slici 6, dok se pojedinosti geometrije uronjenog tijela mogu vidjeti na slici 7.



Slika 6: Računalna domena za HB simulaciju.



Slika 7: Dimenzije krutog tijela.

Površinski valovi koji uzrokuju gibanje tijela imaju valnu duljinu od  $\lambda = 11.84$  m. Iz te vrijednosti valne duljine određuje se kružna frekvencija i temeljni period oscilacije. Međutim potrebno je uzeti u obzir i činjenicu da se tijelo giba brzinom od  $U = 2$  m/s. Stoga se u simulacijama koristi tzv. nailazna kružna frekvencija koja u sebi sadrži i utjecaj gibanja tijela. Nailazna kružna frekvencija u ovom slučaju je  $\omega_e = 3.343$  rad/s što odgovara nailaznom periodu  $T_e = 1.8795$  s. Potrebno je još spomenuti da je visina vala  $H = 0.196$  m.

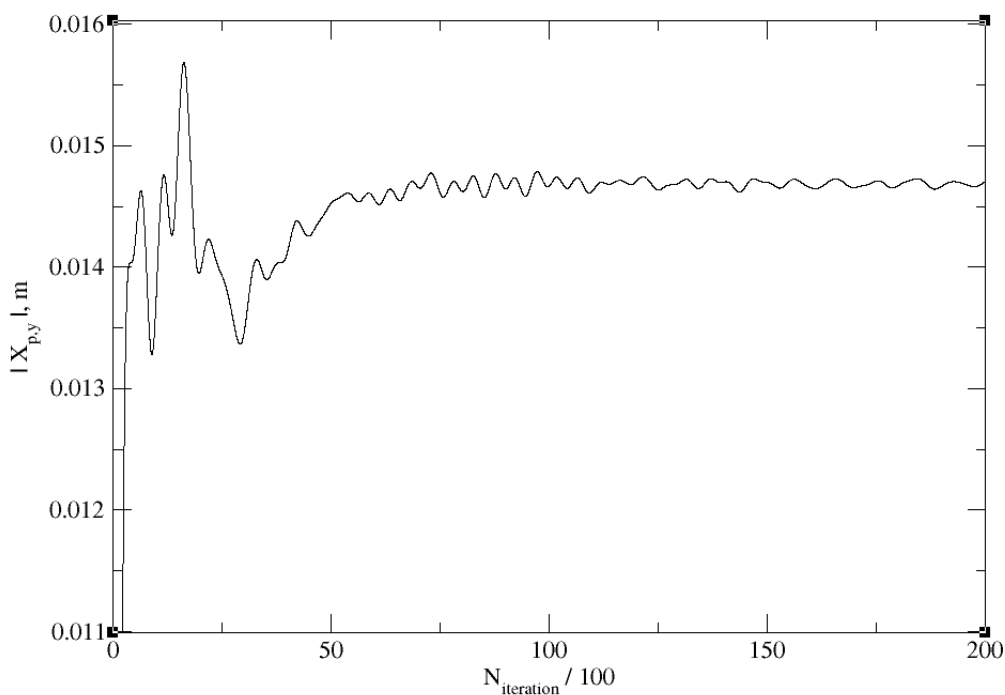
HB simulacija je izvršena s 4 i 6 harmonika. U tablici 5 su prikazani rezultati HB simulacija kao i relativna razlika u odnosu na rezultate tranzijentne simulacije. Relativna razlika se izračunava kao  $\varepsilon = (S_t - S_{hb})/S_t$ , gdje  $S_t$  označava tranzijentno rješenje, a  $S_{hb}$  označava HB rješenje.

**Tablica 5: Prvi i drugi red amplitude pomaka i sile.**

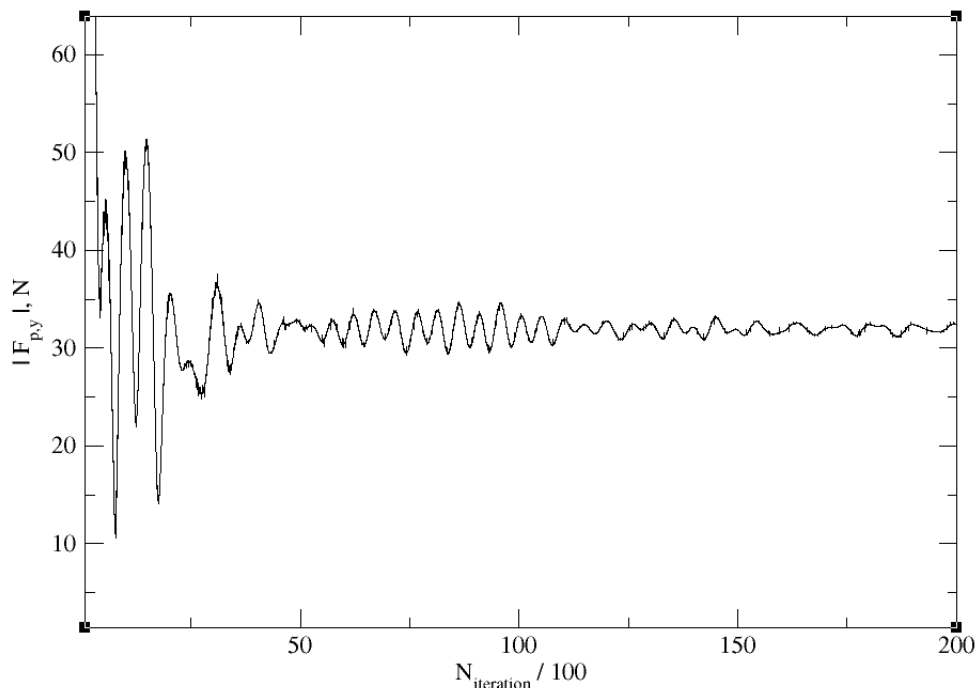
No. Harmonics	$X_1$ [m]	$F_1$ [N]	$F_2$ [N]	$ \varepsilon_{X_1} , \%$	$ \varepsilon_{F_1} , \%$	$ \varepsilon_{F_2} , \%$
4	0.01486	30.8 – 33.2	0.7 – 1.9	13.6	7.57 – 15.96	77.57
6	0.01468	31.2 – 32.4	1 – 1.7	12.23	8.97 – 13.16	58.87

Iz tablice se može iščitati da je relativna razlika za prvi red amplitude pomaka 13.6% za simulaciju sa četiri harmonika, dok ta razlika kod simulacije sa šest harmonika padne na 12.23%.

Sile prvog i drugog reda ne konvergiraju u potpunosti u HB simulaciji tj. zadržava se periodična promjena između minimalne i maksimalne vrijednosti. U simulaciji sa četiri harmonika, najveća relativna razlika za prvi red sile iznosi 15.96%, dok u slučaju simulacije sa šest harmonika ta razlika padne na 13.16%. Rezultati za drugi red sile u obje simulacije imaju odstupanje od  $\pm 50\%$  od iznosa svoje srednje vrijednosti te se stoga ne mogu uzeti u obzir. Međutim, budući da je iznos drugog reda sile maksimalno  $\approx 5\%$  iznosa sile prvog reda, on ne utječe znatno na ukupno gibanje krutog tijela. U tablici 5 prikazani su samo pomaci prvog reda. Konvergencija pomaka prikazana je na slici 8, dok je konvergencija sile prikazana na slici 9.

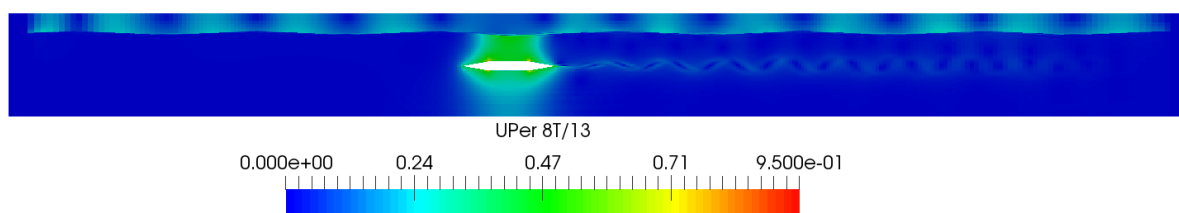


**Slika 8: Konvergencija prvog reda pomaka.**

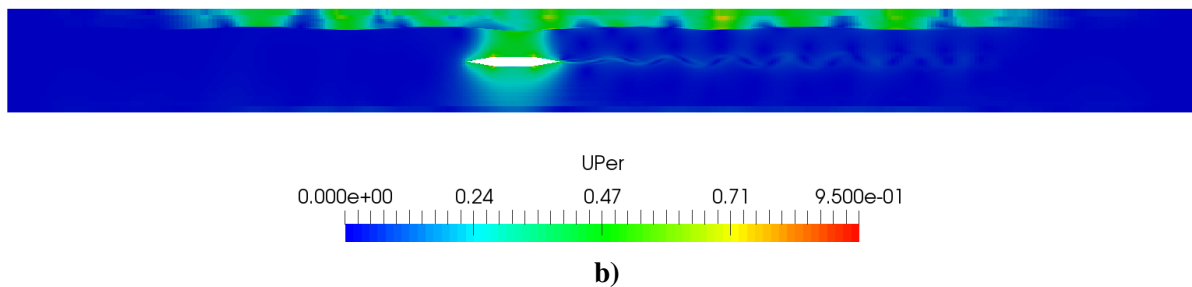


**Slika 9: Konvergencija prvog reda sile.**

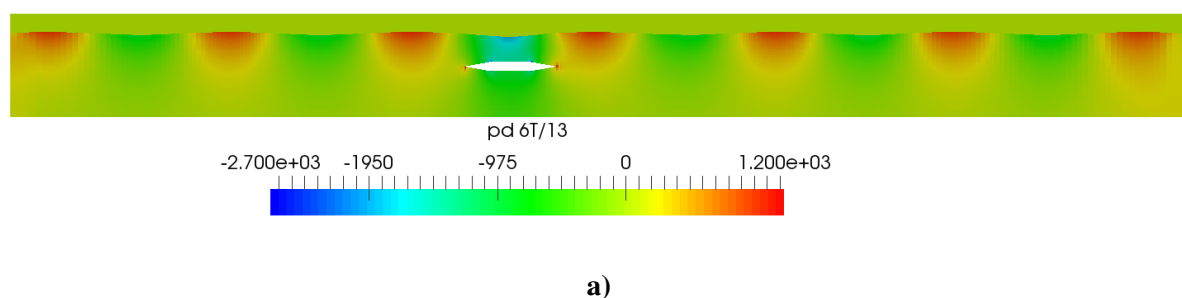
Sa slika koje pokazuju polje perturbirane brzine (slike 10a i 10b) u obje simulacije može se zaključiti da su ona slična u prvoj fazi tj. vodi. Međutim, veličina perturbiranog polja brzine u zraku je veća u tranzijentnoj simulaciji, dok je periodičnost polja bolje izražena u HB simulaciji. Razlika u poljima perturbirane brzine je povezana s postojanjem velikih iznosa tlakova u relaksacijskoj zoni tranzijentne simulacije (slike 11a i 11b). Usprkos tome sa slika 11a i 11b koje prikazuju polje dinamičkog tlaka u obje simulacije za 6 vremenski trenutak se može zaključiti da je polje tlaka slično u okolici potopljenog tijela. Budući da je u ovom slučaju tijelo uronjeno razlike u perturbiranim poljima ne utječu na gibanje.



**a)**



Slika 10: (a) HB simulacija u trenutku  $8T/13$ , (b) Tranzijentna simulacija u trenutku  $8T/13$ .



Slika 11: (a) HB simulacija u trenutku  $6T/13$ , (b) Tranzijentna simulacija u trenutku  $6T/13$ .

## Zaključak

Iz provedene validacije algoritma za izračun gibanja u frekvencijskoj domeni se vidi da je relativna razlika između rezultata HB i tranzijentne simulacije između 10% i 15%. Takve razlike su prihvatljive budući da je gibanje uronjenog tijela ekstremno blago. Vrijednost prvog reda sile iznosi samo 0.32% težine tijela, dok je amplituda gibanja manja od 10% visine površinskog vala.

U budućem radu nužno je validirati rotacijsko gibanje krutog tijela te provesti 3D simulaciju gibanja sa 6 stupnjeva slobode. Rezultati provedenih simulacija potvrđuju da se HB metoda može koristiti sa simulaciju gibanja tijela pri plovidbi po valovitom moru.



# 1 Introduction

This work presents the development and validation of time-spectral method for simulation of the wave-induced rigid body motion. Simulation of nonlinear, viscous, temporally periodic, large-scale two-phase flows is based on an existing two-phase numerical model developed within a Finite Volume (FV) Computational Fluid Dynamics (CFD) software *foam-extend* [1]. This method is intended for general two-phase flows with temporally periodic nature of the boundary conditions. With temporally periodic boundary conditions, flow field in the domain of the interest is periodic. Periodic flow fields are encountered in the problems with surface waves which are important in the field of naval, offshore and ocean hydrodynamics.

One of the important tasks of naval hydrodynamics is to reliably assess the drag force of ships in waves. Reliable assessment of drag force in waves is important in the process of the ship hull optimization which is used to lower fuel consumption. Therefore, for the assessment of drag force viscous CFD methods are used since they offer reliable results, as shown in numerous validation publications [8, 9, 10, 11, 12].

Most viscous naval hydrodynamics CFD calculations are performed in time domain. Although frequency domain methods have been used in naval hydrodynamics over several decades [13], modern spectral CFD method that could be used in naval hydrodynamics was developed in recent years [14, 15, 16, 17, 18, 6]. The mentioned frequency domain methods which were used in naval hydrodynamics are based on the potential flow assumption, where the nonlinear free surface boundary conditions are often linearised. Hence, they cannot describe nonlinear flows accurately and therefore cannot be used to assess ship resistance in waves.

Spectral CFD methods were first developed in the field of turbomachinery. In the following text, a brief overview of the publications related to the use of spectral methods for the turbomachinery applications will be presented. He and Ning [14] presented a nonlinear harmonic method applied to Navier-Stokes equations for simulation of unsteady viscous flow around turbomachinery blades. Maple et al [15] developed an adaptive method where the number of resolved harmonics is varied in the domain depending on the required spectral resolution, applied to a supersonic/subsonic diverging nozzle. McMullen and Jameson [16] investigated acceleration techniques for coupled sets of steady state equations. Ekici et al [17] used spectral method based Euler equations to simulate helicopter rotor blade flow, while Guédéney et al [18] extended the method for turbomachinery flows with multiple frequencies in order to capture rotor-stator interaction effects.

The nonlinear harmonic method, also called HB, transforms a periodic transient problem into a set of coupled steady-state problems. Transformation of a transient problem into a set of coupled steady-state problems is possible for the flows with temporally periodic nature with a known dominant frequency. Since steady state simulations are generally faster to perform than transient problems, HB method should accelerate the calculation. Furthermore, with the use of



the HB method, the main drawback of the transient simulation of the periodic flow is avoided. When the periodic flow is simulated with transient time-marching techniques a large number of simulated periods is required before fully developed periodical flow can be reached. In this work, implicit coupling of steady state equations in the block matrix is used [5].

Simulation of the flow presents only a part of this work. The flow field obtained with an HB simulation is then used to calculate the corresponding ship motion. Ship motion is governed by the Newton-Euler equations. The Newton-Euler equations are usually solved in time domain. However since the flow field is solved in the frequency domain, the motion equations should be also solved in the frequency domain. Transformation of the Newton-Euler equations in the frequency domain is achieved using the Discrete Fourier Transform (DFT). Definition of the rotation matrix is usually problematic since the most widely used parametrisations (Euler angles, quaternions) have some restrictions. In this thesis, parametrisation problems are avoided by calculating the rotation matrix directly via the Lie group approach [7].

This thesis is divided into five chapters. The second chapter presents the governing equations in SWENSE decomposed form as described by Vukčević et al [3]. Next, the HB treatment of time derivative term is described. Furthermore, von Neumann stability analysis of the implicitly coupled HB source term is conducted. The third chapter is used to describe rigid body motion equations. The chapter is divided into three sections: the first section describes translational motion in both time and the frequency domain, while the second section is used to describe rotational motion in both domains. In the third section, calculation of forces and torques is described. In the fourth chapter, translational and rotational motion is validated with the analytical solution for heave force and pitch torque, respectively. The fifth chapter is used to describe a process of heave translation validation on a submerged rigid body. HB simulation results are compared with the corresponding transient simulation. Finally, a conclusion is given.

## 2 Mathematical model

### 2.1 Introduction

In this chapter a mathematical model used for description of two-phase, nonlinear and viscous flow is given. First, the governing equations will be presented [3] with the usage of Ghost Fluid Method (GFM) [4] to formulate the dynamic pressure and density jump at the interface. Next, the governing equations in SWENSE decomposed form are presented, [3]. Furthermore, a description of governing equations in the time-spectral HB form is given [5].

### 2.2 Governing equations

In this section the mathematical model for incompressible, turbulent, two-phase flow of two immiscible fluids with a sharp interface is presented. Interface  $\Gamma$  separates the two phases, in this thesis water and air, each of which has a constant density,  $\rho = \rho_w$  and  $\rho = \rho_a$ , respectively.

Taking into account piece-wise constant density and continuous velocity field due to the kinematic boundary condition, the continuity equation reads:

$$\nabla \cdot \underline{u} = 0, \quad (2.1)$$

where  $\underline{u}$  is the velocity field. As a general note, in this thesis vectors and vector fields are denoted with one line under the symbol and matrices with two lines.

According to Vukčević et al [4], momentum equation for incompressible, turbulent, two-phase flow reads:

$$\frac{\partial \underline{u}}{\partial t} + \nabla \cdot (\underline{u}\underline{u}) - \nabla \cdot (\underline{v}_e \nabla \underline{u}) = -\frac{1}{\rho} \nabla p_d + \nabla \underline{u} \cdot \nabla \underline{v}_e, \quad (2.2)$$

where  $\underline{v}_e$  stands for the effective kinematic viscosity,  $\rho$  is the density which has a discontinuity at the interface,  $p_d$  denotes the dynamic pressure,  $p_d = p - \rho \underline{g} \cdot \underline{x}$ , where  $p$  is the pressure,  $\underline{g}$  represents constant gravitational acceleration, and  $\underline{x}$  is the radii vector.

The interface is captured with the Level Set (LS) method derived from Phase Field equation. In the Level Set equation derived from Phase Field equation [2], the signed distance function is unbounded, which is suitable for SWENSE decomposition. Additionally, the need for the redistancing algorithm is eliminated [3].

Transport equation for the Level Set field  $\psi$  reads:

$$\frac{\partial \psi}{\partial t} + \nabla \cdot (\underline{c}\psi) - \psi \nabla \cdot \underline{c} - b \nabla \cdot (\nabla \psi) = b \frac{\sqrt{2}}{\varepsilon} \tanh \left( \frac{\psi}{\varepsilon \sqrt{2}} \right). \quad (2.3)$$

In Eq. (2.3)  $b$  and  $\varepsilon$  are numerical parameters:  $b$  is the diffusion coefficient and  $\varepsilon$  is the width parameter.  $\underline{c}$  is the modified convective velocity defined as:

$$\underline{c} = \underline{u} + b \frac{\sqrt{2}}{\varepsilon} \tanh\left(\frac{\psi}{\varepsilon\sqrt{2}}\right) \nabla\psi + b\kappa \frac{\nabla\psi}{|\nabla\psi|}, \quad (2.4)$$

where  $\kappa$  denotes mean interface curvature.

For the mathematical model to be complete, it is necessary to state the appropriate jump conditions at the interface. The GFM [4] used in this model implicitly takes into account the discontinuities in the pressure gradient and density on the free surface by satisfying the kinematic and dynamic free surface boundary conditions [4]. The kinematic free surface boundary condition states that velocity is continuous across the interface, i.e. velocity field infinitesimally close to the interface in the heavier fluid is equal to the velocity field infinitesimally close to the interface in the lighter fluid<sup>2</sup>:

$$[\underline{u}] = \underline{u}^- - \underline{u}^+ = 0. \quad (2.5)$$

The dynamic boundary condition states that the stresses at the interface must be in equilibrium. Stress is usually divided into the normal component due to pressure and the tangential component which originates from viscous stress. In this work, only the pressure gradient jump due to density jump at the interface is taken into account:

$$[\rho] = \rho^- - \rho^+, \quad (2.6)$$

while surface tension effects are neglected. By neglecting the surface tension effects, we obtain the condition of discontinuous pressure field that can be written in terms of dynamic pressure in the following form:

$$[p_d] = -[\rho] \underline{g} \cdot \underline{x}. \quad (2.7)$$

Tangential stress is approximated by linear interpolation of the kinematic viscosity at the interface:

$$\nu_e = \alpha \nu_{e,w} + (1 - \alpha) \nu_{e,a}. \quad (2.8)$$

Linear interpolation is justified for large scale free surface flows [5] considered in this work.

Additional jump condition that needs to be taken into account comes from the continuous velocity field  $\underline{u}$  and assumed continuity of the kinematic viscosity  $\nu_e$ . If we transfer the term  $\nabla \underline{u} \cdot \nabla \nu_e$  from RHS to the LHS of Eq. (2.2) we can see that then LHS is continuous and because of that RHS also must be continuous i.e.:

$$\left[ \frac{1}{\rho} \nabla p_d \right] = 0. \quad (2.9)$$

<sup>2</sup>In all equations related to the GFM <sup>+</sup> denotes heavier fluid and <sup>-</sup> denotes lighter fluid.

Eq. (2.9) represents an additional jump condition that needs to be taken into account along with the conditions stated by Eq. (2.5), Eq. (2.6) i Eq. (2.7). For more details regarding the derivation and implementation of the GFM the reader is referred to [4].

### 2.3 SWENSE decomposition

Spectral Wave Explicit Navier Stokes Equation (SWENSE) decomposition is based on the decomposition of an arbitrary field  $\xi$  into incident  $\xi_I$  and diffracted (perturbation)  $\xi_P$  component [3] :

$$\xi = \xi_I + \xi_P. \quad (2.10)$$

The purpose of SWENSE decomposition is to describe the main features of a free surface wave with a potential flow model from which the field  $\xi_I$  is calculated. After the incident field  $\xi_I$  is obtained, nonlinear, viscous and turbulent effects are superimposed via diffracted field  $\xi_P$ . Although the choice of the incident field  $\xi_I$  is arbitrary, it is assumed that it represents a reasonable estimate of the complete solution.

Governing equations in SWENSE decomposed form are presented in the following text. Note that all incident fields generated by decomposition are denoted with index  $I$ , while all perturbed fields are denoted with index  $P$ .

SWENSE decomposed form of continuity equation (2.1) reads:

$$\nabla \cdot \underline{u}_P = -\nabla \cdot \underline{u}_I. \quad (2.11)$$

Although in the potential flow velocity field is solenoidal,  $\nabla \cdot \underline{u}_I = 0$ , the term  $\nabla \cdot \underline{u}_I = 0$  is retained in Eq. (2.11). With that term Eq. (2.11) solves continuity errors generated by mapping the field  $\underline{u}_I$  generated from the potential flow model to the discretised computational domain [3].

Momentum equation (2.2) in SWENSE decomposed form reads:

$$\begin{aligned} \frac{\partial \underline{u}_P}{\partial t} + \nabla \cdot (\underline{u} \underline{u}_P) - \nabla \cdot (\nu_e \nabla \underline{u}_P) = \\ - \frac{\partial \underline{u}_I}{\partial t} - \nabla \cdot (\underline{u} \underline{u}_I) + \nabla \cdot (\nu_e \nabla \underline{u}_I) - \frac{1}{\rho} \nabla p_d + \nabla \underline{u} \cdot \nabla \nu_e. \end{aligned} \quad (2.12)$$

By comparing Eq. (2.2) and Eq. (2.12), it can be seen that only the velocity field  $\underline{u}$  in the time derivative, convection and diffusion terms is decomposed. Decomposition of the convecting velocity field is unnecessary because it is linearised with explicit volume flux from previous time step, dynamic pressure field is not decomposed because it is treated by GFM [4], and the velocity in the last term on right-hand side is not decomposed since it is treated explicitly.

Level Set equation (2.3) in SWENSE decomposed form reads:

$$\begin{aligned} \frac{\partial \psi_P}{\partial t} + \nabla \cdot (\underline{c} \psi_P) - \psi_P \nabla \cdot \underline{c} - b \nabla \cdot (\nabla \psi_P) = \\ - \frac{\partial \psi_I}{\partial t} - \nabla \cdot (\underline{c} \psi_I) + \psi_I \nabla \cdot \underline{c} + b \nabla \cdot (\nabla \psi_I) + b \frac{\sqrt{2}}{\varepsilon} \tanh \left( \frac{\psi}{\varepsilon \sqrt{2}} \right). \end{aligned} \quad (2.13)$$

Modified convective velocity field  $\underline{c}$  is treated in the same way as the convective velocity field in the momentum equation and therefore it is not decomposed. Furthermore, since the Level Set field  $\psi$  is treated explicitly in the last term on the right-hand side, it is not decomposed.

After the decomposition of governing equations, an overview of the Harmonic Balance method will be given in the next section.

## 2.4 Harmonic balance method

The Harmonic Balance method [6, 5] is used in temporally periodic flows with a known dominant frequency to transform a periodic transient problem into a set of coupled steady-state problems. Transient equations are transformed into a set of steady-state equation coupled via source term that represents the time derivative in the frequency domain. The primary condition that needs to be fulfilled for the usage of Harmonic Balance method is that the flow is temporally periodic in which case every variable can be expanded in a Fourier series with a finite number of harmonics  $N$ :

$$\mathcal{Q}(t) = Q_0 + \sum_{l=1}^N (Q_{C_l} \cos(l\omega t) + Q_{S_l} \sin(l\omega t)), \quad (2.14)$$

where  $\mathcal{Q}$  denotes a general field variable in time, while  $Q$  stands for a Fourier coefficient of that variable in frequency domain.  $\omega$  is a known dominant i.e. base frequency of  $\mathcal{Q}$  and indices  $S_l$  and  $C_l$  stand for the sine and cosine Fourier coefficient, respectively.

Standard transport equation for a variable  $\mathcal{Q}$  in time domain has the following form:

$$\frac{\partial \mathcal{Q}}{\partial t} + \mathcal{R} = 0, \quad (2.15)$$

where  $\mathcal{R}$  is a condensed way of writing convective, diffusive and source terms:

$$\mathcal{R} = \nabla \cdot (\underline{u} \mathcal{Q}) - \nabla \cdot (\gamma \nabla \mathcal{Q}) - S_{\mathcal{Q}}, \quad (2.16)$$

used for the sake of clarity.  $\mathcal{R}$  is expanded into a Fourier series analogous to the Eq. (2.14), with  $Q$  substituted by  $R$ . Insertion of  $\mathcal{Q}$  and  $\mathcal{R}$  into the standard transport equation, Eq. (2.15) yields:



expansion, Eq. (2.14) can be regarded as Discrete Fourier Transform (DFT), matrix representation of DFT is defined to switch between time and frequency domain easily:

$$\underline{Q} = \underline{E} \underline{\mathcal{Q}}. \quad (2.23)$$

$\underline{\mathcal{Q}}$  represents a vector of discrete time values of  $\mathcal{Q}$ . Thus, with the usage of matrix representation DFT, Eq. (2.21) can be written in terms of time domain variable as:

$$\omega \underline{A} \underline{E} + \underline{E} \underline{\mathcal{R}} = \underline{0}. \quad (2.24)$$

Eq. (2.24) is multiplied with  $\underline{E}^{-1}$  from the left which gives us a time-spectral form of that equation:

$$\omega \underline{E}^{-1} \underline{A} \underline{E} + \underline{\mathcal{R}} = \underline{0}. \quad (2.25)$$

Eq. (2.25) presents a set of quasi-steady state equations coupled by off-diagonal elements of the matrix  $\underline{E}^{-1} \underline{A} \underline{E}$ . If we compare Eq. (2.15) and Eq. (2.25), it can be noticed that the time derivative term is replaced by a source term. Label  $\underline{S}(\underline{\mathcal{Q}})$  is defined to represent the HB temporal coupling vector as:

$$\underline{S}(\underline{\mathcal{Q}}) = \omega \underline{E}^{-1} \underline{A} \underline{E} \underline{\mathcal{Q}}, \quad (2.26)$$

while  $S_l$  is  $l$ -th element of the vector defined as:

$$S_l(\underline{\mathcal{Q}}) = -\frac{2\omega}{2N+1} \left( \sum_{k=1}^{2N} P_{k-l} \mathcal{Q}_{t_k} \right), \text{ for } l = 1 \dots 2N+1. \quad (2.27)$$

In Eq. (2.27),  $t_k$  represents the  $k$ -th discrete time instant:

$$t_k = \frac{kT}{2N+1}, \text{ for } k = 1, 2 \dots 2N+1, \quad (2.28)$$

where  $T$  is the base period of oscillation corresponding to  $\omega$ . Furthermore,  $P$  in Eq. (2.27) denotes the constant periodic coupling matrix defined as:

$$P_r = \sum_{m=1}^N r \sin(rm\omega\Delta t), \quad r = -N \dots N, \quad (2.29)$$

where  $\Delta t = T/(2N+1)$ .

From this brief presentation of the Harmonic Balance method (Following [6]), it can be seen that one transient problem is transformed into a set of  $2N+1$  quasi-steady state problems. Each of  $2N+1$  steady state problems describes one equidistantly spaced time instant of period  $T$ . The steady state equations are coupled through the source term, defined by Eq. (2.27), while the discretisation of convection, diffusion and source terms of the transient equation remain

unchanged. In the following text benefits of the implicit coupling of the HB source term will be presented via von Neumann stability analysis. Stability analysis of implicit coupling was conducted by Gatin et al. [5].

### 2.4.1 Implicit coupling of the HB source term

The implicit source coupling between quasi steady-state equations is achieved through a block matrix [19]. The diagonal elements of the block matrix are matrices of size  $(2N + 1) \times (2N + 1)$ , containing the diagonal coefficients of all steady-state equations, and their coupling in off-diagonal coefficients. The solution and source vectors are  $(2N + 1)$  vectors. It is important to say that the block matrix is used only to resolve coupling arising from HB method, while velocity, pressure and surface capturing equations are solved in a segregated manner.

We shall use the von Neumann stability analysis to show benefits of the implicit coupling. The von Neumann stability analysis is conducted on a one-dimensional convection problem in HB form [5]:

$$\frac{\partial \underline{\mathcal{Q}}}{\partial \tau} = -\underline{S}(\underline{\mathcal{Q}}) - \underline{u} \frac{\partial \underline{\mathcal{Q}}}{\partial x}, \quad (2.30)$$

where  $\partial \underline{\mathcal{Q}} / \partial \tau$  presents quasi-temporal term used to facilitate marching towards the steady-state solution, while  $\underline{u}$  denotes the velocity vector field at individual discrete time instants. In order to use the von Neumann stability analysis the source term  $\underline{S}(\underline{\mathcal{Q}})$  of HB method must be formulated in a more general form. Namely, the HB method presented in the text above is formulated with the Fourier series truncated to real part (see Eq. (2.14)), while here a complex Fourier series form is used that produces an imaginary unit in the temporal derivative. Complex Fourier series will be presented in more detail in the next chapter. With the usage of complex Fourier series Eq. (2.30) assumes the following form:

$$\frac{\partial \underline{\mathcal{Q}}}{\partial \tau} = -i\omega \underline{E}^{-1} \underline{A} \underline{E} \underline{\mathcal{Q}} - \underline{u} \frac{\partial \underline{\mathcal{Q}}}{\partial x}, \quad (2.31)$$

where  $i$  stands for imaginary unit,  $i = \sqrt{-1}$ . As stated earlier, each vector in Eq. (2.31) consists of values at the individual time instants; therefore Eq. (2.31) presents a set of coupled equations. However, our goal is to examine individual equation in stability analysis, hence Eq. (2.31) needs to be written in a decoupled manner. Diagonalization of the equation is achieved through the following procedure: first we use the expression  $\underline{\mathcal{Q}} = \underline{E}^{-1} \underline{Q}$  and then multiply equation by  $\underline{E}$  from left. Furthermore, velocity is linearised as  $\underline{u} = \underline{U} \underline{I} + \underline{\delta u}$ , where  $\underline{U}$  represents the mean convective velocity,  $\underline{I}$  is identity vector, and  $\underline{\delta u}$  is the perturbation of velocity. After this procedure Eq. (2.31) assumes the following form:

$$\frac{\partial \underline{Q}}{\partial \tau} = -i\omega \underline{A} \underline{Q} - \underline{U} \frac{\partial \underline{Q}}{\partial x}, \quad (2.32)$$



where  $\underline{Q}$  represents a transformed variable in the frequency domain. Since matrix  $\underline{A}$  defined by Eq. (2.22) is a diagonal matrix, the system of equations described by Eq. (2.32) is decoupled. Hence, we can observe each of  $l$  equations independently:

$$\frac{\partial Q_l}{\partial \tau} = -i\omega l Q_l - U \frac{\partial Q_l}{\partial x}. \quad (2.33)$$

Before the analysis of the implicit approach, explicit coupling approach for the HB source term is examined. In both explicit and implicit approach, implicitly treated convection term is discretised with a first order upwind scheme, while the quasi-temporal term is discretised with a first order accurate Euler scheme. Superscript  $n$  denotes the new time step value, while  $o$  denotes the old time step value.

The discretised form of Eq. (2.33) for explicit coupling of HB source term reads:

$$\frac{Q_{l,p}^n - Q_{l,p}^o}{\Delta \tau} = -i\omega l Q_{l,p}^o - U \frac{Q_{l,p}^n - Q_{l,p-1}^n}{\Delta x}, \quad (2.34)$$

where  $p$  stands for the  $p$ -th grid point i.e cell centre. The von Neumann analysis uses Fourier transform to present the distribution of a variable in space:

$$Q_{l,p} = \sum_{q=-N_c}^{N_c} V_{l,q} e^{ipq\pi/N_c}, \quad p = 1 \dots N_c, \quad (2.35)$$

where  $N_c$  stands for the total number of cells and  $V_{l,q}$  is the vector of  $q$ -th Fourier amplitudes. The system is stable when the magnitude of the amplification factor  $G = V_{l,q}^n / V_{l,q}^o$  is smaller than one for every  $q$ . An arbitrary Fourier coefficient can be used, since the stability condition  $G < 1$  must be valid for each Fourier coefficient:

$$Q_{l,p} = V_l e^{ip\alpha}, \quad (2.36)$$

where  $\alpha$  denotes a general phase angle. Substituting Eq. (2.36) into Eq. (2.34) yields:

$$\frac{V_l^n e^{ip\alpha} - V_l^o e^{ip\alpha}}{\Delta \tau} = -i\omega l V_l^o e^{ip\alpha} - U \frac{V_l^n e^{ip\alpha} - V_l^n e^{i(p-1)\alpha}}{\Delta x}. \quad (2.37)$$

The amplification factor is obtained after simplification of Eq. (2.37):

$$\left| \frac{V_l^n}{V_l^o} \right| = \frac{|1 - i\Delta\tau\omega l|}{\left| 1 + \frac{U\Delta\tau}{\Delta x} (1 - e^{-i\alpha}) \right|}. \quad (2.38)$$

Eq. (2.38) can be written in a more suitable form after introduction of Courant-Friedrich-Lewy number  $Co = U\Delta\tau/\Delta x$  [20]:

$$\left| \frac{V_l^n}{V_l^o} \right| = \frac{|1 - iCo \frac{\Delta x \omega l}{U}|}{\left| 1 + Co (1 - e^{-i\alpha}) \right|}. \quad (2.39)$$

Eq. (2.39) tells us that solution is conditionally stable. By observing the numerator, it can

be seen that solution stability decreases with higher base frequency, coarser grid (larger  $\Delta x$ ) and smaller convective velocity. Deterioration of stability for larger number of harmonics can limit the spectral resolution of the simulation, and convective velocity poses a limit for practical applications since the mean velocity cannot be small or zero.

The discretised form of Eq. (2.33) for implicit coupling of the HB source term is:

$$\frac{Q_{l,p}^n - Q_{l,p}^o}{\Delta \tau} = -i\omega l Q_{l,p}^n - U \frac{Q_{l,p}^n - Q_{l,p-1}^n}{\Delta x}, \quad (2.40)$$

from which, by analogy with Eq. (2.37), Eq. (2.38) and Eq. (2.39) follows:

$$\left| \frac{V_l^n}{V_l^o} \right| = \frac{|1|}{\left| 1 + iCo \frac{\Delta x \omega l}{U} + Co(1 - e^{-i\alpha}) \right|}. \quad (2.41)$$

Eq. (2.41) tells us that the solution that arises from implicit HB source term coupling is unconditionally stable. Contrary to the explicit coupling, stability of the implicit coupling solution increases with a coarser spatial grid, higher base frequency, smaller convective velocity and a larger number of harmonics. In conclusion, it can be said that implicit coupling enables stable simulations with low computational demands, and it enables simulating flows with low mean velocity. It should be noted that this analysis was conducted on linearised equation set, where convective velocity remains constant from time-step to time-step. For more details regarding the derivation and implementation of implicit coupling of the HB source term the reader is referred to [5].

## 2.5 Governing equations in the HB form

Having presented the basics of the HB method, in the previous section, in this section the governing equations of the flow (see Eq. (2.11), Eq. (2.12) and Eq. (2.13) ) will be presented in the HB form. It was shown that only the terms with rate-of-change are replaced with HB source terms, while other terms remain unchanged.

The continuity equation (2.11) does not have any rate-of-change terms. Therefore the form of the equation remains unchanged:

$$\nabla \cdot \underline{u}_{P,l} = -\nabla \cdot \underline{u}_{I,l}, \quad l = 1 \dots 2N + 1. \quad (2.42)$$

The only difference between Eq. (2.42) and Eq. (2.11) is that in Eq. (2.42) velocity field is defined in equidistantly spaced time instants, thus giving us  $2N + 1$  mutually independent equations.

The SWENSE momentum equation (2.12) has two time-derivative terms that need to be replaced with HB source terms:

$$\begin{aligned}
S_l(\underline{u}_P) + \nabla \cdot (\underline{u}_l \underline{u}_{P_l}) - \nabla \cdot (\mathbf{v}_{e_l} \nabla \underline{u}_{P_l}) = \\
- S_l(\underline{u}_I) - \nabla \cdot (\underline{u}_l \underline{u}_{I_l}) + \nabla \cdot (\mathbf{v}_{e_l} \nabla \underline{u}_{I_l}) - \frac{1}{\rho_l} \nabla p_{d_l} + \nabla \underline{u}_l \cdot \nabla \mathbf{v}_{e_l}, \quad l = 1 \dots 2N + 1.
\end{aligned} \tag{2.43}$$

Note that each of  $2N + 1$  quasi-steady-state equations has corresponding density  $\rho_l$  and effective kinematic viscosity  $\mathbf{v}_{e_l}$  fields. Since two HB source terms in Eq. (2.43) represent linear operators, they could be rewritten as one term but this is not done in order to allow different treatment of source terms for the perturbation velocity field  $\underline{u}_P$  and the incident velocity field  $\underline{u}_I$ . The source term of the perturbation velocity field  $\underline{u}_P$  is treated implicitly, while the source term for the incident field  $\underline{u}_I$  is treated explicitly.

Similar to the momentum equation, Level Set equation (2.13) has two time-derivative terms, therefore transformation of Level Set equation is similar to the transformation of the momentum equation:

$$\begin{aligned}
S_l(\psi_P) + \nabla \cdot (\underline{c}_l \psi_{P_l}) - \psi_{P_l} \nabla \cdot \underline{c}_l - b \nabla \cdot (\nabla \psi_{P_l}) = \\
- S_l(\psi_I) - \nabla \cdot (\underline{c}_l \psi_{I_l}) + \psi_{I_l} \nabla \cdot \underline{c}_l + b \nabla \cdot (\nabla \psi_{I_l}) + b \frac{\sqrt{2}}{\varepsilon} \tanh \left( \frac{\psi_{I_l}}{\varepsilon \sqrt{2}} \right).
\end{aligned} \tag{2.44}$$

Again, similar to Eq. (2.43), the HB source term is separated for the incident and perturbation parts of the solution to enable implicit treatment of the perturbation source coupling.

## 2.6 Closure

This chapter shows the mathematical model used to simulate two-phase, nonlinear and viscous flow in the frequency domain following [9, 4, 6, 5]. With the HB method a transient problem is transformed into a set of steady-state problems. Furthermore, it is shown that implicit coupling of the HB source term yields theoretically unconditionally stable solution. In practice it is shown by Gatin et al [5] that the solution is stable only for some minimum value of the reduced frequency. The reader is referred to [5] for details.

Since this chapter presented the governing equation for fluid flow, the next chapter will be dedicated to rigid body dynamics.

## 3 Rigid body dynamics

### 3.1 Introduction

The motion of a rigid body is determined if its configuration, i.e. position and orientation is known at every time instant. Therefore this chapter is divided into two sections: first, governing equation for determination of the rigid body position will be discussed and then governing equation for determination of the rigid body orientation. The differential equation that governs translation (change of position) of a rigid body is called Newton equation, while the differential equation that governs rotation (change of orientation) is called Euler equation.

It is known that it is much easier to describe a translational motion than the rotational motion. Reason for that is that the translations are defined in a linear three-dimensional Euclidean space  $\mathbb{R}^3$ , while rotations are defined in a curved space of group  $SO(3)$ .

### 3.2 Determination of the rigid body position

During translation (change of position) of a rigid body, angles between the basis vectors of inertial and body-fixed coordinate system remain unchanged. Since a rigid body is defined as a sum of an infinite number of mutually constrained particles and because angles between inertial and body-fixed system are constant, translation of a whole body can be described by translation of any point on the rigid body. The basic thesis of continuum mechanics states that one particle takes up only one point in space and that in one point in space can be only one particle. Hence, terms particle and point are used interchangeably in this work. Although any point on a body can be selected to track translation of a body, usually the centre of mass is selected. Also origin of a body-fixed reference frame must be placed in centre of mass so that Newton and Euler equation would be decoupled.

The path that body follows during translation is best described with a position vector  $\underline{x} \in \mathbb{R}^3$ . Vector  $\underline{x}$  connects origin of an inertial coordinate system to the origin of the body-fixed coordinate system i.e. centre of mass of a rigid body. As stated before, a general equation that governs translational motion is the Newton equation:

$$m\ddot{\underline{x}} = \underline{f}_R, \quad (3.1)$$

where  $m$  denotes body mass,  $\ddot{\underline{x}}$  is acceleration of centre of mass, while  $\underline{f}_R$  stands for resultant force acting in the centre of mass of the body.

If we want to model a linear spring-damper system acting on the body, Eq. (3.1) must be modified. From the resultant force  $\underline{f}_R$ , force in the spring is extracted:

$$\underline{f}_s = \underline{c}\underline{x}, \quad (3.2)$$

as well as the force of viscous damping:

$$\underline{f}_d = \underline{k}\dot{\underline{x}}. \quad (3.3)$$

In Eq. (3.2),  $\underline{c}$  stands for a diagonal stiffness matrix of the following form:

$$\underline{c} = \begin{bmatrix} c_x & 0 & 0 \\ 0 & c_y & 0 \\ 0 & 0 & c_z \end{bmatrix}, \quad (3.4)$$

where  $c_x, c_y$  and  $c_z$  are stiffness coefficients of linear spring in the direction of  $x, y$  and  $z$  axis respectively, while  $\underline{x}$  is a position vector. Analogous in Eq. (3.3),  $\underline{k}$  stands for diagonal damping matrix of the following form:

$$\underline{k} = \begin{bmatrix} k_x & 0 & 0 \\ 0 & k_y & 0 \\ 0 & 0 & k_z \end{bmatrix}, \quad (3.5)$$

where  $k_x, k_y$  and  $k_z$  are damping coefficients of viscous damper in the direction of  $x, y$  and  $z$  axis respectively, while  $\dot{\underline{x}}$  is a relative velocity vector.

Note that equations (3.2) and (3.3) are giving only the magnitude of linear spring force and viscous damper force, while the direction is always opposite to the direction of position and relative velocity vectors, respectively. If we take into account the direction of spring and damper forces, Eq. (3.1) take the following form:

$$\underline{m}\ddot{\underline{x}} + \underline{k}\dot{\underline{x}} + \underline{c}\underline{x} = \underline{f}, \quad (3.6)$$

where  $\underline{m}$  stand for the diagonal mass matrix:

$$\underline{m} = \begin{bmatrix} m & 0 & 0 \\ 0 & m & 0 \\ 0 & 0 & m \end{bmatrix}. \quad (3.7)$$

Notation of mass in a form of the mass matrix is used to be consistent with notations of stiffness and damping matrix.

### 3.2.1 Determination of the body position in the frequency domain

In order to solve translational motion in the frequency domain, all time-domain variables from Eq. (3.6) must be expanded into Fourier series. Following the von Neumann stability analysis, complete complex Fourier series is used. General variable  $\mathcal{Q}(t)$  expanded into the Fourier series with  $N$  harmonics takes the following form:

$$\mathcal{Q}(t) = Q_0 + \sum_{p=1}^N Q_p e^{ip\omega t}, \quad (3.8)$$

where  $i$  stands for imaginary unit,  $i = \sqrt{-1}$ ,  $Q_p$  denotes complex Fourier amplitude of  $p$ -th harmonic, while  $\omega$  denotes base angular frequency. Since Eq. (3.6) has terms with both first and second derivative it is necessary to differentiate Fourier series of general variable (Eq. (3.8)). The first derivative of Eq. (3.8) takes the following form::

$$\dot{\mathcal{Q}}(t) = \sum_{p=1}^N ip\omega Q_p e^{ip\omega t}, \quad (3.9)$$

while the second derivative takes form:

$$\ddot{\mathcal{Q}}(t) = \sum_{p=1}^N -p^2 \omega^2 Q_p e^{ip\omega t}. \quad (3.10)$$

Insertion of the Fourier series of the position vector  $\underline{x}$  and his derivatives into Eq. (3.6) yields the governing equation for translation motion in the frequency domain:

$$\begin{aligned} \underline{\underline{m}} \sum_{p=1}^N -p^2 \omega^2 \underline{X}_p e^{ip\omega t} + \underline{\underline{k}} \sum_{p=1}^N ip\omega \underline{X}_p e^{ip\omega t} + \underline{\underline{c}} \sum_{p=1}^N \underline{X}_p e^{ip\omega t} \\ + \underline{\underline{c}} \underline{X}_0 = \underline{F}_0 + \sum_{p=1}^N \underline{F}_p e^{ip\omega t}, \end{aligned} \quad (3.11)$$

where  $\underline{X}_p$  stands for  $p$ th complex Fourier coefficients of position vector  $\underline{x}$ . For each of  $N$  harmonics exists one vector  $\underline{X}_p$  that contains Fourier coefficients in the direction of  $x, y$  and  $z$  axis.

After equating the terms with the corresponding frequencies in Eq. (3.11), following equation is obtained:

$$\underline{X}_{pj} = \frac{F_{pj}}{-mp^2 \omega^2 + ip\omega k_j + c_j}, \quad p = 1 \dots N \text{ and } j = x, y, z. \quad (3.12)$$

Eq. (3.12) is used to calculate the Fourier coefficients of position with the respect to the inertial coordinate system, i.e. with respect to the direction of  $x, y$  and  $z$  axes of inertial coordinate system.

The velocity is defined as the rate-of-change of position vector:

$$\underline{u} = \frac{d\underline{x}}{dt} = \dot{\underline{x}}. \quad (3.13)$$

If Eq. (3.8) and Eq. (3.9) are used to transform time domain variables  $\underline{u}$  and  $\underline{x}$  into frequency domain, Eq. (3.13) takes the following form:

$$\underline{U}_0 + \sum_{p=1}^N \underline{U}_p e^{ip\omega t} = \sum_{p=1}^N ip\omega \underline{X}_p e^{ip\omega t}. \quad (3.14)$$

After equating the terms with the same harmonic in Eq. (3.14), the velocity Fourier coefficients can be calculated from position Fourier coefficients with the following equation:

$$\underline{U}_p = ip\omega \underline{X}_p \quad p = 1 \dots N, \quad (3.15)$$

where  $\underline{U}_p$  stands for  $p$ th complex Fourier coefficients of velocity vector  $\underline{u}$ . Similar to the Fourier coefficient position vector, Fourier coefficient velocity vector contains Fourier coefficients of velocity with respect to the inertial coordinate system.

### 3.3 Determination of a rigid body orientation

Orientation of a body is always defined with respect to the inertial coordinate system, while the rotation (change of orientation) is change of angles between basis vectors of inertial and body-fixed coordinate systems. In the previous section it was stated that in order to have decoupled Newton and Euler equations, origin of the body-fixed coordinate system must be in the centre of mass of the rigid body. Also, in order to have a diagonal tensor of inertia, a direction of a body-fixed coordinate system must be aligned with the direction of the principal axes of inertia of a rigid body. Principal axes of inertia can be found for every rigid body, and they can be easily found in symmetrical bodies because every axis perpendicular to the symmetry plane is the principal axis. If a body is three-times symmetrical, all principal axes are defined, but for the two-times and one-time symmetrical bodies only two principal axes or one principal axis is defined beforehand, respectively, while the others must be determined through computation.

The main difference between translations and rotations is the space in which they are defined in. As it was stated before translations are described with the position vector  $\underline{x}$  which is the part of Euclidean space. Euclidean space is linear in its nature. Rotations are unambiguously defined with the rotation matrix  $\underline{R}$  which is the part of special orthogonal group  $SO(3)$ .  $SO(3)$  group is defined in curved space [7].

A rotation matrix  $\underline{R}$  in 3D space is given by a  $3 \times 3$  matrix. Hence,  $\underline{R}$  has 9 elements. However, these elements are not all independent. Therefore, different parametrisations of the rotation matrix are used in dynamics. One of such parametrisation is the Euler angles. The problem with Euler angles is that they are a parametrisation of rotation matrix in a certain domain; thus they cannot describe all rotations. This problem is known as the gimbal lock. Another widely used parametrisation is quaternion-based parametrisation. Quaternions are a single example of a more general class of hypercomplex numbers discovered by Hamilton [21]. Quaternions parametrise rotation matrix with 4 parameters, and they parametrise the whole domain of rotation matrix. Hence, they are more suitable for use than Euler angles.

However, trend in multibody dynamics in recent years is to utilize the fact that rigid body motions form a Lie group. In the following text only brief presentation about derivation of rotation matrix from Lie group approach is given. More detailed presentation exceeds the extent of this thesis. Therefore, reader can find detailed derivation of Geometric methods and formulations in computational multibody system dynamics in the paper by Müller et al. [7].

Configuration of a rigid body is represented by a rotation matrix  $\underline{\underline{R}} \in SO(3)$  and a position vector  $\underline{x} \in \mathbb{R}^3$  and it can be denoted by  $C = (\underline{\underline{R}}, \underline{x}) \in SE(3)$ . The Lie group  $SE(3)$  is a semidirect product of the rotation group  $SO(3)$  and the translation group  $\mathbb{R}^3$ :

$$SE(3) = \{C = (\underline{\underline{R}}, \underline{x}) \mid \underline{\underline{R}} \in SO(3), \underline{x} \in \mathbb{R}^3\}. \quad (3.16)$$

Rotation group  $SO(3)$  acts on the translation group  $\mathbb{R}^3$  and that describes coordinate system transformations. The rotation group, i.e. special orthogonal group  $SO(3)$  that unambiguously describes rotations, is the Lie group [22] defined as:

$$SO(3) = \{\underline{\underline{R}} \in \mathbb{R}^{3 \times 3} \ ; \ \underline{\underline{R}}^{-1} = \underline{\underline{R}}^T, \det \underline{\underline{R}} = 1\}. \quad (3.17)$$

The frame transformations are often represented in the form of homogenous transformation matrices:

$$\underline{\underline{C}} = \begin{bmatrix} \underline{\underline{R}} & \underline{x} \\ \underline{0} & 1 \end{bmatrix} \in SE(3), \quad (3.18)$$

where  $SE(3)$  is matrix Lie group [7].

In the paper by Müller et al. [7] it is shown that configuration  $\underline{\underline{C}}$  is equal to the closed form of the exponential mapping on  $SE(3)$  which can be found by evaluating the matrix exponential:

$$\exp(\hat{\underline{\underline{X}}}) = \begin{bmatrix} \exp\left(\frac{\underline{\underline{\xi}}}{\|\underline{\underline{\xi}}\|}\right) & \frac{dexp_{\underline{\underline{\xi}}}\eta}{1} \\ \underline{0} & 1 \end{bmatrix}, \quad (3.19)$$

with the Euler-Rodrigues formula:

$$\exp\left(\frac{\underline{\underline{\xi}}}{\|\underline{\underline{\xi}}\|}\right) = \underline{\underline{I}} + \frac{\sin\|\underline{\underline{\xi}}\|}{\|\underline{\underline{\xi}}\|}\frac{\underline{\underline{\xi}}}{\|\underline{\underline{\xi}}\|} + \frac{1 - \cos\|\underline{\underline{\xi}}\|}{\|\underline{\underline{\xi}}\|^2}\underline{\underline{\xi}}^2, \quad (3.20)$$

and the right-trivialized differential of the exponential mapping on  $SO(3)$ , i.e.  $dexp_{\underline{\underline{\xi}}}$ .

Since the configuration  $\underline{\underline{C}}$  Eq. (3.18) is equal to the exponential mapping  $\exp(\hat{\underline{\underline{X}}})$ , Eq. (3.19), it can be concluded by comparing these two equations that the rotation matrix can be evaluated as:



$$\underline{\underline{R}} = \underline{\underline{I}} + \frac{\sin \|\underline{\underline{\xi}}\|}{\|\underline{\underline{\xi}}\|} \underline{\underline{\xi}} + \frac{1 - \cos \|\underline{\underline{\xi}}\|}{\|\underline{\underline{\xi}}\|^2} \underline{\underline{\xi}}^2. \quad (3.21)$$

In Eq. (3.21)  $\underline{\underline{I}}$  stands for identity matrix of size  $3 \times 3$ , while  $\underline{\underline{\xi}}$  is a variable calculated from angular velocity  $\underline{\underline{\omega}}$ :

$$\underline{\underline{\xi}} = \underline{\underline{\omega}}. \quad (3.22)$$

Eq. (3.22) ensures second order of accuracy in the numerical procedure. The explanation about other variables in Eq. (3.19) can be found in [7].

Angular velocity  $\underline{\underline{\omega}}$  used in Eq. (3.22) is evaluated from the Euler equation. The Euler equation is the governing equation for the rotation of a rigid body:

$$\underline{\underline{J}} \dot{\underline{\underline{\omega}}} + \underline{\underline{\omega}} \times \underline{\underline{J}} \underline{\underline{\omega}} = \underline{\underline{l}}, \quad (3.23)$$

where  $\underline{\underline{J}}$  denotes the tensor of inertia, while  $\underline{\underline{\omega}}$  stands for the angular velocity and  $\underline{\underline{l}}$  stands for the resultant torque acting on a body. Note that  $\underline{\underline{\omega}}$  used in the Euler equation is different from  $\omega$  used in Fourier series. The former is vector quantity that stands for angular velocity, while the latter is a scalar quantity that denotes the base frequency of oscillation. If a direction of a body-fixed coordinate system is aligned with the direction of the principal axes of inertia of a rigid body, the tensor of inertia becomes diagonal:

$$\underline{\underline{J}} = \begin{bmatrix} J_{xx} & 0 & 0 \\ 0 & J_{yy} & 0 \\ 0 & 0 & J_{zz} \end{bmatrix}, \quad (3.24)$$

where  $J_{xx}, J_{yy}$  and  $J_{zz}$  are principal moments of inertia.

The cross product in the Euler equation (Eq. (3.23)) is not suitable for numerical use. Hence, the cross product should be written as matrix multiplication with the skew-symmetrical matrix:

$$\underline{\underline{\tilde{\omega}}} = \begin{bmatrix} 0 & -\omega_z & \omega_y \\ \omega_z & 0 & -\omega_x \\ -\omega_y & \omega_x & 0 \end{bmatrix}. \quad (3.25)$$

After the cross product is written as a matrix multiplication Euler equation takes the following form:

$$\underline{\underline{J}} \dot{\underline{\underline{\omega}}} + \underline{\underline{\tilde{\omega}}} \underline{\underline{J}} \underline{\underline{\omega}} = \underline{\underline{l}}. \quad (3.26)$$

Although, the rotation matrix  $\underline{\underline{R}}$  is used to rotate a rigid body, a more intuitive way to

express orientation of a body in space is needed. For that purpose Euler angles are used. It has been stated that the use of Euler angles is not suitable for describing rotations, but that is related to the use of Euler angles for the formation of rotation matrix  $\underline{\underline{R}}$ . Angular velocity  $\underline{\omega}$  can be represented through derivation of angle  $\theta$ , but because rotations are part of curved space it cannot be simply stated that angular velocity is equal to the derivation of angle i.e.  $\underline{\omega} \neq \dot{\theta}$ . A relation between body's angular velocity and time derivatives of Euler angles can be given in the form  $\underline{\omega} = \underline{\underline{H}}_R \dot{\underline{x}}_R$ , where  $\underline{x}_R$  represents a vector of Euler angles [23]. If this representation of angular velocity via derivation of angles is inserted in the Euler equation (Eq. (3.26)), its solution will give us angles and not angular velocity. Those angles are then used to form rotation matrix  $\underline{\underline{R}}$ . The rotation matrix can take several different forms based on selected sequence of rotations. Here, the following sequence of rotations is used:  $\theta_x$  about  $x$ -axis, then  $\theta_y$  about the  $y$ -axis, then  $\theta_z$  about the  $z$ -axis, each rotation being applied about one of the axes of global coordinate system as opposed to one of axes of the body-fixed coordinate system [24]:

$$\underline{\underline{R}} = \begin{bmatrix} \cos \theta_y \cos \theta_z & \cos \theta_y \sin \theta_z & -\sin \theta_y \\ \sin \theta_x \sin \theta_y \cos \theta_z - \cos \theta_x \sin \theta_z & \sin \theta_x \sin \theta_y \sin \theta_z + \cos \theta_x \cos \theta_z & \sin \theta_x \cos \theta_y \\ \cos \theta_x \sin \theta_y \cos \theta_z + \sin \theta_x \sin \theta_z & \cos \theta_x \sin \theta_y \sin \theta_z - \sin \theta_x \cos \theta_z & \cos \theta_x \cos \theta_y \end{bmatrix}. \quad (3.27)$$

Since in this work the rotation matrix is calculated using Eq. (3.21), Eq. (3.27) is used to determine the Euler angles  $\theta_x$ ,  $\theta_y$  and  $\theta_z$ . Hence the Euler angles are equal to:

$$\begin{aligned} \theta_x &= \arctan \frac{R_{\underline{\underline{y}}z}}{R_{\underline{\underline{z}}z}}, \\ \theta_y &= \arctan \frac{-R_{\underline{\underline{x}}z}}{c_2}, \\ \theta_z &= \arctan \frac{\sin \theta_x R_{\underline{\underline{z}}x} - \cos \theta_x R_{\underline{\underline{y}}x}}{\cos \theta_x R_{\underline{\underline{y}}y} - \sin \theta_x R_{\underline{\underline{z}}y}}, \end{aligned} \quad (3.28)$$

where  $c_2 = \sqrt{R_{\underline{\underline{x}}x}^2 + R_{\underline{\underline{x}}y}^2}$ .

### 3.3.1 Determination of the body orientation in the frequency domain

The goal of transforming the Euler equation into the frequency domain is to obtain the expression for the Fourier coefficients of angular velocity. The Euler equation (3.26) must be written in the more suitable form before Fourier series expansion is used. First, the second term on the left-hand side of Eq. (3.26) is transferred to the right-hand side, and then the whole equation is multiplied with  $\underline{\underline{J}}^{-1}$ :

$$\underline{\dot{\omega}} = \underline{J}^{-1} \left[ \underline{l} + \left( \widetilde{\underline{J}\omega} \right) \underline{\omega} \right]. \quad (3.29)$$

Note that the vector that forms the skew-symmetrical matrix in transferred term is changed. After all time domain variables are transformed in the frequency domain via Fourier series expansion (Eq. (3.8) and Eq. (3.9)), the Euler equation takes the following form:

$$\sum_{p=1}^N ip\omega \underline{\Omega}_p e^{ip\omega t} = \underline{J}^{-1} \left\{ \underline{L}_0 + \sum_{p=1}^N \underline{L}_p e^{ip\omega t} +^* \left[ \underline{J} \left( \underline{\Omega}_0 + \sum_{p=1}^N \underline{\Omega}_p e^{ip\omega t} \right) \right] \left( \underline{\Omega}_0 + \sum_{p=1}^N \underline{\Omega}_p e^{ip\omega t} \right) \right\}. \quad (3.30)$$

For clarity, skew-symmetrical matrix in Eq. (3.30) is denoted with asterisk \* rather than with tilde ~. Equalizing the terms with the same harmonic and additional simplification yields a piecewise expression for the Fourier coefficients of angular velocity:

$$\begin{aligned} \Omega_{p_x} &= \frac{1}{ip\omega J_{xx}} \left[ L_{p_x} + (J_{yy} - J_{zz}) \sum_{k=0}^p \Omega_{p_y} \Omega_{(p-k)_z} \right], \\ \Omega_{p_y} &= \frac{1}{ip\omega J_{yy}} \left[ L_{p_y} + (J_{zz} - J_{xx}) \sum_{k=0}^p \Omega_{p_z} \Omega_{(p-k)_x} \right], \quad p = 1 \dots N, \quad (3.31) \\ \Omega_{p_z} &= \frac{1}{ip\omega J_{zz}} \left[ L_{p_z} + (J_{xx} - J_{yy}) \sum_{k=0}^p \Omega_{p_x} \Omega_{(p-k)_y} \right], \end{aligned}$$

where  $\Omega_{p_x}, \Omega_{p_y}$  and  $\Omega_{p_z}$  stand for  $p$ th complex Fourier coefficient of angular velocity in the direction of  $x, y$  and  $z$  axis respectively, while analogous to the angular velocity  $L_{p_x}, L_{p_y}$  and  $L_{p_z}$  are  $p$ th complex Fourier coefficients of torque in the direction of  $x, y$  and  $z$  axis.

The rotation matrix (3.21) is evaluated in time domain, but the time domain variable  $\underline{\xi}$  is obtained from its frequency domain counterpart via inverse Fourier transform. The Fourier coefficients of the variable  $\underline{\xi}$  are calculated from Eq. (3.22) transformed into frequency domain:

$$\sum_{p=1}^N ip\omega \underline{\Xi}_p e^{ip\omega t} = \underline{\Omega}_0 + \sum_{p=1}^N \underline{\Omega}_p e^{ip\omega t}, \quad (3.32)$$

where  $\underline{\Xi}_p$  stands for  $p$ th complex Fourier coefficient of variable  $\underline{\xi}$ .

Equalizing the terms of the corresponding harmonics yields the expression for Fourier coefficients of variable  $\underline{\xi}$ :

$$\Xi_{pj} = \frac{\Omega_{pj}}{ip\omega}, \quad \text{for } p = 1 \dots N \text{ and } j = x, y, z. \quad (3.33)$$

### 3.4 Forces acting on a rigid body

The rigid body changes its configuration due to the forces and torques that act on it. Acting force on a body submerged in a fluid can be divided into two parts: part of the force due to pressure  $f_p$  and part of the force due to viscous effects  $f_v$  :

$$\underline{f} = \underline{f}_p + \underline{f}_v. \quad (3.34)$$

Analogous to the force, torque can also be divided into pressure and viscous part:

$$\underline{l} = \underline{l}_p + \underline{l}_v. \quad (3.35)$$

Forces and torques in the time-domain are calculated in the global coordinate system as [3]:

$$\underline{f}_p = \sum_{bf} \underline{s}_f p_f + m \underline{g}, \quad (3.36)$$

$$\underline{f}_v = \sum_{bf} \rho_f \nu_{e,f} \underline{s}_f \cdot \underline{T}^*, \quad (3.37)$$

$$\underline{l}_p = \sum_{bf} \underline{r}_f \times \underline{s}_f p_f, \quad (3.38)$$

$$\underline{f}_v = \sum_{bf} \underline{r}_f \times \left( \rho_f \nu_{e,f} \underline{s}_f \cdot \underline{T}^* \right), \quad (3.39)$$

where  $\sum_{bf}$  denotes summation over all body faces,  $\rho_f$  is the corresponding density at the boundary face and  $\nu_{e,f}$  is effective kinematic viscosity.  $\underline{T}^*$  is deviatoric part of stress tensor  $\underline{T}$ , which is defined as twice symmetric part of the  $\nabla \underline{u}$  tensor. Vector  $\underline{r}_f$  is the distance vector that connects current boundary face and centre of mass of a body.

Since the fluid flow is solved with the HB method, flow field is calculated at  $2N + 1$  equidistantly spaced time instants of period  $T$ . Hence, forces and torques, which are calculated with the pressure field  $p$  and velocity field  $\underline{u}$ , are known only in these discrete time instants. Therefore, forces and torques calculated in time domain must be transformed into the frequency domain via DFT:

$$\begin{aligned}\underline{Q}_0 &= \frac{1}{2N+1} \sum_{j=0}^{2N} \underline{Q}_j, \\ \underline{Q}_p &= \frac{2}{2N+1} \sum_{j=0}^{2N} \underline{Q}_j e^{i\frac{2\pi pj}{2N+1}}, \quad p = 1 \dots N,\end{aligned}\tag{3.40}$$

where  $\underline{Q}_p$  stands for Fourier coefficient of  $p$ -th harmonic, while  $\underline{Q}_j$  represents the time variable at  $j$ th time instant. After the transformation force and torque Fourier coefficients can be used to calculate the motion of a rigid body.

For the sake of complete presentation, an expression for inverse DFT used in the next chapter is also given here:

$$\underline{Q}_j = \sum_{p=0}^N \underline{Q}_p e^{-i\frac{2\pi pj}{2N+1}}, \quad j = 1 \dots 2N+1.\tag{3.41}$$

### 3.5 Closure

This section covered rigid body dynamics. The goal was to represent the method for calculation of body motion that is compatible with the Harmonic Balance method. For this purpose governing equations for translational and rotational motion, i.e. the Newton and Euler equation, are transformed in the frequency domain. Furthermore, detailed derivation of expressions which are used to obtain position and velocity in spectral space is given.

## 4 Validation of spectral rigid body motion

### 4.1 Introduction

The method for calculating rigid body motion presented in the previous chapter is tested on two test cases. In this chapter, the validation of the rigid body motion in frequency domain is conducted, while in the next chapter results are compared to a transient simulation. All simulations are performed in the CFD software *foam-extend*.

Mathematical model presented in Chapter 3, which is used to calculate body motion in frequency domain is validated against analytical results. The goal of simulations in this case is to validate the accuracy of kinematic variables, i.e. position, velocity, angle and angular velocity acquired through equations (3.12), (3.15), (3.29) and (3.28). Since only kinematic variables are tested, forces and torques acting on the body are imposed with a constant amplitude in the frequency domain. From Eq. (3.12) it can be seen that calculation of position Fourier coefficient of  $p$ -th harmonic depends only on value of force Fourier coefficient of the same harmonic, while it does not depend on other harmonics. Hence, value for each of the  $N$  force Fourier coefficient is set independently. Analogously, if we take a look at Eq. (3.29) it can be seen that calculation of angular velocity Fourier coefficient of  $p$ -th harmonic depends only on the value of torque Fourier coefficient of the same harmonic and therefore value for each of the  $N$  torque Fourier coefficient is also set independently.

For the numerical simulations forces and torques must be set in frequency domain, however since analytical solution is obtained from Eq. (3.6) and Eq. (3.26) in time-domain, their corresponding values in time domain also must be known. Of course, if the variable is known in one of the domains, it is easily projected into the other via Fourier transform or inverse Fourier transform. Because the Fourier coefficient is a complex number, it consists of the real and imaginary part, while periodic function in time domain is a sum of sine and cosine terms. The real part of the Fourier coefficient is the amplitude of the cosine function of the corresponding harmonic, while the imaginary part is the amplitude of the sine function of the corresponding harmonic.

Validation of translational and rotational motion is conducted separately. In the case of translational motion, force that acts on a body causes translation along the  $y$  axis of global coordinate system, while in case of rotational motion, torque that acts on a body causes rotation about  $z$  axis of the global coordinate system. Since this is a 2D simulation, translation along  $y$  axis is heave motion, while rotation about the  $z$  axis is pitch rotation.

Heave motion is validated with 9 different forces. The forces differ in the number of used harmonics and in the magnitude of corresponding amplitude. Pitch rotation is also validated with 9 torques with different number of used harmonics and different magnitude of corresponding amplitude.

## 4.2 Translation

The translation is tested on a rectangular rigid body placed in the center of the computational domain as it can be seen in Figure 4.1. Since only heave motion is allowed, periodic force is acting in the direction of  $y$  axis.

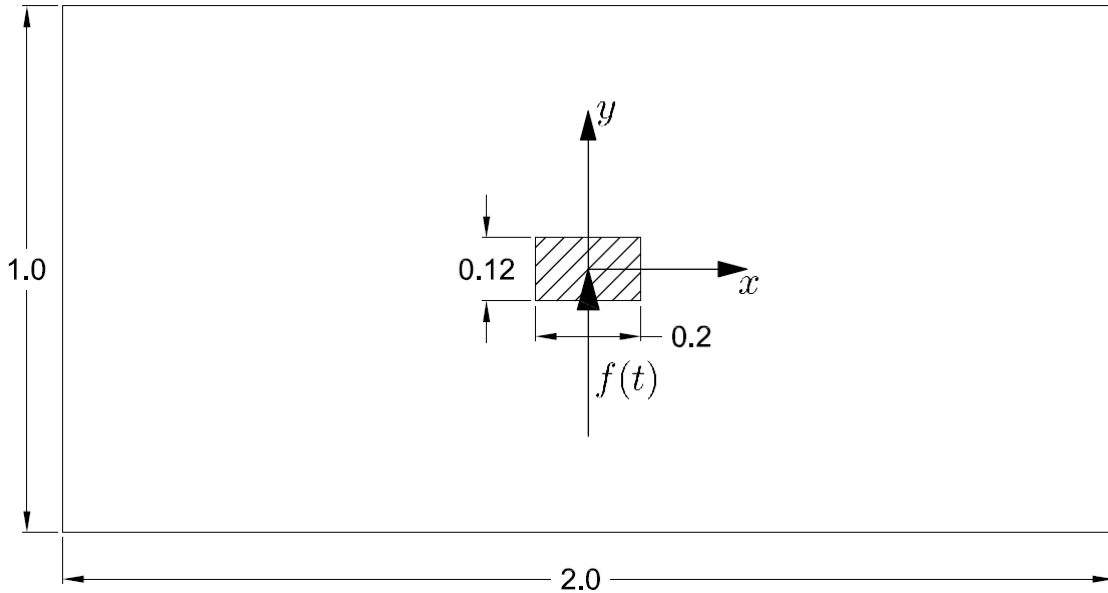


**Figure 4.1: Computational domain for the validation of translational motion.**

*Analytical solution.* Governing equation for translational motion is the vectorial equation (3.6). Since in this case only motion in the direction of  $y$  axis is allowed this equation reduces to a scalar equation. Furthermore, contribution of stiffness and damping coefficient can be neglected. Hence, equation that will be solved to obtain analytical solution is:

$$m \cdot \ddot{y}(t) = f(t), \quad (4.1)$$

where  $\ddot{y}$  is the acceleration of a body in the  $y$  direction. All simulations are conducted with  $N = 4$  harmonics. Therefore, the force can be written in a general form as:

$$\begin{aligned} f(t) &= \hat{f}_1^s \sin(\omega t) + \hat{f}_1^c \cos(\omega t) + \hat{f}_2^s \sin(2\omega t) + \hat{f}_2^c \cos(2\omega t) \\ &+ \hat{f}_3^s \sin(3\omega t) + \hat{f}_3^c \cos(3\omega t) + \hat{f}_4^s \sin(4\omega t) + \hat{f}_4^c \cos(4\omega t) \\ &= \sum_{n=1}^4 (\hat{f}_n^s \sin(n\omega t) + \hat{f}_n^c \cos(n\omega t)), \end{aligned} \quad (4.2)$$

where  $\hat{f}_n^s$  represents the  $n$ -th harmonic amplitude of the sine part of the force, while  $\hat{f}_n^c$  represents the  $n$ -th harmonic amplitude of the cosine part of the force. After insertion of a general force (Eq. (4.2)) in the governing equation (Eq. (4.1)) and then a division by mass of

the body, equation for body acceleration takes the following form:

$$\ddot{y}(t) = \frac{1}{m} \sum_{n=1}^4 (\hat{f}_n^s \sin(n\omega t) + \hat{f}_n^c \cos(n\omega t)) \quad (4.3)$$

The equation for body velocity is obtained after integrating the acceleration equation, Eq. (4.3):

$$\dot{y}(t) = \frac{1}{m} \frac{1}{n\omega} \sum_{n=1}^4 (-\hat{f}_n^s \cos(n\omega t) + \hat{f}_n^c \sin(n\omega t)) + C_1. \quad (4.4)$$

Analogous equation for the position of the centre of mass is obtained after integrating the velocity equation, Eq. (4.4):

$$y(t) = \frac{1}{m} \frac{1}{(n\omega)^2} \sum_{n=1}^4 (-\hat{f}_n^s \sin(n\omega t) - \hat{f}_n^c \cos(n\omega t)) + C_1 \cdot t + C_2. \quad (4.5)$$

Integration constants  $C_1$  and  $C_2$  are usually determined from the initial conditions i.e. position and velocity of the body in initial time instance, but in this case initial values are calculated with the use of basic assumptions of Harmonic Balance. The basic assumption of the Harmonic Balance is that all variables and functions are periodic. In order to validate the results of spectral motion algorithm position and velocity given with Eq. (4.4) and Eq. (4.5) will be transformed in the frequency domain. Therefore, the position and velocity functions must remain periodic. Also it was stated earlier that in the existing model mean value of position and velocity in the frequency domain is not solved, i.e. it remains zero throughout the simulation. Hence, integration constant  $C_1$  is obtained from condition of zero mean value of velocity in the time domain.

The mean value theorem for integrals reads:

$$\bar{f}(x) = \frac{1}{b-a} \int_a^b f(x) dx. \quad (4.6)$$

If the mean value theorem is used on the velocity equation (Eq. (4.4)) and if the fact that the mean value must be zero is taken into account, equation for determination of integration constant  $C_1$  takes the following form:

$$\frac{1}{T} \int_0^T \left[ \frac{1}{m} \frac{1}{n\omega} \sum_{n=1}^4 (-\hat{f}_n^s \cos(n\omega t) + \hat{f}_n^c \sin(n\omega t)) + C_1 \right] dt = 0. \quad (4.7)$$

After integration and further simplification of Eq. (4.7), constant  $C_1$  is obtained and it is equal to zero,  $C_1 = 0$ . This result is expected, since the term containing  $C_1$  is responsible for non-periodic linear change. Hence, in order for position to remain periodic  $C_1$  must be zero.

The value of integration constant  $C_2$  is obtained after applying the mean value theorem (see Eq. (4.6)) on Eq. (4.5). Knowing that  $C_1 = 0$ , it can be written:



$$\frac{1}{T} \int_0^T \left[ \frac{1}{m} \frac{1}{(n\omega)^2} \sum_{n=1}^4 (-\hat{f}_n^s \sin(n\omega t) - \hat{f}_n^c \cos(n\omega t)) + C_2 \right] dt = 0. \quad (4.8)$$

Analogous to Eq. (4.7), after integration and further simplification of Eq. (4.8), integration constant  $C_2$  is obtained,  $C_2 = 0$ .

Now that the integration constants are obtained the final form of governing equations for heave motion can be written:

$$\begin{aligned} \ddot{y}(t) &= \frac{1}{m} \sum_{n=1}^4 (\hat{f}_n^s \sin(n\omega t) + \hat{f}_n^c \cos(n\omega t)), \\ \dot{y}(t) &= \frac{1}{m} \frac{1}{n\omega} \sum_{n=1}^4 (-\hat{f}_n^s \cos(n\omega t) + \hat{f}_n^c \sin(n\omega t)), \\ y(t) &= \frac{1}{m} \frac{1}{(n\omega)^2} \sum_{n=1}^4 (-\hat{f}_n^s \sin(n\omega t) - \hat{f}_n^c \cos(n\omega t)). \end{aligned} \quad (4.9)$$

### 4.3 Rotation

The rotation is tested on a rectangular rigid body placed in the center of the computational domain shown in Figure 4.2. Since only pitch motion is allowed, periodic torque is acting in the direction of  $z$  axis.

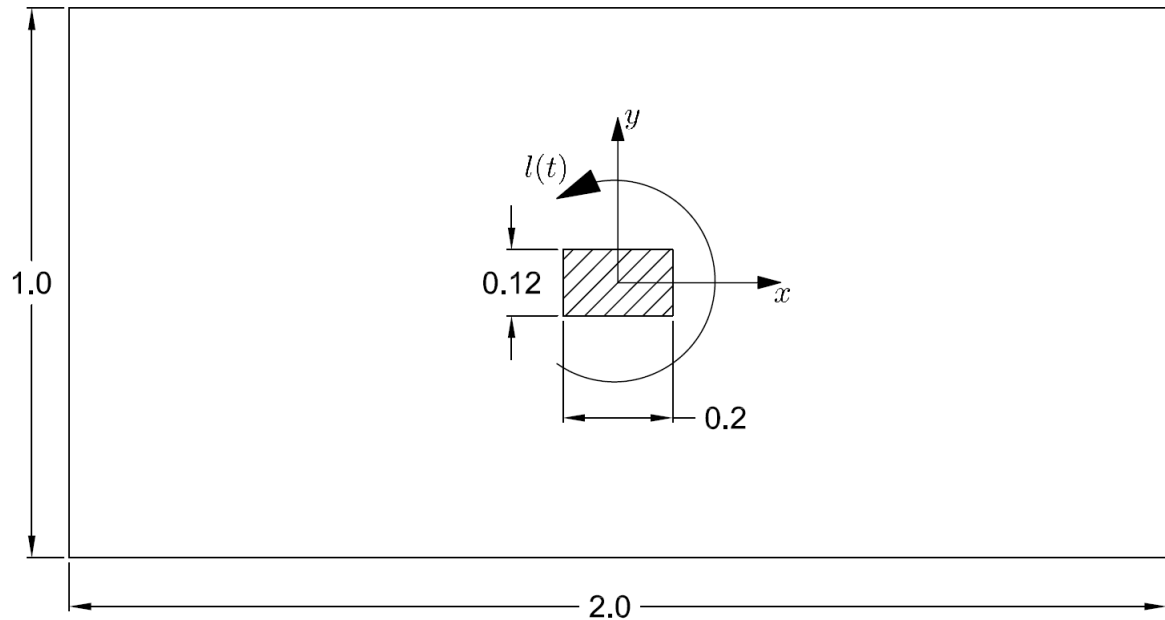


**Figure 4.2: Validation of pitch rotation**

*Analytical solution.* Governing equation for the rotational motion of a rigid body is the Euler equation (3.23). In the case of planar rigid body dynamics, the Euler equation can be

simplified. Since the only rotation that exist is the rotation about the  $z$  axis, tensor of inertia  $\underline{J}$  can be replaced with the moment of inertia  $J_{zz}$ . Since  $\underline{J}$  is now replaced with scalar value, the second term of Euler equation (3.23) consists of a cross product of colinear vectors which is equal to zero. Furthermore, in the planar dynamics angular velocity is equal to the angle differentiation:

$$\omega = \frac{d\theta}{dt}. \quad (4.10)$$

Hence, the Euler equation for the planar dynamics takes the following form:

$$J_{zz}\ddot{\theta} = l(t), \quad (4.11)$$

where  $\ddot{\theta}$  stands for the angular acceleration of a rigid body, while  $l(t)$  stands for the acting torque. Analogous to the validation of the translation, rotation is also validated with the simulations with  $N = 4$  harmonics. Therefore, the torque can be written in the same general form as force (Eq. (4.2)):

$$l(t) = \sum_{n=1}^4 (\hat{l}_n^s \sin(n\omega t) + \hat{l}_n^c \cos(n\omega t)), \quad (4.12)$$

where  $\hat{l}_n^s$  stands for the  $n$ -th harmonic amplitude of the sine part of torque, while  $\hat{l}_n^c$  stands for the  $n$ -th harmonic amplitude of the cosine part of torque. Equation for angular acceleration is obtained after the insertion of generalized torque in Eq. (4.11) and division by  $J_{zz}$ :

$$\ddot{\theta} = \frac{1}{J_{zz}} \sum_{n=1}^4 (\hat{l}_n^s \sin(n\omega t) + \hat{l}_n^c \cos(n\omega t)). \quad (4.13)$$

The equation for angular velocity is obtained after the integration of the angular acceleration equation, Eq. (4.13):

$$\dot{\theta}(t) = \frac{1}{J_{zz}} \frac{1}{n\omega} \sum_{n=1}^4 (-\hat{l}_n^s \cos(n\omega t) + \hat{l}_n^c \sin(n\omega t)) + C_3, \quad (4.14)$$

while equation for the determination of orientation (angle) is obtained after integration of the angular velocity equation, Eq. (4.14):

$$\theta(t) = \frac{1}{J_{zz}} \frac{1}{(n\omega)^2} \sum_{n=1}^4 (-\hat{l}_n^s \sin(n\omega t) - \hat{l}_n^c \cos(n\omega t)) + C_3 \cdot t + C_4. \quad (4.15)$$

Values of integration constants  $C_3$  and  $C_4$  are determined analogous to the determination of the values of integration constant  $C_1$  and  $C_2$ . After the use of the mean value theorem on the Eq. (4.14) and Eq. (4.15), respectively, we get that both constants must be equal to the zero. Hence, equations used to determine the analytical solution for pitch rotation are:

$$\begin{aligned}
\ddot{\theta} &= \frac{1}{J_{zz}} \sum_{n=1}^4 (\hat{l}_n^s \sin(n\omega t) + \hat{l}_n^c \cos(n\omega t)), \\
\dot{\theta}(t) &= \frac{1}{J_{zz}} \frac{1}{n\omega} \sum_{n=1}^4 (-\hat{l}_n^s \cos(n\omega t) + \hat{l}_n^c \sin(n\omega t)), \\
\theta(t) &= \frac{1}{J_{zz}} \frac{1}{(n\omega)^2} \sum_{n=1}^4 (-\hat{l}_n^s \sin(n\omega t) - \hat{l}_n^c \cos(n\omega t)).
\end{aligned} \tag{4.16}$$

#### 4.4 Setup of the numerical simulation

The computational domain is discretized with `blockMesh` utility which is a part of `foam-extend` with dimensions shown in Figure 4.1 (and in Figure 4.2). The finite volume mesh is shown on Figure 4.3. Mesh is made of 8 blocks, with total of 1898 hexahedra cells.

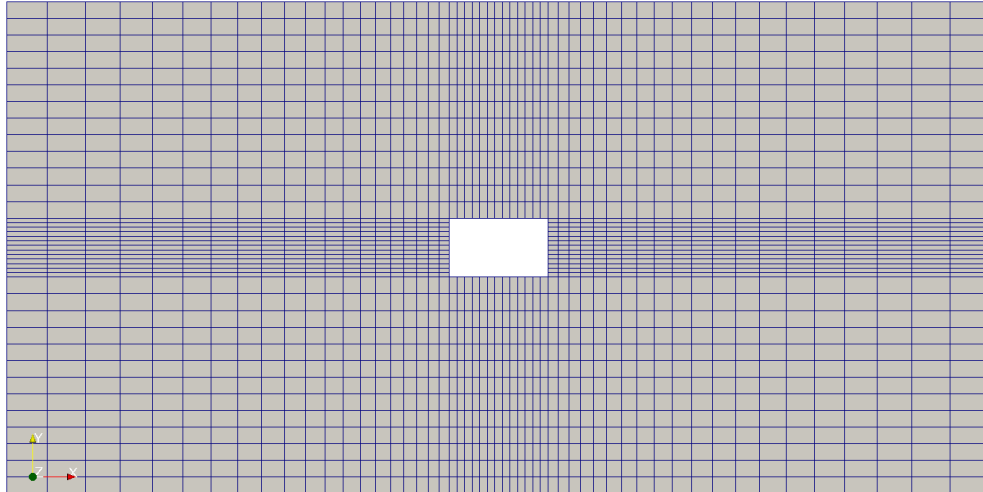


**Figure 4.3: First validation test case mesh**

The rigid body is placed in a single phase fluid flow. Since the flow field is not important for the force/torque calculation in this case, boundary conditions are not discussed here. The mass of the rigid body is  $m = 10\text{kg}$ , while the moment of inertia is set to  $J_{zz} = 100\text{kg} \cdot \text{m}^3$ . The period of oscillation is set to  $T = 0.7\text{s}$ , yielding the frequency of oscillation  $\omega = 8.976\text{rad/s}$ .

In the HB method every variable and field is calculated in  $2N + 1$  equally distanced time instants. The spacing between time instants is  $\Delta t = T/(2N + 1)$ . Since in our simulations  $N = 4$  harmonics are used and the base period of oscillation is  $T = 0.7\text{s}$ , time instants in which the motion is calculated are separated by  $\Delta t = 0.0778\text{s}$ .

Since this solver is designed to simulate the wave-induced ship motion, calculation of the flow is its integral part and cannot be avoided, but as it was stated earlier this case is designed in a way that decouples flow and motion. In all following simulations motion starts after one hundred iterations, while the first one hundred iterations are used to ensure stable flow solution.

This is noticeable in figures showing the convergence of the numerical solution.

## 4.5 Results of numerical simulations

As stated before a total of eighteen simulations are performed in order to check the accuracy of motion solution algorithm. First nine simulations are performed to check the translation, while the remaining simulations are performed to check the rotational motion. The complexity of force and torque is increasing with the number of simulations, i.e the most complex force is in simulation No. 9, while the most complex torque is in the simulation No. 18.

### 4.5.1 Translation

Forces used in the validation of translational motion are presented in Table 4.1.  $F_{py}$  stands for  $p$ th order harmonic amplitude of force in the  $y$  axis direction.

**Table 4.1: Forces in the simulations for the translational motion validation.**

Order, $p$		1st	2nd	3rd	4th
Simulation 1	$Re(F_{py})$	0	0	0	0
	$Im(F_{py})$	1	0	0	0
Simulation 2	$Re(F_{py})$	1	0	0	0
	$Im(F_{py})$	0	0	0	0
Simulation 3	$Re(F_{py})$	0	0	0	0
	$Im(F_{py})$	40	0	0	0
Simulation 4	$Re(F_{py})$	-40	0	0	0
	$Im(F_{py})$	0	0	0	0
Simulation 5	$Re(F_{py})$	30	0	0	0
	$Im(F_{py})$	20	0	0	0
Simulation 6	$Re(F_{py})$	0	0	0	0
	$Im(F_{py})$	20	15	0	0
Simulation 7	$Re(F_{py})$	-10	20	0	0
	$Im(F_{py})$	0	0	0	0
Simulation 8	$Re(F_{py})$	150	0	0	0
	$Im(F_{py})$	0	-120	0	0
Simulation 9	$Re(F_{py})$	0	0	15	0
	$Im(F_{py})$	50	30	0	45

The results of translational motion simulations are presented in Table 4.2. Those results are showing that the numerical and analytical solution for every simulation is identical, i.e. the error is 0%. Convergence of the Fourier coefficients of position  $X_{p_y}$  and velocity  $U_{p_y}$  is shown in figures 4.4a and 4.4b, respectively, while the comparison of numerical and analytical solution for the position  $y$  and velocity  $u_y$  in the time domain is shown in figures 4.5a and 4.5b, respectively. Convergence of the numerical solution and the comparison of numerical and analytical solution in the time domain is given for the ninth simulation since in that simulation acting force is the most complex (see forces in Table 4.1).

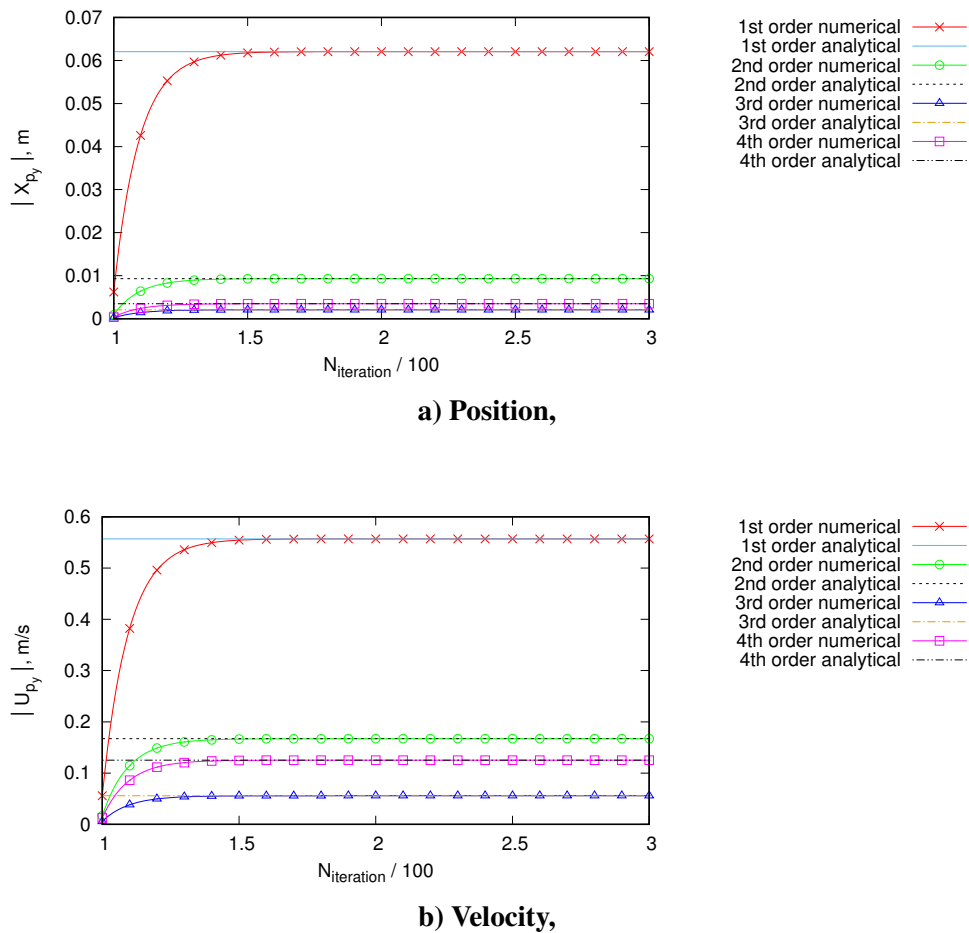
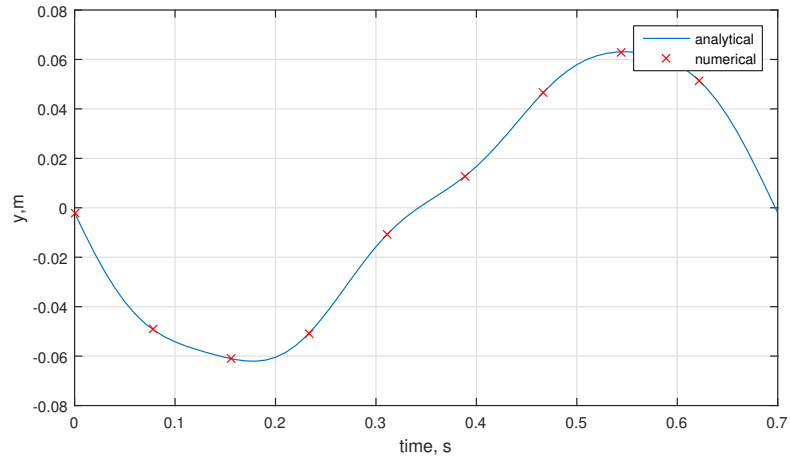
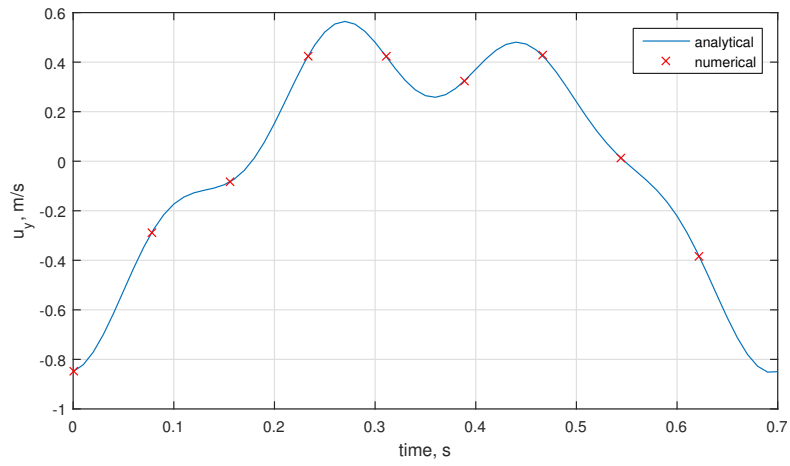


**Figure 4.4: Convergence of Fourier coefficients in the 9th simulation.**



a) Position,



b) Velocity,

Figure 4.5: Time domain variable during one period in the 9th simulation.

**Table 4.2: Results of the translational validation simulations.**

Order, $p$			1st	2nd	3rd	4th
Simulation 1	$ X_{p_y} $ , m	numerical	0.0012411	0	0	0
		analytical	0.0012411	0	0	0
	$ U_{p_y} $ , m/s	numerical	0.0111408	0	0	0
		analytical	0.0111408	0	0	0
Simulation 2	$ X_{p_y} $ , m	numerical	0.0012411	0	0	0
		analytical	0.0012411	0	0	0
	$ U_{p_y} $ , m/s	numerical	0.0111408	0	0	0
		analytical	0.0111408	0	0	0
Simulation 3	$ X_{p_y} $ , m	numerical	0.049647	0	0	0
		analytical	0.049647	0	0	0
	$ U_{p_y} $ , m/s	numerical	0.44563	0	0	0
		analytical	0.44563	0	0	0
Simulation 4	$ X_{p_y} $ , m	numerical	0.049647	0	0	0
		analytical	0.049647	0	0	0
	$ U_{p_y} $ , m/s	numerical	0.44563	0	0	0
		analytical	0.44563	0	0	0
Simulation 5	$ X_{p_y} $ , m	numerical	0.044751	0	0	0
		analytical	0.044751	0	0	0
	$ U_{p_y} $ , m/s	numerical	0.40168	0	0	0
		analytical	0.40168	0	0	0
Simulation 6	$ X_{p_y} $ , m	numerical	0.024823	0.22281	0	0
		analytical	0.024823	0.22281	0	0
	$ U_{p_y} $ , m/s	numerical	0.0046544	0.083556	0	0
		analytical	0.0046544	0.083556	0	0
Simulation 7	$ X_{p_y} $ , m	numerical	0.012411	0.11140	0	0
		analytical	0.012411	0.11140	0	0
	$ U_{p_y} $ , m/s	numerical	0.0062059	0.11140	0	0
		analytical	0.0062059	0.11140	0	0
Simulation 8	$ X_{p_y} $ , m	numerical	0.18617	1.67112	0	0
		analytical	0.18617	1.67112	0	0
	$ U_{p_y} $ , m/s	numerical	0.037235	0.66845	0	0
		analytical	0.037235	0.66845	0	0
Simulation 9	$ X_{p_y} $ , m	numerical	0.062059	0.00930888	0.0020686	0.0034908
		analytical	0.062059	0.00930888	0.0020686	0.0034908
	$ U_{p_y} $ , m/s	numerical	0.55704	0.16711	0.055704	0.12533
		analytical	0.55704	0.16711	0.055704	0.12533

#### 4.5.2 Rotation

The torque used in the validation of rotational motion solution is presented in Table 4.1.  $L_{p_z}$  stands for  $p$ th order harmonic amplitude of torque in  $z$  axis direction. To avoid confusion with translational simulations, rotational simulations are denoted with the numbers ranging from 10 to 18.

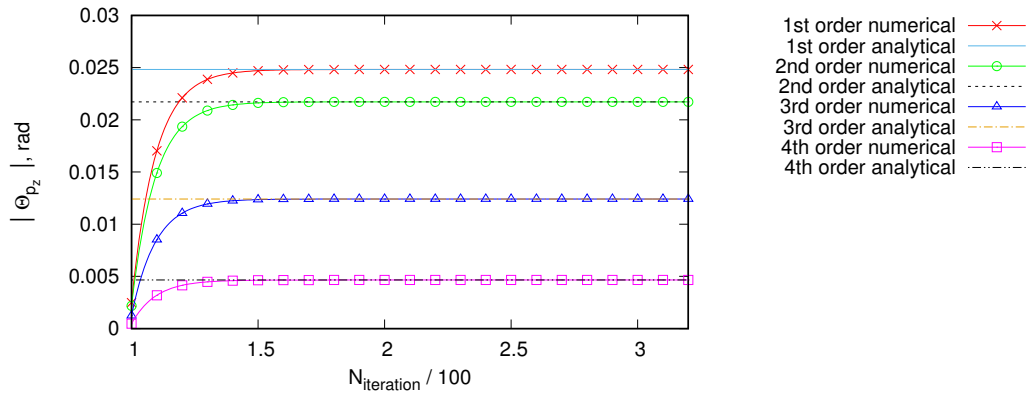
**Table 4.3: Torque in simulations for rotational motion validation.**

Order, $p$		1st	2nd	3rd	4th
Simulation 10	$Re(L_{p_z})$	0	0	0	0
	$Im(L_{p_z})$	1	0	0	0
Simulation 11	$Re(L_{p_z})$	1	0	0	0
	$Im(L_{p_z})$	0	0	0	0
Simulation 12	$Re(L_{p_z})$	0	0	0	0
	$Im(L_{p_z})$	-800	0	0	0
Simulation 13	$Re(L_{p_z})$	800	0	0	0
	$Im(L_{p_z})$	0	0	0	0
Simulation 14	$Re(L_{p_z})$	-400	0	0	0
	$Im(L_{p_z})$	700	0	0	0
Simulation 15	$Re(L_{p_z})$	0	0	0	0
	$Im(L_{p_z})$	600	600	0	0
Simulation 16	$Re(L_{p_z})$	1200	1800	0	0
	$Im(L_{p_z})$	0	0	0	0
Simulation 17	$Re(L_{p_z})$	0	800	0	0
	$Im(L_{p_z})$	-300	0	0	0
Simulation 18	$Re(L_{p_z})$	200	0	0	-600
	$Im(L_{p_z})$	0	700	-900	0

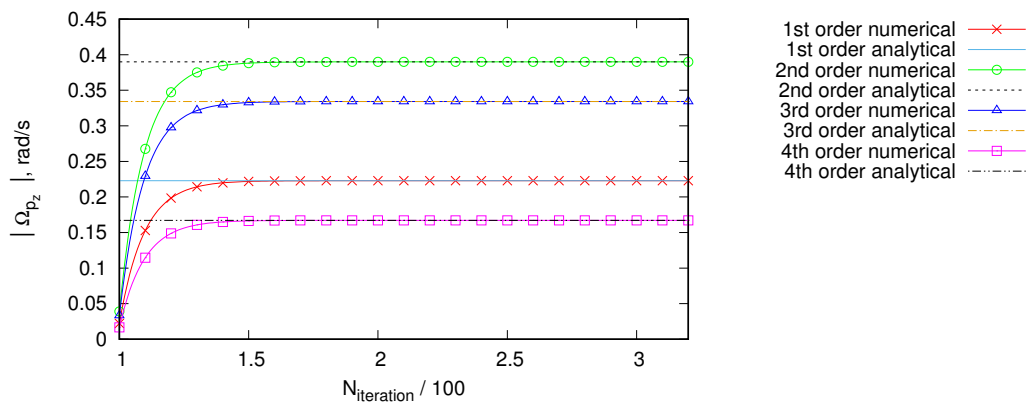
The results of rotational motion simulations are presented in Table 4.3. The numerical and analytical solution for the Fourier coefficients of Euler angle  $\Theta_{p_z}$  and angular velocity  $\Omega_{p_z}$  is identical in every simulation, hence the error is 0%. Convergence of the Euler angle and angular velocity Fourier coefficients can be seen in figures 4.6a and 4.6b, respectively. Additionally, comparison of numerical and analytical solution for time domain Euler angle  $\theta_z$  and angular velocity  $\omega_z$  can be found in figures 4.7a and 4.7b, respectively. Convergence of the numerical



solution and the comparison of numerical and analytical solution in the time domain is given for the eighteenth simulation, since in that simulation acting torque is the most complex (see torques in Table 4.3).

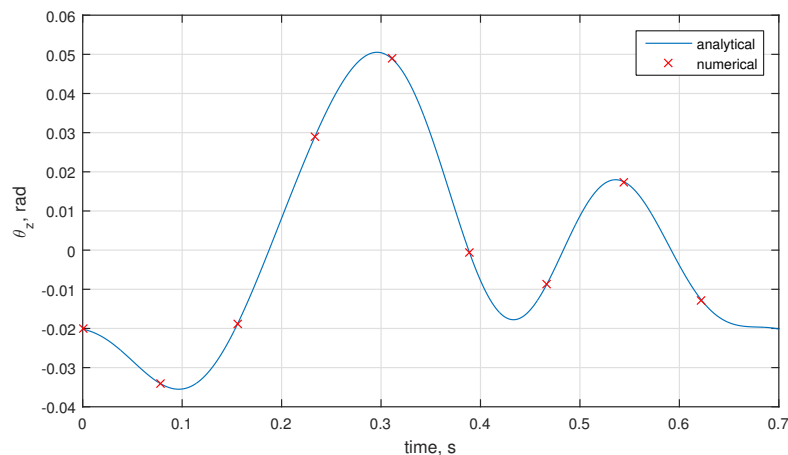


a) Euler angle,

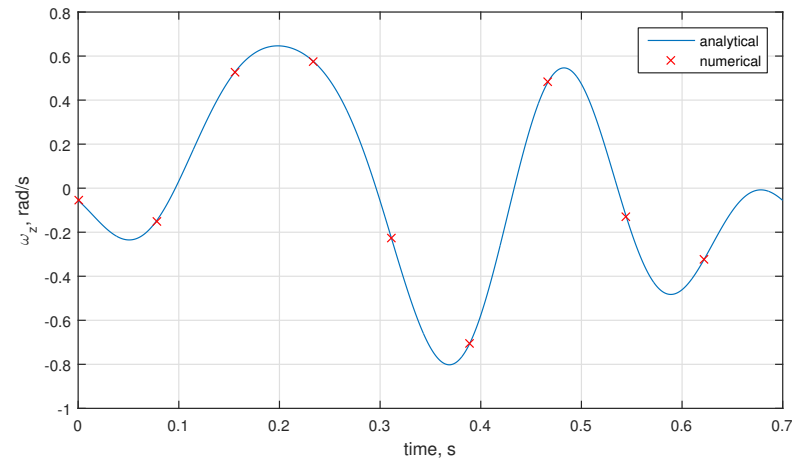


b) Angular velocity,

Figure 4.6: Convergence of Fourier coefficients in the 18th simulation.



a) Euler angle,



**b) Angular velocity,**

**Figure 4.7: Time domain variables during one period in the 18th simulation.**

Table 4.4: Results of rotational validation simulations.

Order, $p$			1st	2nd	3rd	4th
Simulation 10	$ \Theta_{p_z} $ , rad	numerical	0.00012411	0	0	0
		analytical	0.00012411	0	0	0
	$ \Omega_{p_z} $ , rad/s	numerical	0.00111408	0	0	0
		analytical	0.00111408	0	0	0
Simulation 11	$ \Theta_{p_z} $ , rad	numerical	0.00012411	0	0	0
		analytical	0.00012411	0	0	0
	$ \Omega_{p_z} $ , rad/s	numerical	0.00111408	0	0	0
		analytical	0.00111408	0	0	0
Simulation 12	$ \Theta_{p_z} $ , rad	numerical	0.099294	0	0	0
		analytical	0.099294	0	0	0
	$ \Omega_{p_z} $ , rad/s	numerical	0.89126	0	0	0
		analytical	0.89126	0	0	0
Simulation 13	$ \Theta_{p_z} $ , rad	numerical	0.099294	0	0	0
		analytical	0.099294	0	0	0
	$ \Omega_{p_z} $ , rad/s	numerical	0.89126	0	0	0
		analytical	0.89126	0	0	0
Simulation 14	$ \Theta_{p_z} $ , rad	numerical	0.10006	0	0	0
		analytical	0.10006	0	0	0
	$ \Omega_{p_z} $ , rad/s	numerical	0.89820	0	0	0
		analytical	0.89820	0	0	0
Simulation 15	$ \Theta_{p_z} $ , rad	numerical	0.074471	0.018617	0	0
		analytical	0.074471	0.018617	0	0
	$ \Omega_{p_z} $ , rad/s	numerical	0.66845	0.33422	0	0
		analytical	0.66845	0.33422	0	0
Simulation 16	$ \Theta_{p_z} $ , rad	numerical	0.14894	0.055853	0	0
		analytical	0.14894	0.055853	0	0
	$ \Omega_{p_z} $ , rad/s	numerical	0.1.33692	1.00267	0	0
		analytical	1.33690	1.00267	0	0
Simulation 17	$ \Theta_{p_z} $ , rad	numerical	0.037235	0.024823	0	0
		analytical	0.037235	0.024823	0	0
	$ \Omega_{p_z} $ , rad/s	numerical	0.33422	0.44563	0	0
		analytical	0.33422	0.44563	0	0
Simulation 18	$ \Theta_{p_z} $ , rad	numerical	0.024823	0.021720	0.012411	0.0046544
		analytical	0.024823	0.021720	0.012411	0.0046544
	$ \Omega_{p_z} $ , rad/s	numerical	0.22281	0.38992	0.33422	0.16711
		analytical	0.22281	0.38992	0.33422	0.16711

## **4.6 Closure**

In this chapter, a simple test case is designed and simulated in order to check the accuracy of the motion solution method presented in the previous chapter. Variety of translational and rotational simulations are performed in order to cover a wide range of cases that are possible in practice. The conclusion of all simulations is that the motion algorithm produces results that are exactly the same as the analytical solution. Next step is to perform simulations in which the motion is induced by a surface wave.

## 5 Motion validation of a submerged body

### 5.1 Introduction

In this chapter heave motion of a body is compared to the results of a transient simulation. Transient simulation results obtained using the present numerical framework are considered referent since they have been thoroughly verified and validated in numerous publications [8, 25, 26].

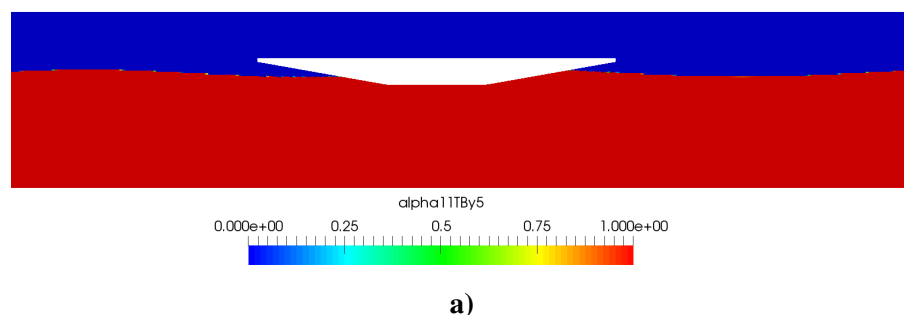
This chapter is divided into five sections. In the first section, the problems that have been experienced during the design of the test case are presented. Next, the setup that is used for HB simulation will be presented. Additionally, results of the corresponding transient simulation are given. In the last section the results of the HB simulation and their comparison with the transient simulation results are presented.

### 5.2 Design of the test case

The goal of this test is to compare the motion calculated using Harmonic Balance with results of the corresponding transient simulation. Since this is the first simulation in which the fluid flow and rigid body motion are coupled, a simple  $2D$  test is designed. The rigid body in a shape of trapezoid is chosen because it best approximates the shape of a ship.

Trapezoidal body was placed on the free surface, however this simulation diverged. Since this is a  $2D$  case, incoming air could not flow to the sides of the body, instead it was getting trapped under the bow. This accumulation of air eventually caused divergence of the solution since this phenomena has a high frequency, which is not captured by the Fourier series expansion (see Eq. (2.14)).

Instabilities on the free surface due to the air accumulation can be seen in Figure 5.1b, while the free surface at the beginning of the simulation can be seen in Figure 5.1a. Although the free surface is captured with LS method, for clarity the free surface is presented using  $\alpha$  volume fraction.



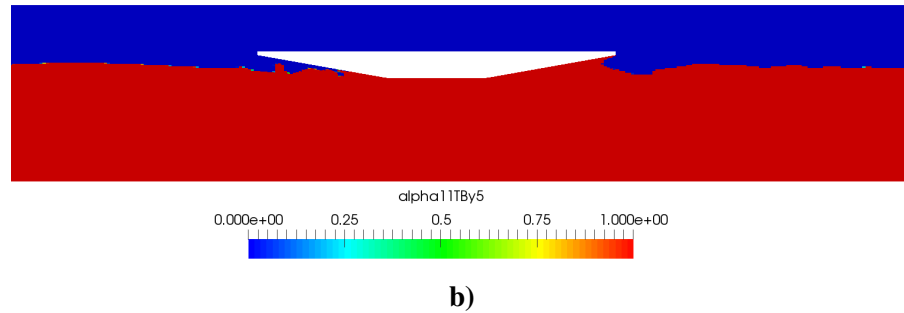


**Figure 5.1:** (a) Free surface at the beginning of a simulation, (b) Air accumulation under the bow of the body.

In order to avoid the divergence of the simulation, the rigid body is submerged under the free surface. Hence, trapezoidal shape of the body is no longer suitable since its sharp edges would cause unwanted transient effects in the numerical solution. Therefore, a symmetrical rigid body in a shape of a hexagon is selected for further study. As it can be seen in Figure 5.2, the length of the rigid body is  $L_b = 6$  m, while its height is  $h_b = 0.6$  m.

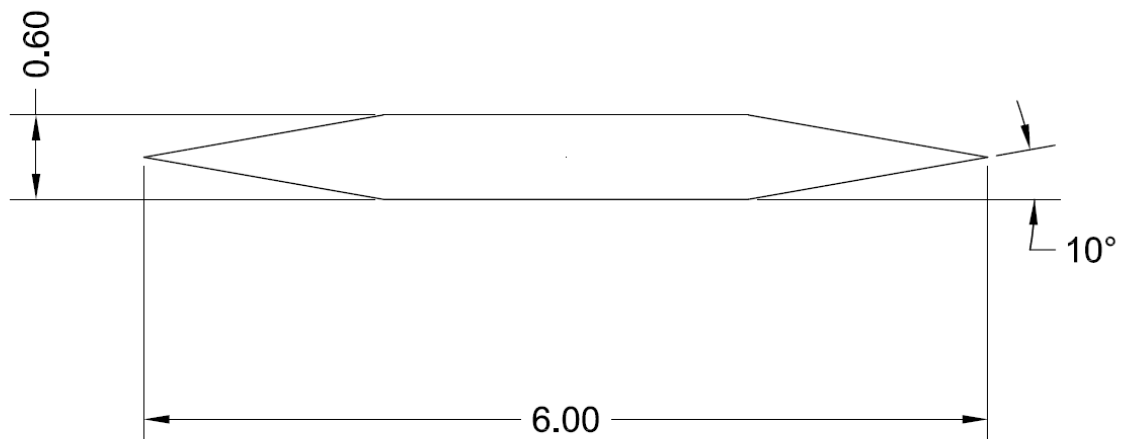


**Figure 5.2:** Dimensions of the rigid body.

Initially, the rigid body is placed at a depth of 1.67 m. This depth is used in the reference transient simulation, while for the reasons explained in the following text the depth is modified in the HB simulation. Positions of the upstream and downstream boundaries of the computational domain are selected in a way to avoid wave reflection. Hence, the length of the computational domain upstream of the body is equal to two and a half lengths of the free surface wave,  $2.5\lambda$ , while the length of the domain in the downstream direction is equal to three and a half lengths of the free surface wave,  $3.5\lambda$ . Domain height is 6.71 m, where the water takes up 81.37% i.e. 5.46 m. Computational domain dimensions can be seen in Figure 5.3.

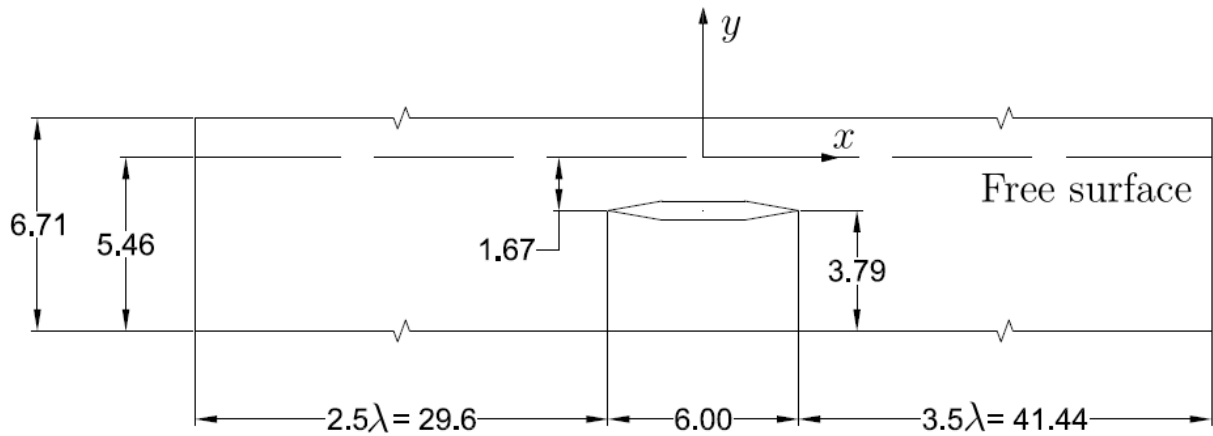


**Figure 5.3: Computational domain dimensions for the transient simulation.**

For the mass of the body that corresponds to the buoyancy force acting on the body, a non-periodic heave motion is obtained as it can be seen in Figure 5.4.

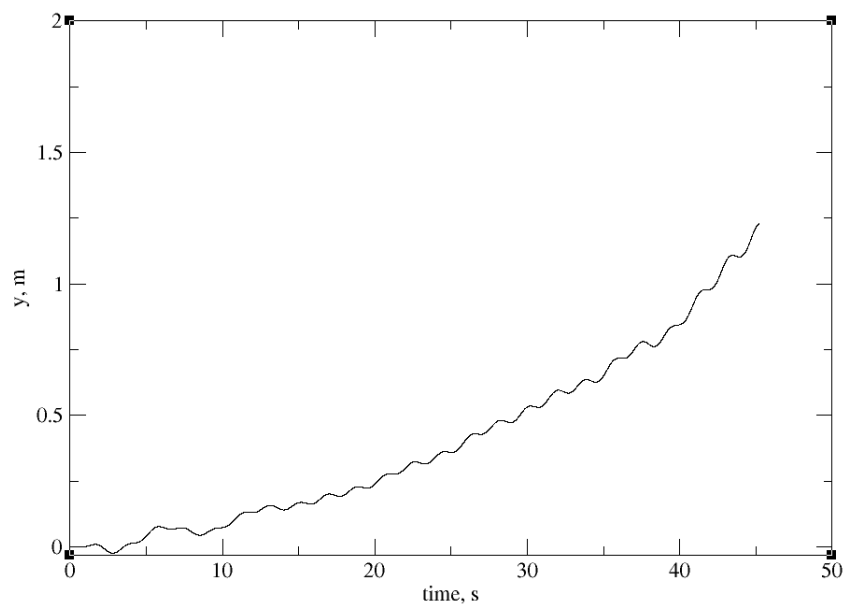


**Figure 5.4: Existence of mean value of motion.**

In order to use current HB motion algorithm which cannot calculate the mean value of motion, the mean value changes in the transient simulation must be nullified. Nullification of the mean value changes in the transient simulation is achieved by using a linear spring and the body mass greater than the buoyancy force.

Since the weight of the body is greater than the buoyancy force, the body is sinking until the equilibrium of forces is achieved. Furthermore, since the mean value motion cannot be calculated with HB simulation, the value for which the body sank in the transient simulation must be taken into account beforehand i.e. in the HB simulation body needs to be placed deeper by the mean value of motion from transient simulation. The mean value motion of the transient

simulation is 0.492934 m. Therefore, although overall dimensions of the computational domain are equal in the case of the transient and HB simulation, the position of the body is different as it can be seen in Figure 5.5.

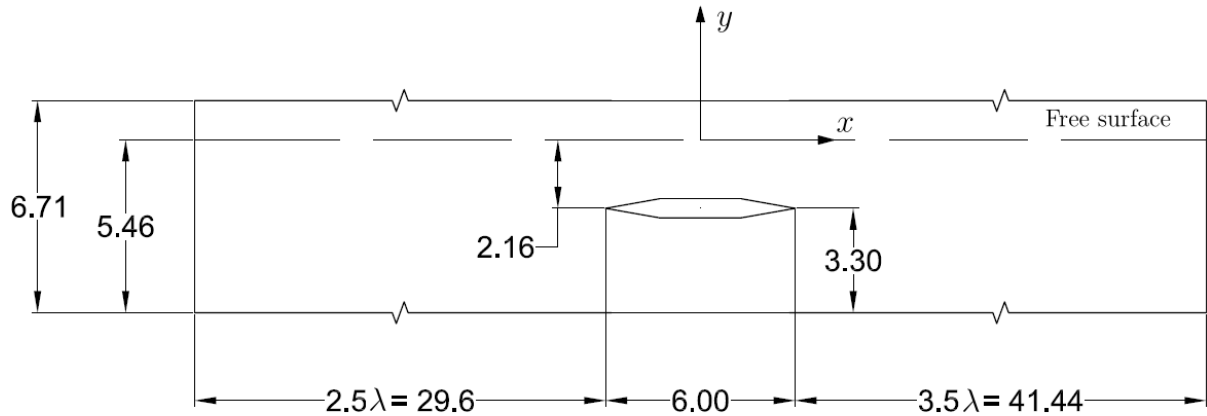


**Figure 5.5: Computational domain dimensions for the HB simulation.**

### 5.3 Numerical case set up

In this chapter set up for the HB simulation is presented in detail, and a brief review of the reference transient simulation is given.

#### 5.3.1 Discretised computational domain

Finite Volume (FV) mesh is generated using software *Pointwise* [27]. The mesh is block structured with three longitudinal and six vertical blocks. All of 32718 cells are in the shape of hexahedra. In order to reduce the number of cells this mesh is graded in both longitudinal and vertical direction. In the longitudinal direction cells are graded towards the middle where object is placed, while in the vertical direction there are two distinct levels of mesh grading. First level of grading represents cells around body that are mildly graded, while the second level of cells grading is near the by free surface. Mesh is made with 10 elements per wave height. Full view of the FV mesh can be seen in Figure 5.6, while the zoomed detail of the mesh which shows the mesh around the body and near the free surface can be seen in Figure 5.7.

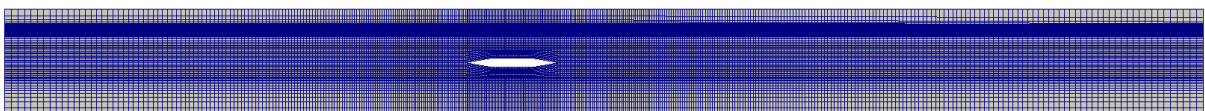


**Figure 5.6: Full view of the mesh.**



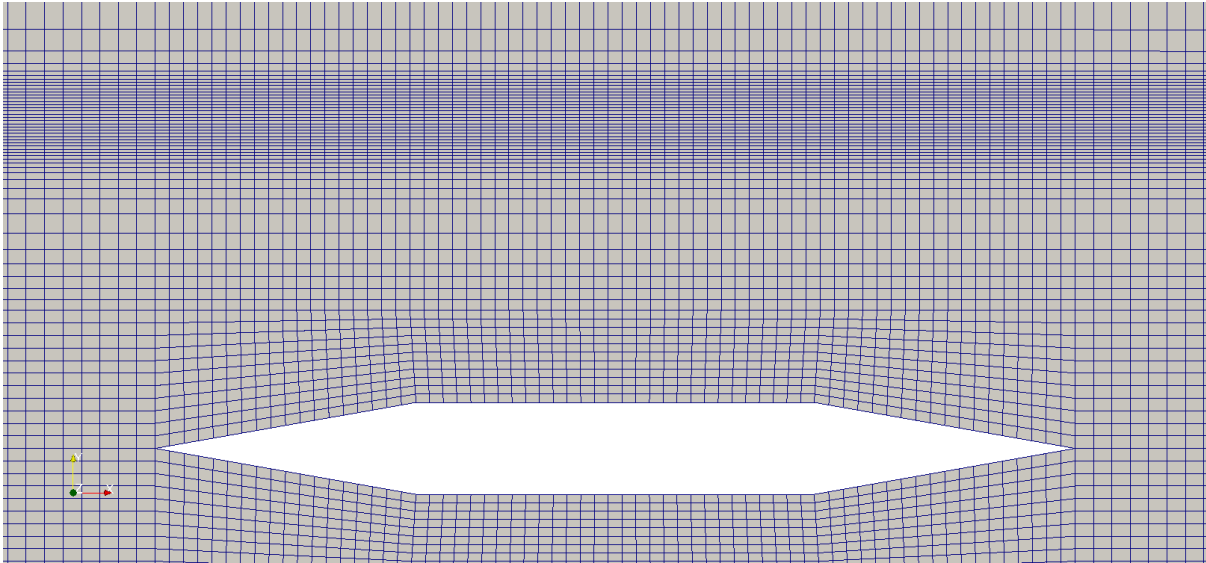


**Figure 5.7: Zoomed view of the mesh in the middle of domain.**

### 5.3.2 Relaxation zones

Relaxation zones are used to prevent the wave reflection which can disrupt CFD results. Wave reflection occurs when the perturbation components do not vanish near the boundaries of the domain [3]. In relaxation zones, the solution is a linear combination of CFD and potential flow solution. It was shown by Vukčević et al [3] that when the length of the relaxation zone is greater than  $\lambda$  amplitude of the reflected wave is below 1% of the incident wave amplitude. Therefore, the length of the relaxation zone at inlet and outlet, in this case, is set to one and a half wave length,  $\lambda_r = 1.5\lambda$ . Figure 5.8 shows the weight field that represents relaxation zones. When the weight field is equal to zero,  $w = 0$ , the solution consists only of the CFD results, and when the weight field is equal to one,  $w = 1$ , solution is comprised of the incident field.

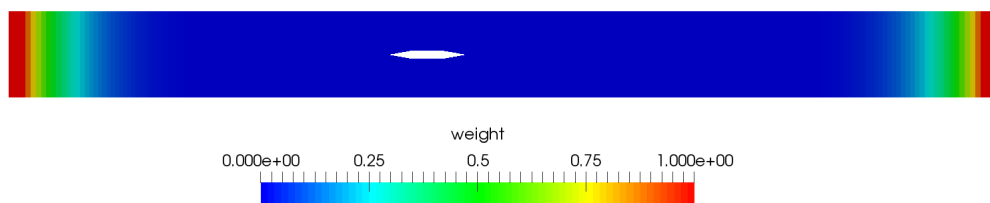


**Figure 5.8: Relaxation zones represented with a weight field.**

### 5.3.3 Wave parameters

The dimensions of the computational domain and the length of relaxation zones are determined with the respect to the wave length of the free surface wave. In this case the wave length is  $\lambda = 11.84\text{m}$ , while the wave height is  $h = 0.196\text{m}$ . Angular frequency  $\omega$  can be calculated

with the following equation from the linear wave theory:

$$\omega = \sqrt{\frac{2\pi g}{\lambda}}, \quad (5.1)$$

where  $g = 9.81 \text{ m/s}^2$  stands for gravitational acceleration. With the known angular frequency period  $T$  or wave frequency  $f_w$  can be easily calculated. However, the speed of the submerged body must be taken into account. The wave would affect the body motion with the frequency calculated with Eq. (5.1) in case of a stationary rigid body. Since the rigid body has the speed of  $U = 2 \text{ m/s}$  in the  $-x$  direction (see Figure 5.4), it will encounter waves at a higher frequency. It should be stated here that waves are propagating in the direction of the  $x$  axis. Therefore, the encounter frequency is calculated by the following equation:

$$\omega_e = \omega \left( 1 + \frac{U\omega}{g} \right). \quad (5.2)$$

All relevant wave parameters are shown in Table 5.1.

**Table 5.1: Wave parameters.**

Wave height	$H$ , m	0.196
Wave length	$\lambda$ , m	11.84
Wave frequency	$\omega$ , rad/s	2.2816
Speed of a body	$U$ , m/s	2
Encounter frequency	$\omega_e$ , rad/s	3.343
Encounter period	$T_e$ , s	1.8795
Relaxation zone length	$\lambda_r$ , m	17.76

It should be noted that in our simulations rigid body does not move in the direction of  $-x$  axis, but the same effect is produced by inducing a steady current in the opposite direction.

### 5.3.4 Boundary conditions

Free surface and velocity are initialised using the nonlinear stream function wave theory [28] solution at given time instances. Therefore, boundary conditions are set up in a way that enables velocity and free surface initialisation with the wave theory, i.e. the perturbation components of the velocity  $\underline{u}_p$  and LS field  $\psi_p$ , as well as dynamic pressure are initialised to zero.

### 5.3.5 Simulation properties

*Phases.* Two phases used in this case are water and air. Density of the water is  $\rho_w = 1000 \text{ kg/m}^3$ , while its kinematic viscosity is  $\nu_w = 1 \cdot 10^{-6}$ . Density of air in this case is set to  $\rho_a = 1 \text{ kg/m}^3$ , while its kinematic viscosity is set to  $\nu_a = 1.48 \cdot 10^{-5}$ . The flow of both phases is laminar.

*Rigid body.* The body mass is set to  $m = 1000\text{kg}$ , while the stiffness coefficient of linear spring is set to  $c = 9000\text{Ns/m}$ .

*Numerical schemes.* In order to obtain numerical solution for the governing equations that are described in Chapter 2, FV discretization process must be carried out. Once the discretisation is carried out different numerical schemes for the convection and diffusion terms can be chosen [29].

*Convection.* For the convection terms of the perturbation components following numerical schemes are used: in the momentum equation second order, upwind-biased, unbounded scheme is used, while in the LS equation numerical scheme with van Leer limiter is used. For incident components second-order, unbounded schemes are used.

*Diffusion.* Incident components of the velocity and LS field are discretised using linear interpolation.

Additionally, for discretisation of the dynamic pressure gradient in the momentum equation linear interpolation with implicit jump conditions across the interface is used.

## 5.4 Reference transient simulation

The transient simulation is performed using the same mesh as in the HB simulation. The only difference between the HB and transient mesh is the body placement as it can be seen by comparing Figures 5.3 and 5.5. In order to ensure periodic convergence, 200 periods are simulated with 650 time-steps per wave period. First order harmonic amplitude of heave motion  $X_{1,y}$  is obtained with the Fast Fourier Transform (FFT) of the position signal in time. Analogously, first,  $F_{1,y}$  and second  $F_{2,y}$  order harmonic amplitude of force is obtained with the FFT of the force signal in time. The input of the FFT is the moving window with the width corresponding to the encounter period  $T_e$ . Successive moving window FFT's are used to determine the periodic convergence of the first and second order harmonic amplitudes.

Figure 5.9 presents the time series of heave motion, while the corresponding periodic convergence of first and second order amplitude of motion can be seen in Figure 5.10. Figure 5.11 presents the time series of heave force that acts on a body, while Figure 5.12 shows the periodic convergence of first and second order force amplitude with respect to the number of simulated periods. Converged values of first and second order amplitudes of position and force that will be used for comparison with the HB simulation are given in Table 5.2.

**Table 5.2: Periodically converged results for first and second harmonic amplitudes of the position and force.**

Order, $i$	position, $X_i$ [m]	force, $F_i$ [N]
1st	0.01308	28.6312
2nd	0	1.07

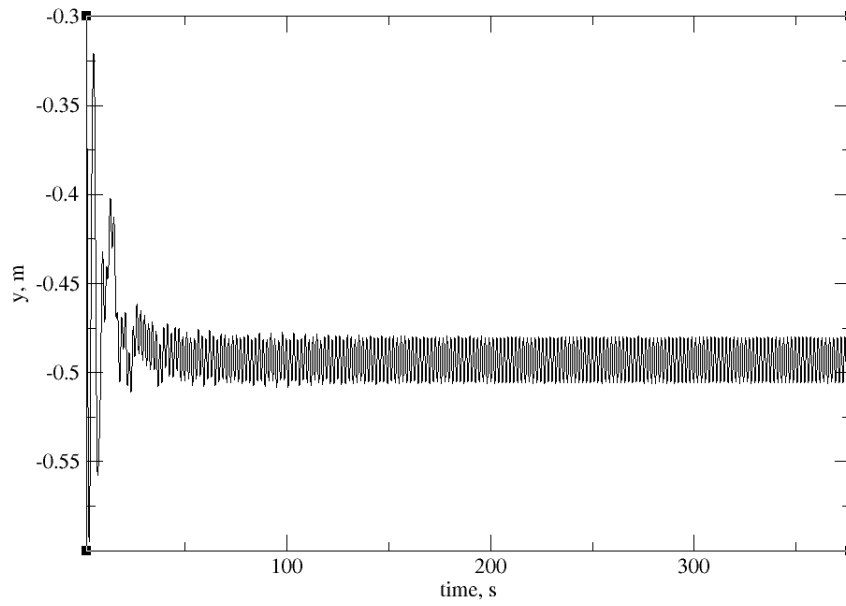


Figure 5.9: Time signal of the rigid body position.

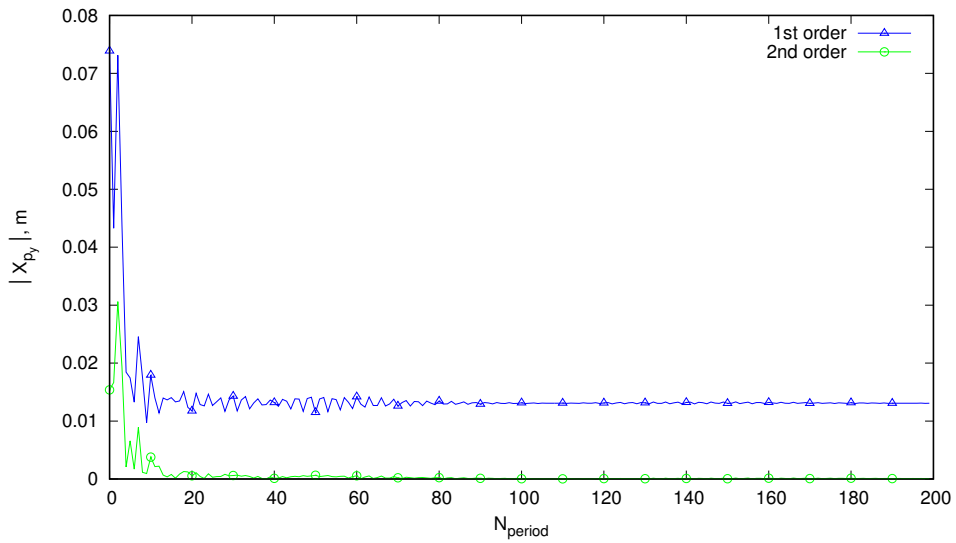


Figure 5.10: Periodic convergence of the position Fourier coefficients.

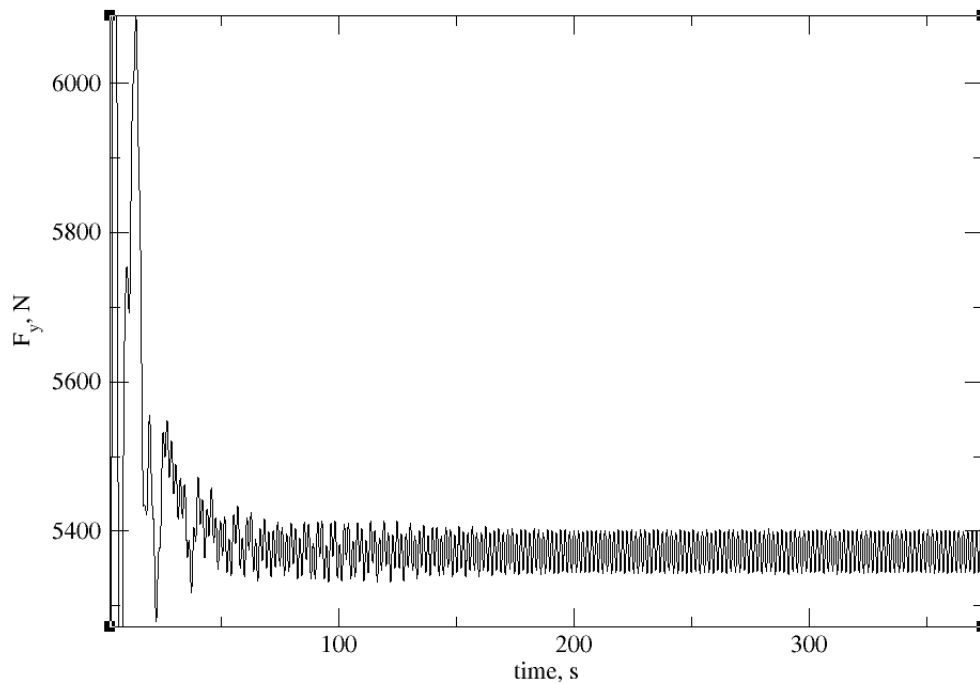


Figure 5.11: Time signal of the force acting on the rigid body.

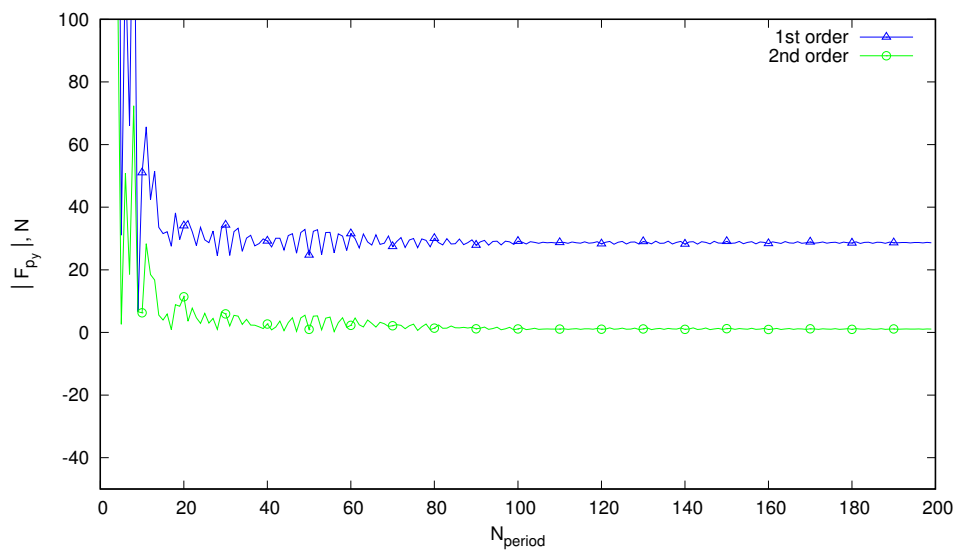


Figure 5.12: Periodic convergence of force Fourier coefficients.

## 5.5 Comparison of the HB and transient simulation results

Results of the HB simulation that are presented in this section are obtained with six harmonics. Initially a simulation with two harmonics was performed, however it diverged which is why the number of harmonics was increased. With four harmonics the simulation

converged, however in order to establish sensitivity of the result to the number of used harmonics, an additional simulation with six harmonics is performed. Since the difference between the results obtained from the simulations with four and six harmonics is around 1%, additional increase in the number of harmonics was rendered unnecessary. In order to ensure convergence 20000 iterations are performed.

First and second order harmonic amplitudes of position and force are given in Table 5.3, while the convergence of the first order position and first order force amplitude is shown on Figure 5.13 and Figure 5.14, respectively.

**Table 5.3: First and second order harmonic amplitude of the position and force obtained from HB simulation with 6 harmonics.**

Order, $i$	motion, $X_i$ [m]	force, $F_i$ [N]
1st	0.01468	$31.8 \pm 0.6$
2nd	0	$1.35 \pm 0.35$

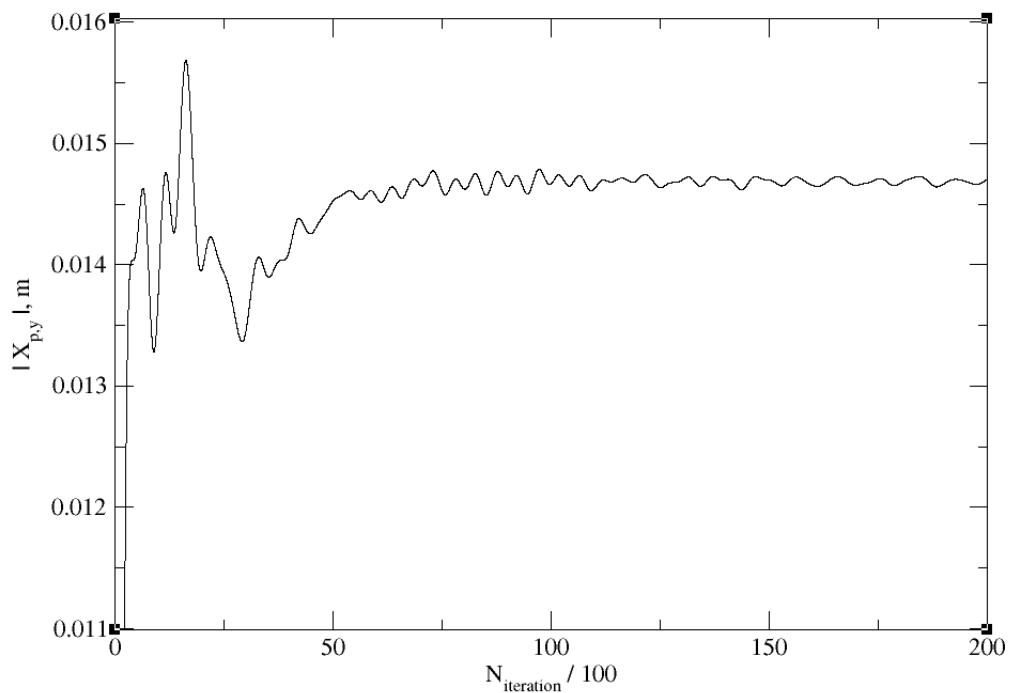


**Figure 5.13: Convergence of the first order position amplitude.**

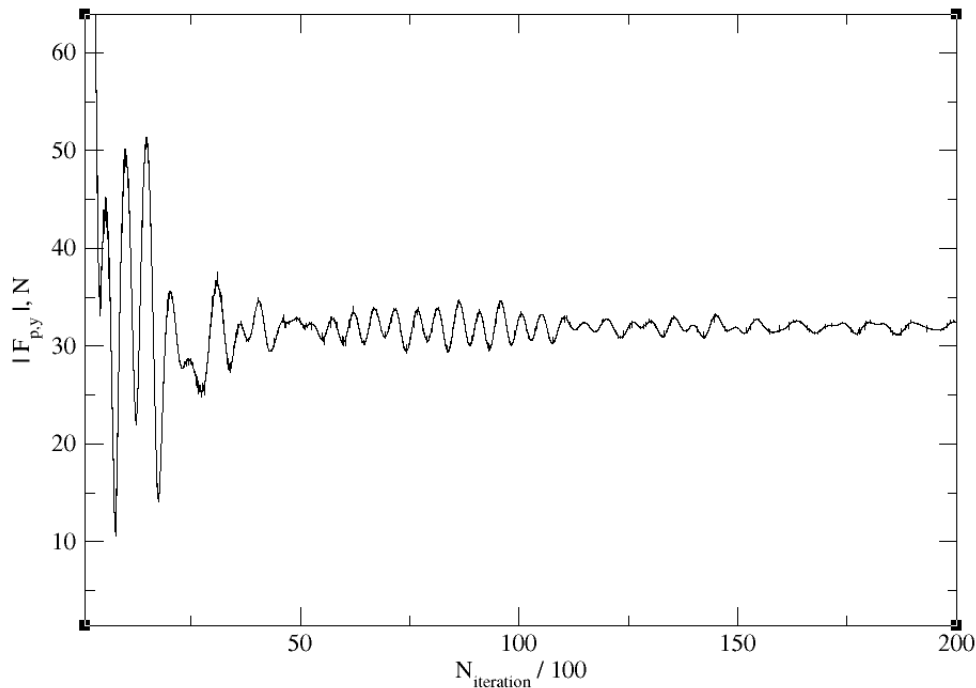


**Figure 5.14: Convergence of the first order force amplitude.**

Table 5.4 shows the results of the first order harmonic amplitude of position and the first and second order harmonic amplitudes of force for different number of harmonics and relative difference with respect to the transient simulation. The absolute value of relative difference  $\varepsilon = (S_t - S_{hb})/S_t$  between HB and transient simulation is given in percentages, where  $S_t$  denotes transient solution and  $S_{hb}$  denotes the HB solution. The relative difference of the first order position amplitude for the simulation with four harmonics is 13.6%, and for the simulation with six harmonics relative difference drops to 12.23%.

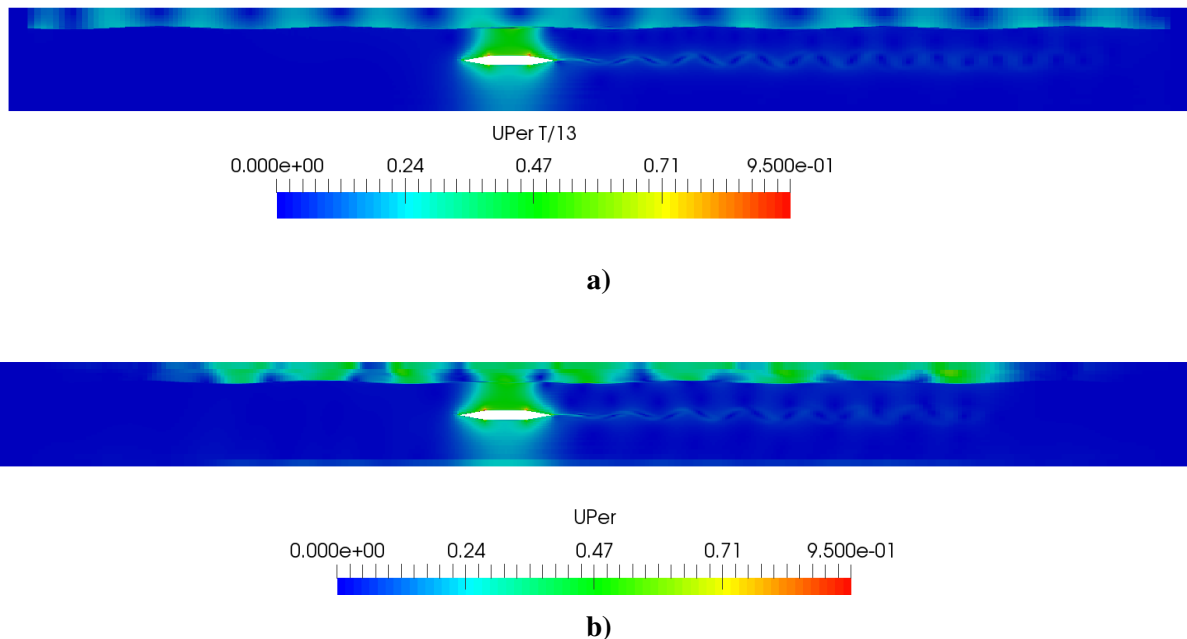
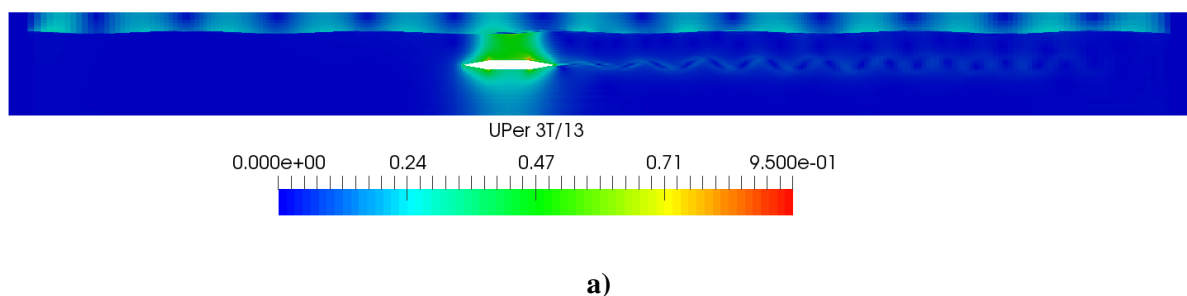
The first and second order force amplitudes in the HB simulation are not fully converged, i.e. they are periodically changing between minimum and maximum values. Hence, in Table 5.4 values for force amplitudes are given as a range of values. In the simulation with four harmonics, biggest relative difference of first order force amplitude is 15.96%, while in the simulation with six harmonics biggest relative difference drops to 13.16%. Since the value of the second order force amplitude is changing nearly  $\pm 50\%$  from its mean value in both simulations they cannot be taken into consideration. Nevertheless, because the magnitude of the second order force amplitude is relatively small with respect to the magnitude of first order force amplitude it does not affect the overall motion of the body. Note that the second order amplitude of position is not given in Table 5.4 since it is negligibly small.

**Table 5.4: Results of the HB simulations with 4 and 6 harmonics and the relative difference towards transient simulation.**

No. Harmonics	$X_1$ [m]	$F_1$ [N]	$F_2$ [N]	$ \varepsilon_{X_1} , \%$	$ \varepsilon_{F_1} , \%$	$ \varepsilon_{F_2} , \%$
4	0.01486	$32 \pm 1.2$	$1.3 \pm 0.6$	13.6	$11.765 \pm 4.195$	77.57
6	0.01468	$31.8 \pm 0.6$	$1.35 \pm 0.35$	12.23	$11.065 \pm 2.095$	58.87

The Figures 5.15, 5.16, 5.17 and 5.18 show perturbation velocity fields  $\underline{u}_P$  at randomly selected time instants and their corresponding field from transient simulation.

From the figures it can be seen that the velocity fields in water are similar. However, the magnitude of the perturbation velocity field in the air is greater in the transient simulation, while the periodic distribution of the velocity is more representative in the HB simulation. This is very likely related to the existence of high values of dynamic pressure in the relaxation zones of the transient simulation, as can be seen in Figures 5.19, 5.20 and 5.21. Nevertheless, from the same figures it can be seen that the dynamic pressure fields around the submerged body are similar. Perturbation velocity field differences in air do not affect the motion in this case since the body is submerged.

**Figure 5.15: (a) HB simulation at  $T/13$ , (b) Transient simulation at  $T/13$ .**

a)



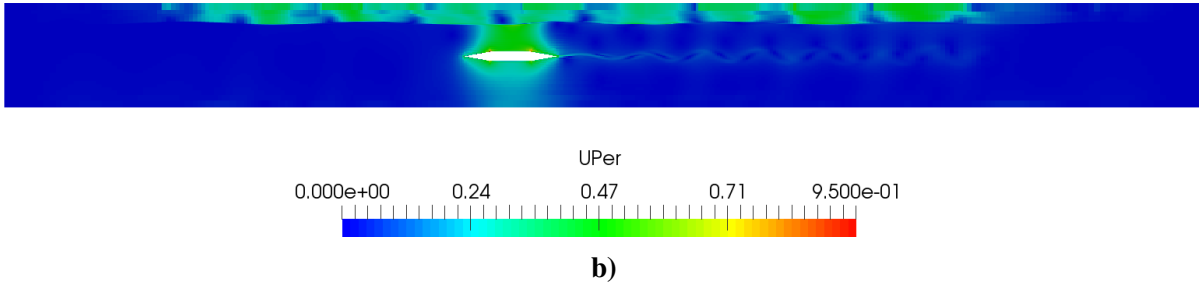


Figure 5.16: (a) HB simulation at  $3T/13$ , (b) Transient simulation at  $3T/13$ .

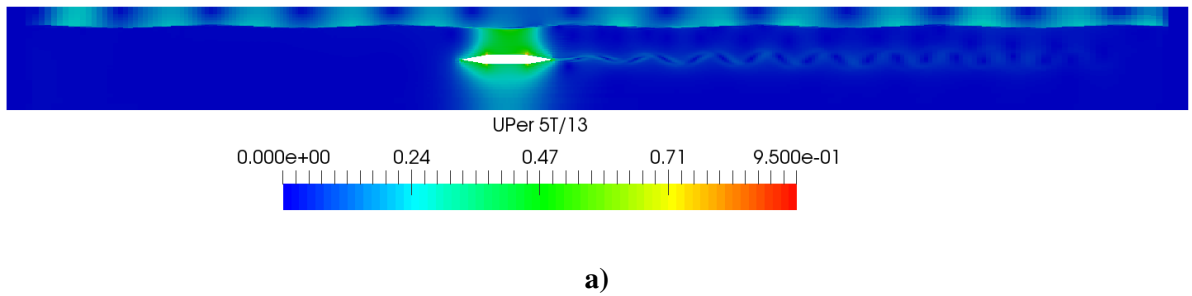
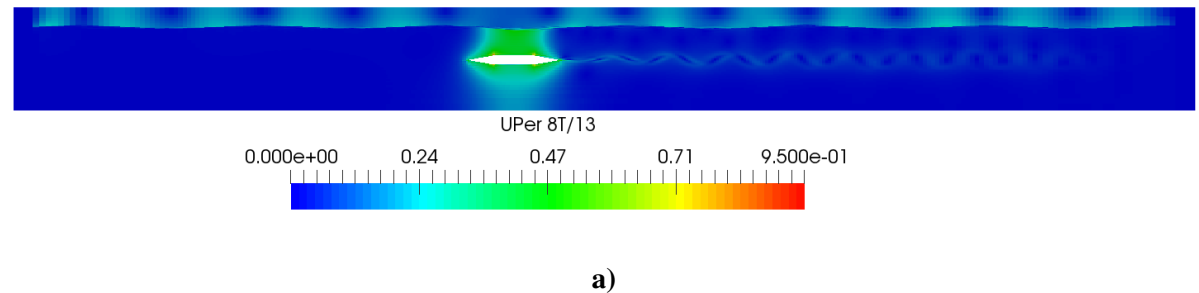
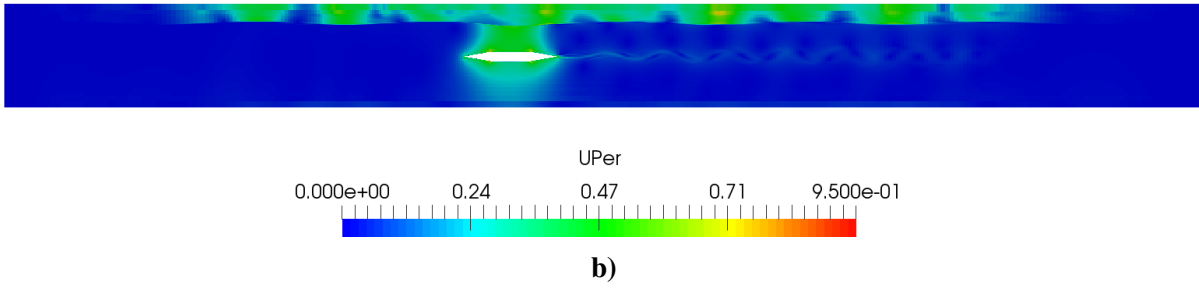


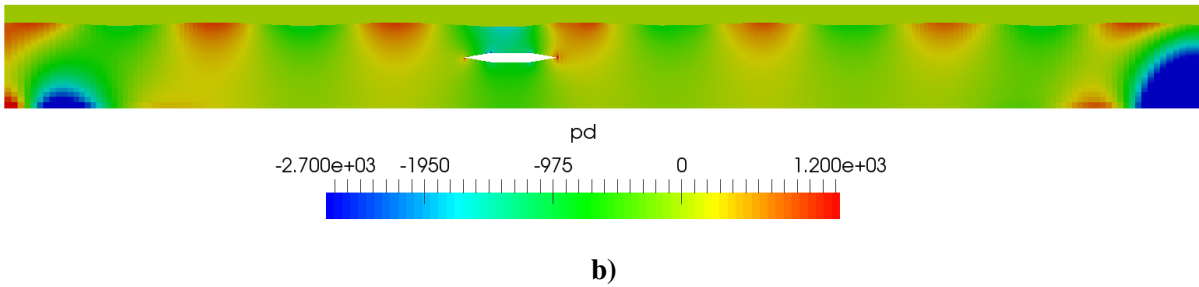
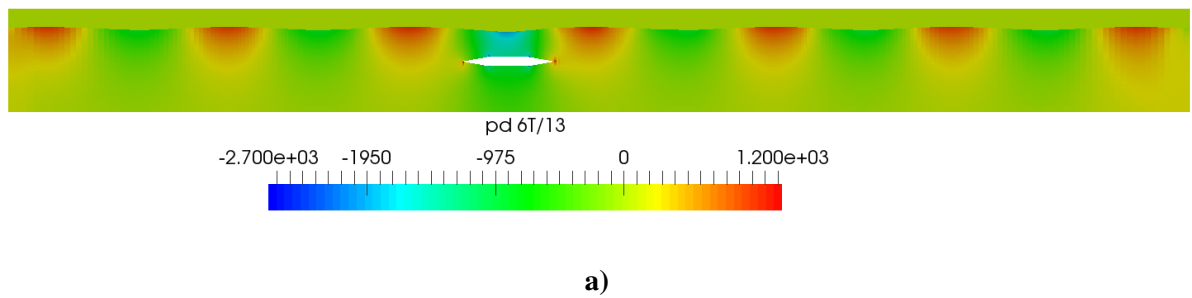
Figure 5.17: (a) HB simulation at  $5T/13$ , (b) Transient simulation at  $5T/13$ .



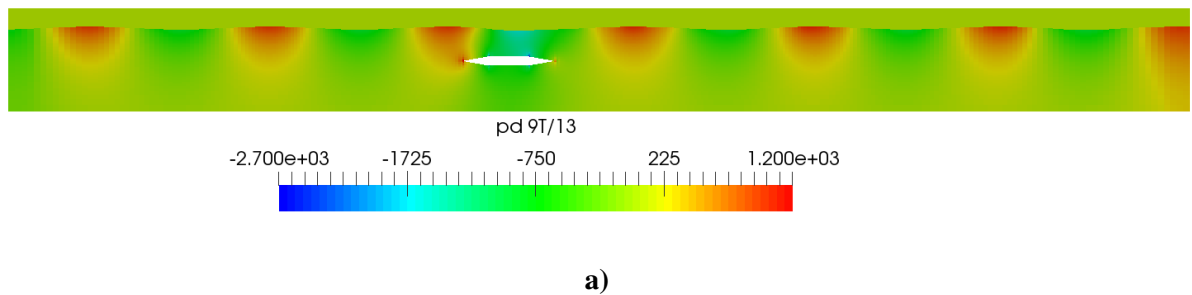


**Figure 5.18: (a) HB simulation at  $8T/13$ , (b) Transient simulation at  $8T/13$ .**

Figures 5.19, 5.20 and 5.21 are showing comparable dynamic pressure fields at randomly selected time instants.



**Figure 5.19: (a) HB simulation at  $6T/13$ , (b) Transient simulation at  $6T/13$ .**



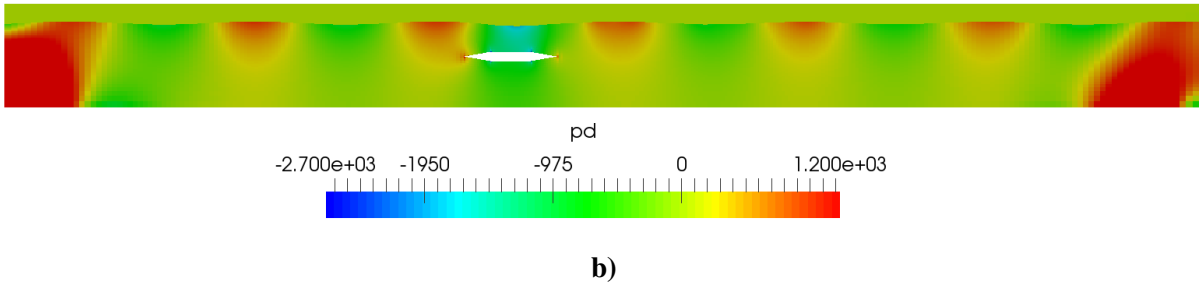


**Figure 5.20: (a) HB simulation at  $9T/13$ , (b) Transient simulation at  $9T/13$ .**

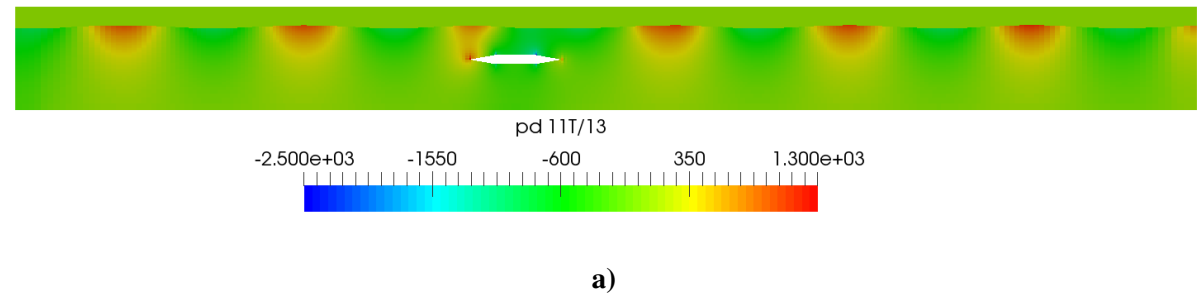


**Figure 5.21: (a) HB simulation at  $11T/13$ , (b) Transient simulation at  $11T/13$ .**

The wake pattern produced by the submerged body motion can be noticed in Figures 5.19, 5.20 and 5.21. Therefore, the zoomed view of the wake pattern in the eighth time instant of the HB simulation is shown in Figure 5.22.

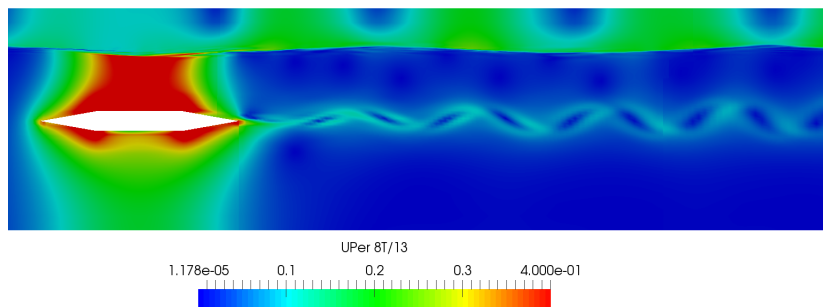


**Figure 5.22: The wake pattern**

## 5.6 Conclusion

The goal of this chapter was to validate heave motion of a rigid body calculated with HB simulation. It is shown that relative difference between HB and the corresponding transient simulation is between 10% and 15%. The discrepancies are acceptable since the motion of the submerged body is extremely mild. First order amplitude of force is only 0.32% of the body weight, while the amplitude of motion is smaller than 10% of wave height.

In the future work it is necessary to validate rotational motion and the complete *6DOF* motion with a *3D* case. Nevertheless, results in this chapter are confirming that the HB method can be used to simulate wave induced motion.

## 6 Conclusion and Future Work

This thesis presents a method for rigid body motion calculation which is compatible with the HB method that is used to calculate flow field. New method is tested on two test cases. In the first test case, translational and rotational motion is validated with analytical results, while in the second test case results are compared to the corresponding transient simulation.

In order to be able to describe the derivation of governing equations for rigid body dynamic in the frequency domain, existing HB method which is used to simulate two-phase, nonlinear and viscous flow is explained. First, governing equations in the basic form and the jump conditions at the interface are described, followed by the SWENSE decomposition method and governing equations in SWENSE form. Next, basics of HB method are given as well as the advantages of the implicit coupling of the source term. At last, HB method is used to transform SWENSE decomposed governing equation into time-spectral form, i.e. HB form. These equations are then implemented in a numerical solver to simulate two-phase, nonlinear and viscous flow. Following the brief overview of HB method, detailed derivation of the motion equations is given.

Validation of the new method is then conducted on two test cases. Goal of the first test case is to validate translational and rotational motion when the force and torque remained constant during the simulation. In order to check the accuracy of the method, complexity of forces and torques acting on the body increased up until the point when they were given as a combination of four orders of harmonic amplitudes. Results for this test case showed that this method can be used since numerical and analytical results are the same.

Second test case was designed to validate wave-induced body motion. In this case only heave motion was tested. Results of the HB simulation are compared to transient simulation results. Results show around 12% of relative difference for position and around 15% relative difference for force. These results are good enough considering the mild motion of the body. Hence, the results have shown that the body motion can be calculated in frequency domain.

Disadvantage of the method that is now implemented is the inability to calculate mean value motion. That should be the focus of future work. Furthermore, in this thesis only translational motion induced by waves was validated, so in future work rotational motion should be validated. Additionally, the final validation study should be performed on a realistic 3D ship.

In short, this thesis shows that ship motion calculation in naval hydrodynamics can be performed in the frequency domain with the HB method. With additional work this method should lead toward automatic optimisation of ship resistance in waves in the process of ship design.

## References

- [1] Jasak, H., “OpenFOAM: Open source CFD in research and industry,” International Journal of Naval Architecture and Ocean Engineering, Vol. 1, No. 2, 2009, pp. 89–94.
- [2] Sun, Y. and Beckermann, C., “Sharp interface tracking using the phase-field equation,” Journal of Computational Physics, Vol. 220, No. 2, 2007, pp. 626–653.
- [3] Vukčević, V., Jasak, H., and Malenica, Š., “Decomposition model for naval hydrodynamic applications, Part I: Computational method,” Ocean Engineering, Vol. 121, 2016, pp. 37–46.
- [4] Vukčević, V., Jasak, H., and Gatin, I., “Implementation of the Ghost Fluid Method for free surface flows in polyhedral Finite Volume framework,” Computers and Fluids, Vol. 153, 2017, pp. 1–19.
- [5] Gatin, I. and Jasak, H., “Harmonic Balance Method for Nonlinear and Viscous Free Surface Flows,” Submittet to Ocean Engineering, 2017.
- [6] Cvijetić, G., Jasak, H., and Vukčević, V., “Finite Volume Implementation of Non-Linear Harmonic Balance Method for Periodic Flows,” SciTech, Vol. Im, No. January, 2016, pp. 1–21.
- [7] Müller, A. and Terze, Z., “Geometric methods and formulations in computational multibody system dynamics,” Acta Mechanica, Vol. 227, No. 12, 2016, pp. 3327–3350.
- [8] Vukčević, V., Jasak, H., and Malenica, Š., “Decomposition model for naval hydrodynamic applications, Part II: Verification and validation,” Ocean Engineering, Vol. 121, 2016, pp. 76–88.
- [9] Vukčević, V. and Jasak, H., “Seakeeping validation and verification using decomposition model based on embedded free surface method,” in: Tokyo 2015: A workshop on CFD in Ship Hydrodynamics, 2015.
- [10] Gatin, I., Vukčević, V., and Jasak, H., “Validation and verification of steady resistance kcs simulations with dynamic sinkage and trim of kcs using embedded free surface method,” in: Tokyo 2015: A workshop on CFD in Ship Hydrodynamics, 2015.
- [11] Vukčević, V., Jasak, H., and Malenica, S., “Assessment of Higher-Order Forces on a Vertical Cylinder with Decomposition Model Based on SWENSE Method,” Numerical Towing Tank Symposium, 2015, pp. 1–6.
- [12] Larsson, L., Stern, F., and Visonneau, M., “Numerical Ship Hydrodynamics - An Assessment of the Gothenburg 2010 Workshop,” 2013.

- [13] Keddam, M., “Offshore Hydromechanics,” Electrochimica Acta, Vol. 47, No. January, 2002, pp. 1503–1504.
- [14] He, L. and Ning, W., “Efficient Approach for Analysis of Unsteady Viscous Flows in Turbomachines,” AIAA Journal, Vol. 36, No. 11, 1998, pp. 2005–2012.
- [15] Maple, R. C., King, P. I., Orkwis, P. D., and Wolff, J. M., “Adaptive harmonic balance method for nonlinear time-periodic flows,” Journal of Computational Physics, Vol. 193, No. 2, 2004, pp. 620–641.
- [16] McMullen, M. S. and Jameson, A., “The computational efficiency of non-linear frequency domain methods,” Journal of Computational Physics, Vol. 212, No. 2, 2006, pp. 637–661.
- [17] Ekici, K., Hall, K. C., and Dowell, E. H., “Computationally fast harmonic balance methods for unsteady aerodynamic predictions of helicopter rotors,” Journal of Computational Physics, Vol. 227, No. 12, 2008, pp. 6206–6225.
- [18] Guédeney, T., Gomar, A., Gallard, F., Sicot, F., Dufour, G., and Puigt, G., “Non-uniform time sampling for multiple-frequency harmonic balance computations,” Journal of Computational Physics, Vol. 236, No. 1, 2013, pp. 317–345.
- [19] Saad, Y., “Parallel iterative methods for sparse linear systems,” Studies in Computational Mathematics, Vol. 8, No. C, 2001, pp. 423–440.
- [20] “Courant–Friedrichs–Lewy condition,” <https://www.cfd-online.com/Wiki/Courant>
- [21] Weisstein, E. W., “Quaternion,” <http://mathworld.wolfram.com/Quaternion.html>.
- [22] Stramigioli, S. and Bruyninckx, H., “Geometry and screw theory for robotics,” Tutorial during ICRA 2001, Vol. 2001, 2001, pp. 75.
- [23] Terze, Z. and Eiber, A., “Dynamics of Multibody Systems second edition,” 233, 2008.
- [24] Cai et al, “Nonlinear filters: Estimation and Applications,” Sensors, Vol. 14, No. 3, 2010, pp. 1251–1260.
- [25] Vukčević, V. and Jasak, H., “Seakeeping Validation and Verification using Decomposition Model based on Embedded Free Surface Method,” Tokyo 2015: A workshop on CFD in Ship Hydrodynamics, December 2015.
- [26] Vukčević, V. and Jasak, H., “Validation and Verification of Decomposition Model based on Embedded Free Surface Method for Oblique Wave Seakeeping Simulations,” Tokyo 2015: A workshop on CFD in Ship Hydrodynamics, December 2015.
- [27] Pointwise, “Gridgen Manual,” Sleep (Rochester).

- [28] Reinecker, M. and Fenton, J., “A Fourier approximation method for steady water waves,” *J. Fluid Mech.*, Vol. 104, No. 18, 1981, pp. 119–137.
- [29] “OpenFOAM v5 User Guide: 4.4 Numerical schemes,” <https://cfd.direct/openfoam/user-guide/fvschemes/>.